Interplay of Structural and Light-induced Carrier Dynamics in Metal Halide Perovskites

Zhao, J.

DOI
10.4233/uuid:158da0dc-e2a8-4c59-8af8-5b50b2b96c94

Publication date
2024

Document Version
Final published version

Citation (APA)
Zhao, J. (2024). *Interplay of Structural and Light-induced Carrier Dynamics in Metal Halide Perovskites*. [Dissertation (TU Delft), Delft University of Technology]. https://doi.org/10.4233/uuid:158da0dc-e2a8-4c59-8af8-5b50b2b96c94

Interplay of Structural and Light-induced Carrier Dynamics in Metal Halide Perovskites

Interplay of Structural and Light-induced Carrier Dynamics in Metal Halide Perovskites

Dissertation

for the purpose of obtaining the degree of doctor
at Delft University of Technology
by the authority of the Rector Magnificus Prof. dr. ir. T.H.J.J. van der Hagen,
chair of the Board for Doctorates
to be defended publicly on
Monday 18 March 2024 at 12:30 o'clock

by

Jiashang ZHAO

Master of Science in Physical Chemistry,
Renmin University of China, Beijing, China,
born in Hebei, China.

This dissertation has been approved by the promotors.

Composition of the doctoral committee:

Rector Magnificus,	chairperson
Dr. ir. T.J. Savenije	Delft University of Technology, promotor
Prof. dr. A.J. Houtepen	Delft University of Technology, copromotor
Independent members:	
Prof. dr. L.J.A. Koster	University of Groningen
Prof. dr. S.J. Picken	Delft University of Technology
Prof. dr. ir. O. Isabella	Delft University of Technology
Dr. ir. A. Huijser	University of Twente
Prof. dr. F.C. Grozema	Delft University of Technology, reserve member

Printed by: ...

Cover designed by: J. Zhao

ISBN 000-00-0000-000-0

An electronic version of this dissertation is available at
http://repository.tudelft.nl/.

Learn as much as you can
do all you can do

活到老 学到老

Contents

1

Introduction

1

Nowadays, the rapid rise of the human population and economic growth lead to an increasing global energy demand. To meet this enormous demand, fossil fuels are burned on a huge scale. However, the global warming caused by fossil fuel burning is increasingly affecting the world's ecosystem, having a huge impact on nature as well as human civilization. For these reasons, renewable and clean energy sources need to be developed to meet the growing energy demands and to reduce CO_2 emissions. According to the International Energy Agency (IEA),[1] global renewable electricity capacity is forecast to rise over 60% and is expected to contribute almost 95% of the increase in global power capacity by 2026, with solar photovoltaic (PV) alone providing more than half. Currently, silicon (Si) solar cells dominate the PV market.[2] In order to reduce the cost of balance of system, such as the inverter, solar charge controller, and installation, further improvement of the efficiency of solar modules is necessary. PV based on metal halide perovskites (MHPs) is one of the most promising PV technologies for next-generation solar cells, including single-junction or Si/perovskite tandem solar cells. In 2009 perovskite solar cells (PSCs) were first used as dye in a so-called dye-sensitized solar cell yielding a power conversion efficiency (PCE) of 3.8%.[3] Over the last decade, the performance has rapidly increased to over 26% in a single junction solar cell.[4–11] Hence, investigating the structural and fundamental optoelectronic properties responsible for this impressive PCE enhancement is of great scientific interest and huge technological importance. This chapter introduces the general structure and various compositions of perovskites and then describes the different preparation methods of perovskite thin films. Next, the main decay processes following upon optical excitation are discussed. Finally, the research aim and outline of this thesis are provided.

1.1. The crystal structure and compositional engineering of MHPs

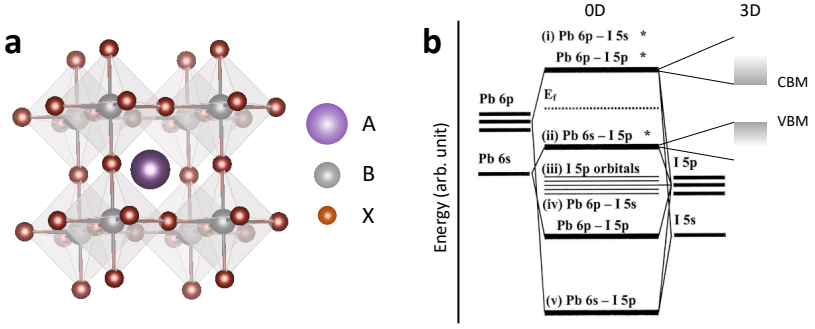

Figure 1.1: (a) Crystal structure, and (b) Bonding diagram of $[PbI_6]^{4-}$ cluster and 3D perovskite, adapted from ref[12].

The term perovskite is derived from the original name of calcium titanate ($CaTiO_3$) and is used for the class of materials, which have the same type of crystal structure as $CaTiO_3$. For the perovskites discussed in this thesis, the chemical formula is ABX_3,[13]

with A, a monovalent cation, B, a divalent metal cation, and X, a halide anion. The 3D structure is built up of corner-sharing BX_6 octahedra, while the A cations fill the voids between the BX6 octahedra, as shown in Figure 1.1a. The A cation can be methylammonium (MA, $CH_3NH_3^+$), formamidinium (FA, $CH(NH_2)_2^+$), or cesium (Cs^+); The B cation can be lead (Pb^{2+}) or tin (Sn^{2+}), and X is a halide anion Cl^-, Br^-, I^-. In terms of composition, the A cation can consist of a single or a mix of cations, as is also the case for ions at the B and X sites. The electronic band structure of perovskites, including the valence band and conduction band, is mainly composed of orbitals of the B cations and X anions (Figure 1.1b).[12] The band gap (E_g) can be tuned ranging from 1.2 to 3.0 eV by varying the B cations and X anions (Figure 1.2). In this thesis, only Pb-based perovskites are studied, while the A cations and/or X anions are varied.

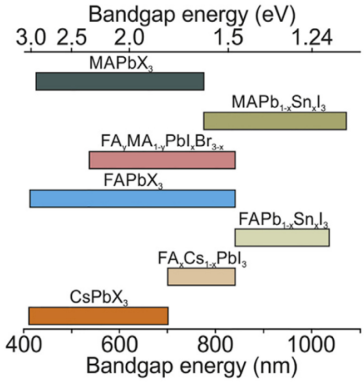

Figure 1.2: Bandgap energies for different combinations of A, B, and X ions in the ABX_3 perovskite structure, taken from ref[14].

Compositional engineering is one of the most effective approaches to improve the performance of PSCs. The initially most studied MHP is $MAPbI_3$ with an E_g of approximately 1.6 eV. Starting with a PCE of 9.7% in 2012,[4] tremendous efforts have been devoted over the past few years to improve efficiency, yielding a record PCE of over 22%.[15] Despite this astonishing achievement, $MAPbI_3$ suffers from structural instability and undesired degradation upon heating as well as the formation of trap states under light illumination.[16] To further boost the performance and improve the stability of PSCs, researchers have started seeking more promising alternatives, such as $FAPbI_3$ with a more narrow E_g of 1.48 eV, which is close to the optimal band gap of single junction solar cell.16 Moreover, upon mixing FA with small amounts of MA and/or Cs, the resulting $CsMAFAPbI_3$ exhibits better thermal and long-term operational stability. Furthermore, the crystal structure is more phase stable at room temperature, which can be explained by the fact that the Goldschmidt tolerance factor (t) is close to 1.[17] This factor is related to the A, B, X ionic radii (R_A, R_B, R_X), described as:

$$t = \frac{R_A + R_X}{\sqrt{2}R_B + R_X} \tag{1.1}$$

Another great advantage of MHPs, is the tunability of the bandgap, enabling the integration into multi-junction tandem solar cells, such as perovskite-Si tandem solar cells or all-perovskite tandem solar cells.[18–20]

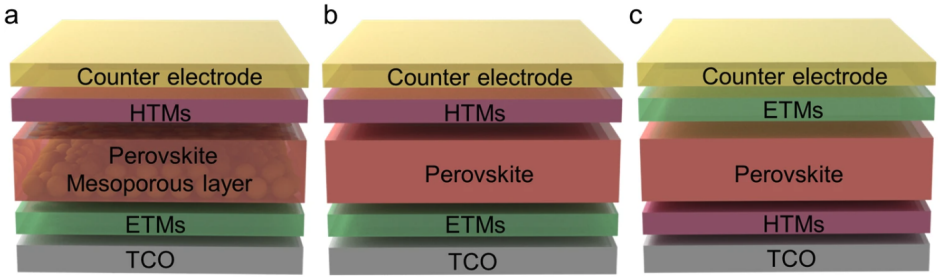

Figure 1.3: Perovskite solar cells with (a) conventional mesoporous n-i-p, (b) planar n-i-p, and (c) inverted planar p-i-n configurations, taken from ref[21].

For single junction PSCs, commonly employed device structures are either conventional (n-i-p) including both mesoporous and planar architectures, or inverted (p-i-n) planar configurations, as shown in Figure 1.3. In the early stages of PSC development, mesoporous PSCs composed of a dense and mesoporous TiO_2 layer yielded the best efficiency but exhibited high hysteresis in the current-voltage curves.[22,23] Later, planar structures using alternative SnO_2 instead of TiO_2 showed improved performance and these could be fabricated via low-temperature processes. Up to now, the highest recorded PCEs for single junction PSCs have achieved 26.1%[11] in conventional n-i-p structures and 24.6%[10] with an inverted p-i-n configuration. Although PSCs with p-i-n structures currently demonstrate lower performance compared to regular n-i-p structures, they exhibit enhanced stability which is related to the use of undoped hole transport layers and are promising for integration into tandem solar cells.[18] Nevertheless, based on Shockley-Queisser theoretical calculations,[24,25] an upper limit on PCE of 33.7% can be attained for a single junction PSC featuring an ideal band gap light absorber ($E_g \approx 1.4$ eV) under AM 1.5 solar spectrum. To overcome this limitation, tandem solar cells, comprising both wide-bandgap and narrow-bandgap solar cells, have gained more and more attention. They allow for the effective absorption of a broader range of solar radiation into the infrared, thereby minimizing the thermalization loss of the excess photon energy. Therefore, much higher PCEs are feasible for tandem solar cells in comparison to their single-junction counterparts.

1.2. Deposition methods of MHP films: spin-coating vs thermal evaporation

In addition to the optimization by compositional engineering, the preparation process of MHPs also plays a crucial role in improving the efficiency of PSCs. One of the most commonly used solution-based fabrication methods is spin-coating, which can consist of a one-step spin-coat process or a two-step spin-coat process.[26] Initially, the two-step procedure, including the deposition of PbI_2 and subsequent dipping into an MAI so-

lution, is usually used to fabricate $MAPbI_3$-based PSCs, which is beneficial to control the crystal domain size and morphology of perovskite. However, concerning the mixed cation, and mixed halide MHPs, the one-step process proves to be more straightforward to perform. In a one-step spin-coating process, after deposition of the precursor solution containing all the precursors in the right stoichiometric amounts, perovskite films are formed by evaporation of the solvent. The as-deposited films are then annealed to completely convert the remaining precursors into the perovskite structure and to enhance the crystal growth. Notably, nucleation of the perovskite starts already during spinning, which affects consecutive growth during the annealing process and consequently its final morphology.[27] Hence, it is important to have some control over the perovskite nucleation and growth in order to be able to manipulate the final crystal structure, grain size, and homogeneity.

Figure 1.4: Schematic representation of the perovskite film fabrication process using an antisolvent, adapted from ref[28].

The antisolvent extraction method has been widely employed in the one-step spin-coating process to facilitate the removal of the polar organic solvent used to dissolve the precursors (Figure 1.4). The introduction of the antisolvent during the spin-coating process leads to a sudden change in the solubility of the precursors. As a result of this change, the dissolved precursors precipitate immediately, followed by rapid evaporation of the remaining solvent mixture. All process steps, including spin speeds, choice of solvents, and timings influence the eventual quality of formed perovskite films. Therefore, finding the optimal time to apply the antisolvent is of great importance to achieve dense, compact, and well-crystallized MHPs. A recent study demonstrates the mechanism of MHP formation using different antisolvents and optimal times on the eventual layer morphology.[28] We used this antisolvent method to prepare our samples in Chapters 4 and 5. It is worth noting that another key advantage of the solution-processing method is the possibility of introducing additives into the perovskite precursor solution to manipulate the structural and optoelectronic properties of perovskite films.[29] For instance, the introduction of hypophosphorous acid (HPA) into the $MAPbBr_3$ precursor solution in Chapter 2 leads to an increase in crystal domain size and a reduction in trap states.

An alternative approach to deposit perovskite layers is thermal evaporation, including, single-source evaporation, and sequential- or co-evaporation via multiple sources (Figure 1.5).[29,30] Compared to solution processing of MHP films by spin-costing, thermal evaporation has benefits, such as avoiding to use of toxic solvents and hence being more environmentally friendly. Additional advantages are precise controlling of the thickness of perovskite layers, deposition of the absorber layers without damaging the underlying

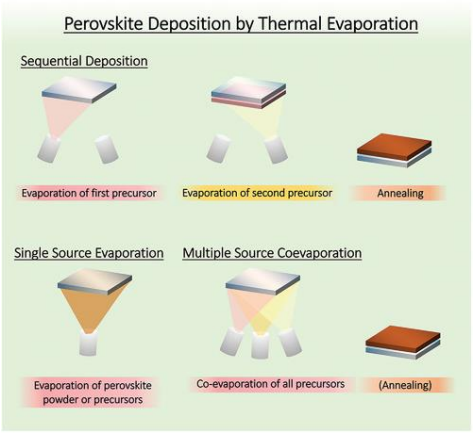

Figure 1.5: Schematic illustration of the deposition of a perovskite layer by thermal evaporation, adapted from ref[29].

layers as well as scaling up of large-area PSCs. For sequential deposition, the precursors are evaporated layer by layer via a single or multi-cycle strategy. Post-annealing is required to accelerate the inter-diffusion and complete conversion of MHPs along the penetration depth.[31] Dual-source or multisource co-evaporation is achieved by evaporating different precursors simultaneously.[32,33] The main advantage is the reduction in deposition time. During the thermal evaporation process, many parameters, for example, evaporation rate, pressure, substrate, and temperature affect the nucleation and growth of MHP films. Especially for co-evaporation, controlling the evaporation rates of each precursor is crucial to ensure the desired stoichiometry of the final films. Despite these challenges and complexities in operation, thermal evaporation-based PSCs have achieved a record efficiency of over 18% for a 21 cm^2 mini-module.[32] Apart from the above-mentioned deposition methods, there are many other methods for the deposition of MHP films, such as slot-die coating, blade-coating, inkjet printing, pulsed laser deposition, etc.[34–37]

1.3. Transport, recombination, and extraction of photogenerated charges in MHPs

For an efficiently working PSC, in principle, light absorption leads to the generation of free electrons and holes, which then diffuse towards the charge-selective transport layers, and eventually get collected by the electrodes. First of all, in view of the high absorption coefficient of MHPs in the visible range up to $10^4 - 10^5$ cm^{-1}, the absorber layer can be deposited with a thickness of only hundreds of nanometers (typically ~ 500 nm). Basically, the generation of free carriers upon photoexcitation depends on the exciton binding energy (E_x). For MHPs with $E_x \leq k_B T$, photogenerated excitons dissociate into free carriers, resulting in electrons in the conduction band and holes in the valence band.

The charge carrier transport properties can be evaluated by the diffusion length (L_D), carrier mobility (μ), and carrier lifetime (τ). By definition,

$$L_D = \sqrt{\frac{k_B T}{e} \mu\tau} \tag{1.2}$$

Since L_D is proportional to the square root of the mobility and carrier lifetime, slower recombination leads to longer diffusion lengths. For the minority carriers, L_D should be substantially larger than the thickness of the absorber layer to avoid the recombination losses as much as possible. Furthermore, μ depends on the intrinsic properties of semiconductor materials and is related to the effective mass and scattering time, i.e. a change in the composition of MHPs can lead to a change in the mobility. In addition, the carrier mobility is also affected by the grain size of the polycrystalline MHP layer.[38] Although the intragrain mobility can be high, the charge transfer between two grains might be hampered, limiting the overall transport properties.

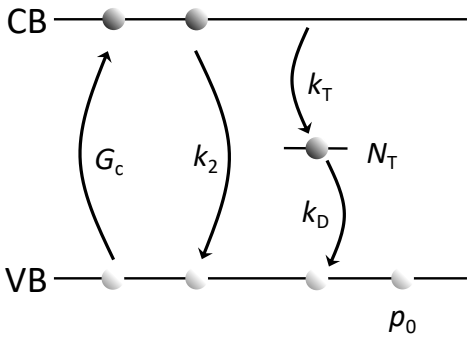

Figure 1.6: Schematic illustration of the recombination processes upon photoexcitation.

In a neat MHP absorber layer, photogenerated charge carriers can undergo a variety of recombination pathways (Figure 1.6), such as trap-mediated non-radiative recombination, band-to-band recombination, and Auger recombination. The latter mainly happens at very high carrier densities ($> 10^{18}$ cm^{-3}) and is negligible within the scope of photovoltaic applications. The charge carrier concentration is an important factor determining via which recombination pathway charges decay. At low carrier concentrations, the process of trap-filling is typically dominant and governed by the rate constants for trapping and depopulation, k_T and k_D, respectively. Second-order electron-hole recombination (k_2) becomes important at higher carrier concentrations in case the majority of traps are occupied. Trap-mediated non-radiative recombination tends to decrease both the short-circuit current and the open-circuit voltage (V_{oc}) of a corresponding solar cell. Therefore, defects in the bulk or at the surface of MHPs should be avoided, which means that the passivation of MHPs is essential to improve the photovoltaic performance. When combining an MHP absorber layer with selective transport layers (TLs), not only the recombination in the MHP bulk but also the carrier extraction to the TLs and recombination at the interfaces are important. Pinpointing the origin of

the defects or understanding carrier recombination mechanisms in a complete device can be very challenging. Therefore, studies on carrier extraction and recombination in stacks of an MHP combined with TLs are very helpful in understanding the origin of carrier recombination.[39,40]

Methods that have been used to study carrier recombination and extraction in MHPs in combination with TLs include time-resolved photoluminescence (TRPL),[41] terahertz spectroscopy,[42] transient absorption (TA),[43] and transient photovoltage (TPV).[44] In this thesis, we used a technique entitled time-resolved microwave conductivity (TRMC). This technique is based on the interaction of microwaves with all photo-induced free charge carriers and details regarding the theory and the set-up can be found in various overview papers.[45,46] Compared with the abovementioned techniques, the superior sensitivity of the TRMC technique allows the recording of the photo-conductivity at low light intensities similar to or less than AM 1.5. Moreover, this technique is contactless and requires only the MHP absorber layer with or without TLs, simplifying data interpretation as compared to measurements conducted on complete devices as is done in Chapter 5. On the other hand, the inability to implement conductive electrodes is also a shortcoming of TRMC. In addition, TRMC measurements reveal both radiative and non-radiative carrier recombination processes, while TRPL relies only on radiative charge carrier decay.

1.4. Low-temperature structural and optoelectronic properties in MHPs

The majority of studies on the photophysics of MHPs and the performance of PSCs have been carried out at room temperature. Research at low temperatures can provide insight into the intrinsic properties of MHPs. For example, temperature-dependent X-ray diffraction[47] provides insight into the phase behavior of MHPs. Cryogenic absorption and photoluminescence (PL) measurements[48,49] allow determining the exciton binding energy E_x. Extensive temperature-dependent studies on charge carrier dynamics, absorption, and PL as well as phase transitions have been carried out on $MAPbI_3$.[50] $MAPbI_3$ undergoes an abrupt transition from the orthorhombic to the tetragonal phase at around 160 K and a further transition to the cubic phase at 330 K. Interestingly, in the tetragonal phase the band-gap increases with elevating the temperature as the lattice expands. In addition, on decreasing the temperature, the carrier mobility increases due to reduced phonon scattering.[51] Despite the superior photovoltaic performance of state-of-the-art triple-cation lead mixed halide perovskites,[10,52] studies on their temperature-dependent structure and carrier dynamics are rather limited.[53] Therefore, it is of great interest to investigate the relationship between composition and fundamental photophysical properties at low temperatures in triple-cation lead mixed halide MHPs.

1.5. Research aim and outline of this thesis

This thesis aims to reveal how structure affects carrier recombination and collection kinetics of MHPs among different compositions using TRMC in neat absorber layer, bi-layer, and tri-layer systems.

In Chapter 2, we start with the wide-bandgap perovskite $MAPbBr_3$, which has great

potential to be used as the top cell in tandem solar cells. Carrier decay dynamics in neat $MAPbBr_3$ are studied using TRMC and TRPL. The combination of these two techniques allows us to pinpoint the nature of long-lived tails of TRMC signals, which can be explained by a large amount of hole defect states ($N_T > 10^{16}$ cm^{-3}) in comparison to $MAPbI_3$. Moreover, we find that defects can be passivated by introducing an additive, i.e. hypophosphorous acid (HPA), which leads to an increase in the average grain size. Chapter 3 is devoted to a study on co-evaporated $MAPbI_3$, which forms the absorber layer in devices with n-i-p or p-i-n architecture. Due to the co-evaporation process, the $MAPbI_3$ films show a gradient in composition and here the structural and optoelectronic properties of these layers are investigated. We find that an MAI deficiency predominantly in the top part of the $MAPbI_3$ films results in local n-doping, leading to the formation of an internal electric field across the film thickness. This internal electric field might be beneficial for charge carrier collection in PSCs with a p-i-n configuration but not for those in an n-i-p configuration. The highest efficiencies reported for PSCs are all based on triple-cation mixed-halide perovskites. Chapters 4 and 5 focus on $Cs_{0.05}FA_{0.85}MA_{0.10}Pb(I_{0.97}Br_{0.03})_3$ (CsMAFA) perovskites, which have been extensively studied in recent years, showing very promising performance and stability. In Chapter 4, we carry out an in-depth fundamental investigation of the relationship between the phase behavior and the optoelectronic properties in CsMAFA films with 5% excess PbI_2. XRD pattern refinement reveals that CsMAFA undergoes an α-β phase transition around 280 K and another transition to the γ-phase at $\sim$ 180 K. Furthermore, the microstrain in different phases are derived from Williamson-Hall plots. Fitting of the TRMC traces enables us to quantitatively extract the concentration of trap states. We conclude that CsMAFA exhibits the lowest amount of microstrain in the β-phase at around 240 K, corresponding to the lowest concentrations of trap states. Below 200 K we find a considerable increase in trap states most likely related to the temperature-induced compressive microstrain. To increase the open-circuit voltage in PSCs based on these CsMAFAs, reducing recombination processes at the interfaces with TLs is key. In Chapter 5, we study the charge carrier dynamics in bi- and tri-layers of CsMAFA with electron and hole TLs using TRMC in the absence and presence of bias illumination (BI). For bilayers, carrier extraction is nearly quantitative. Furthermore, we find almost balanced mobilities for electrons and holes in CsMAFA. For triple layers, both carriers are extracted at low laser intensities, independent of the configuration. Applying BI leads to equilibrium concentrations of carriers in both TLs and the resulting TRMC signal is much higher since charge extraction is retarded.

References

[1] V. P. Wright. World Energy Outlook. *International Energy Agency* (2023), 1–353.

[2] E. Płaczek-Popko. Top PV market solar cells 2016. *Opto-Electronics Review* **25** (2017), 55–64.

[3] A. Kojima, K. Teshima, Y. Shirai, and T. Miyasaka. Organometal halide perovskites as visible-light sensitizers for photovoltaic cells. *Journal of the American Chemical Society* **131** (2009), 6050–6051.

[4] H. S. Kim, C. R. Lee, J. H. Im, et al. Lead iodide perovskite sensitized all-solid-state submicron thin film mesoscopic solar cell with efficiency exceeding 9%. *Scientific Reports* **2** (2012), 591.

[5] J. H. Heo, S. H. Im, J. H. Noh, et al. Efficient inorganic-organic hybrid heterojunction solar cells containing perovskite compound and polymeric hole conductors. *Nature Photonics* **7** (2013), 486–491.

[6] H. Zhou, Q. Chen, G. Li, et al. Interface engineering of highly efficient perovskite solar cells. *Science* **345** (2014), 542–546.

[7] H. Tan, A. Jain, O. Voznyy, et al. Efficient and stable solution-processed planar perovskite solar cells via contact passivation. *Science* **355** (2017), 722–726.

[8] W. S. Yang, B. W. Park, E. H. Jung, et al. Iodide management in formamidinium-lead-halide-based perovskite layers for efficient solar cells. *Science* **356** (2017), 1376–1379.

[9] G. Kim, H. Min, K. S. Lee, et al. Impact of strain relaxation on performance of a-formamidinium lead iodide perovskite solar cells. *Science* **370** (2020), 108–112.

[10] G. Li, Z. Su, L. Canil, et al. Highly efficient p-i-n perovskite solar cells that endure temperature variations. *Science* **379** (2023), 399–403.

[11] NREL. *Best Research-Cell Efficiencies: Rev. October 2023*. 2023.

[12] T. Umebayashi, K. Asai, T. Umebayashi, et al. Electronic structures of lead iodide based low-dimensional crystals. *Physical Review B - Condensed Matter and Materials Physics* **67** (2003), 2–7.

[13] A. Poglitsch and D. Weber. Dynamic disorder in methylammoniumtrihalogenoplumbates (II) observed by millimeter-wave spectroscopy. *The Journal of Chemical Physics* **87** (1987), 6373–6378.

[14] M. Anaya, G. Lozano, M. E. Calvo, and H. Míguez. ABX3 Perovskites for Tandem Solar Cells. *Joule* **1** (2017), 769–793.

[15] K. Wang, C. Wu, Y. Hou, et al. Isothermally crystallized perovskites at room-temperature. *Energy and Environmental Science* **13** (2020), 3412–3422.

[16] E. J. Juarez-Perez, L. K. Ono, M. Maeda, et al. Photodecomposition and thermal decomposition in methylammonium halide lead perovskites and inferred design principles to increase photovoltaic device stability. *Journal of Materials Chemistry A* **6** (2018), 9604–9612.

[17] J. Cao and F. Yan. Recent progress in tin-based perovskite solar cells. *Energy and Environmental Science* **14** (2021), 1286–1325.

[18] A. Al-Ashouri, E. Köhnen, B. Li, et al. Monolithic perovskite/silicon tandem solar cell with >29% efficiency by enhanced hole extraction. *Science* **370** (2020), 1300–1309.

[19] J. Liu, M. De Bastiani, E. Aydin, et al. Efficient and stable perovskite-silicon tandem solar cells through contact displacement by MgFx. *Science* **377** (2022), 302–306.

[20] H. Chen, A. Maxwell, C. Li, et al. Regulating surface potential maximizes voltage in all-perovskite tandems. *Nature* **613** (2023), 676–681.

[21] S. Liu, V. P. Biju, Y. Qi, W. Chen, and Z. Liu. Recent progress in the development of high-efficiency inverted perovskite solar cells. *NPG Asia Materials* **15** (2023).

[22] M. M. Lee, J. Teuscher, T. Miyasaka, T. N. Murakami, and H. J. Snaith. Efficient hybrid solar cells based on meso-superstructured organometal halide perovskites. *Science* **338** (2012), 643–647.

[23] M. Kim, I. w. Choi, S. J. Choi, et al. Enhanced electrical properties of Li-salts doped mesoporous TiO2 in perovskite solar cells. *Joule* **5** (2021), 659–672.

[24] W. Shockley and H. J. Queisser. Detailed balance limit of efficiency of p-n junction solar cells. *Journal of Applied Physics* **32** (1961), 510–519.

[25] S. Rühle. Tabulated values of the Shockley-Queisser limit for single junction solar cells. *Solar Energy* **130** (2016), 139–147.

[26] J. Y. Kim, J. W. Lee, H. S. Jung, H. Shin, and N. G. Park. High-Efficiency Perovskite Solar Cells. *Chemical Reviews* **120** (2020), 7867–7918.

[27] D. Zheng, F. Raffin, P. Volovitch, and T. Pauporté. Control of perovskite film crystallization and growth direction to target homogeneous monolithic structures. *Nature Communications* **13** (2022).

[28] A. D. Taylor, Q. Sun, K. P. Goetz, et al. A general approach to high-efficiency perovskite solar cells by any antisolvent. *Nature Communications* **12** (2021), 1–11.

[29] Y. Vaynzof. The Future of Perovskite Photovoltaics—Thermal Evaporation or Solution Processing? *Advanced Energy Materials* **10** (2020), 2003073.

[30] J. H. Lee, B. S. Kim, J. Park, J. W. Lee, and K. Kim. Opportunities and Challenges for Perovskite Solar Cells Based on Vacuum Thermal Evaporation. *Advanced Materials Technologies* **2200928** (2022), 1–12.

[31] J. Yan, L. S. Stickel, L. van den Hengel, et al. Vacuum Deposited Perovskites with a Controllable Crystal Orientation. *The journal of physical chemistry letters* **14** (2023), 8787–8795.

[32] J. Li, H. Wang, X. Y. Chin, et al. Highly Efficient Thermally Co-evaporated Perovskite Solar Cells and Mini-modules. *Joule* **4** (2020), 1035–1053.

[33] Y. H. Chiang, M. Anaya, and S. D. Stranks. Multisource Vacuum Deposition of Methylammonium-Free Perovskite Solar Cells. *ACS Energy Letters* **5** (2020), 2498–2504.

[34] K. Xu, A. Al-Ashouri, Z. W. Peng, et al. Slot-Die Coated Triple-Halide Perovskites for Efficient and Scalable Perovskite/Silicon Tandem Solar Cells. *ACS Energy Letters* **7** (2022), 3600–3611.

[35] T. Tang, P. Dacha, K. Haase, et al. Analysis of the Annealing Budget of Metal Oxide Thin-Film Transistors Prepared by an Aqueous Blade-Coating Process. *Advanced Functional Materials* **33** (2023).

[36] H. Eggers, F. Schackmar, T. Abzieher, et al. Inkjet-Printed Micrometer-Thick Perovskite Solar Cells with Large Columnar Grains. *Advanced Energy Materials* **10** (2020).

[37] Y. Smirnov, L. Schmengler, R. Kuik, et al. Scalable Pulsed Laser Deposition of Transparent Rear Electrode for Perovskite Solar Cells. *Advanced Materials Technologies* **6** (2021).

[38] O. G. Reid, M. Yang, N. Kopidakis, K. Zhu, and G. Rumbles. Grain-Size-Limited Mobility in Methylammonium Lead Iodide Perovskite Thin Films. *ACS Energy Letters* **1** (2016), 561–565.

[39] E. M. Hutter, J. J. Hofman, M. L. Petrus, et al. Charge Transfer from Methylammonium Lead Iodide Perovskite to Organic Transport Materials: Efficiencies, Transfer Rates, and Interfacial Recombination. *Advanced Energy Materials* **7** (2017), 1–8.

[40] V. M. Caselli and T. J. Savenije. Quantifying Charge Carrier Recombination Losses in MAPbI3/C60 and MAPbI3/Spiro-OMeTAD with and without Bias Illumination. *Journal of Physical Chemistry Letters* **13** (2022), 7523–7531.

[41] F. Staub, H. Hempel, J. C. Hebig, et al. Beyond Bulk Lifetimes: Insights into Lead Halide Perovskite Films from Time-Resolved Photoluminescence. *Physical Review Applied* **6** (2016), 1–13.

[42] E. Cinquanta, D. Meggiolaro, S. G. Motti, et al. Ultrafast THz Probe of Photoinduced Polarons in Lead-Halide Perovskites. *Physical Review Letters* **122** (2019), 166601.

[43] E. Ugur, J. I. Khan, E. Aydin, et al. Carrier Extraction from Perovskite to Polymeric Charge Transport Layers Probed by Ultrafast Transient Absorption Spectroscopy. *Journal of Physical Chemistry Letters* **10** (2019), 6921–6928.

[44] D. Walter, A. Fell, Y. Wu, et al. Transient photovoltage in perovskite solar cells: Interaction of trap-mediated recombination and migration of multiple ionic species. *Journal of Physical Chemistry C* **122** (2018), 11270–11281.

[45] T. J. Savenije, A. J. Ferguson, N. Kopidakis, and G. Rumbles. Revealing the dynamics of charge carriers in polymer:fullerene blends using photoinduced time-resolved microwave conductivity. *Journal of Physical Chemistry C* **117** (2013), 24085–24103.

[46] T. J. Savenije, D. Guo, V. M. Caselli, and E. M. Hutter. Quantifying Charge-Carrier Mobilities and Recombination Rates in Metal Halide Perovskites from Time-Resolved Microwave Photoconductivity Measurements. *Advanced Energy Materials* **10** (2020), 1–12.

[47] D. H. Fabini, C. C. Stoumpos, G. Laurita, et al. Reentrant Structural and Optical Properties and Large Positive Thermal Expansion in Perovskite Formamidinium Lead Iodide. *Angewandte Chemie* **128** (2016), 15618–15622.

[48] F. Ruf, M. F. Aygüler, N. Giesbrecht, et al. Temperature-dependent studies of exciton binding energy and phase-transition suppression in (Cs,FA,MA)Pb(I,Br)3 perovskites. *APL Materials* **7** (2019).

[49] H. C. Woo, J. W. Choi, J. Shin, et al. Temperature-Dependent Photoluminescence of CH3NH3PbBr3 Perovskite Quantum Dots and Bulk Counterparts. *Journal of Physical Chemistry Letters* **9** (2018), 4066–4074.

[50] R. L. Milot, G. E. Eperon, H. J. Snaith, M. B. Johnston, and L. M. Herz. Temperature-Dependent Charge-Carrier Dynamics in CH3NH3PbI3 Perovskite Thin Films. *Advanced Functional Materials* **25** (2015), 6218–6227.

[51] M. C. Gélvez-Rueda, N. Renaud, and F. C. Grozema. Temperature Dependent Charge Carrier Dynamics in Formamidinium Lead Iodide Perovskite. *Journal of Physical Chemistry C* **121** (2017), 23392–23397.

[52] S. Mariotti, E. Köhnen, F. Scheler, et al. Interface engineering for high-performance, triple-halide perovskite-silicon tandem solar cells. *Science* **381** (2023), 63–69.

[53] C. Greenland, A. Shnier, S. K. Rajendran, et al. Correlating Phase Behavior with Photophysical Properties in Mixed-Cation Mixed-Halide Perovskite Thin Films. *Advanced Energy Materials* **10** (2020), 1–11.

2

How Deep Traps Affect the Charge Dynamics and Collection in $MAPbBr_3$

Wide-band-gap perovskites such as methylammonium lead bromide (MAPB) are promising materials for tandem solar cells because of their potentially high open-circuit voltage, which is yet still far below the maximum limit. The relatively short charge-carrier lifetimes deduced from TRPL measurements seem in strong contrast with the long lifetimes observed with time-resolved photoconductance measurements. This is explained by a large amount of hole defect states, $N_T > 10^{16}$ cm^{-3}, in spin-coated layers of MAPB residing at or near the grain boundaries. The introduction of hypophosphorous acid (HPA) increases the average grain size by a factor of 3 and reduces the total concentration of the trap states by a factor of 10.

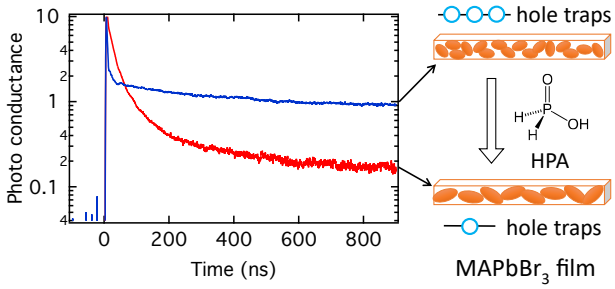

This chapter is based on

J. Zhao, V. M. Caselli, M. Bus, et al. How Deep Hole Traps Affect the Charge Dynamics and Collection in Bare and Bilayers of Methylammonium Lead Bromide. *ACS Applied Materials and Interfaces* **13** (2021), 16309–16316.

2.1. Introduction

As mentioned in Chapter 1, metal halide perovskites (MHPs) have attracted an increasing amount of attention over the past decade due to the steep increase in performance of MHP-based solar cells from an initial 3.8% in 2009 to over 26%.[1–6] The high performance is attributed to a number of interesting properties such as high optical absorption coefficients, long charge-carrier diffusion lengths, and recombination lifetimes as well as low trap state densities.[4,7,8] Their low cost and ease of processing make them also attractive for other applications including light-emitting diodes, lasers, and X-ray detectors.[9–11] Recently, tandem solar cells based on a Si bottom cell and a MHP top cell are intensively investigated since efficiencies above the Shockley-Queisser limit can be attained.[12–15] The wide band gap of 2.38 eV of methylammonium lead bromide (MAPB) perovskite makes it a promising candidate as a top cell for a tandem solar cell.[16,17] Moreover, MAPB features promising properties, such as high photoluminescence (PL) yield,[18] relatively small exciton binding energies,[19] and balanced mobility between electrons and holes.[17] In principle, the wider band gap of MAPB should potentially allow for higher open-circuit voltages (V_{OC}) essential to reach higher power conversion efficiencies (PCEs) of tandem solar cells. However, in practice, the energy gap between the E_g/e and V_{OC} for mixed halide perovskites increases with increasing ratios of Br/I.[20] For MAPB-based solar cells, the maximum reported V_{OC}'s amounts to 1.61 V,[21] which in view of the E_g of 2.38 eV, yields a deficit of 0.77 V. In comparison, for MAPI, E_g amounts to 1.59 eV and the highest reported voltage amounts to 1.26 V, yielding a gap of only 0.33 V.[22] Hence, to reach higher V_{OC}'s for the Br-containing top cell, a detailed understanding and eventual reduction of this deficit is important.

One of the most critical factors determining the efficiency of MHP-based solar cells is the presence of recombination centers. For perovskites, a large variety of defect states including point defects in the bulk, e.g., interstitials or vacancies and surface defects, such as undercoordinated halide ions or lead ions, is possible. Some of these defects form states within the forbidden band gap and lead to the trapping of excess charge carriers.[23,24] Hence, to ultimately improve solar cell efficiencies, it is particularly important to understand the origin and type of these trap states. From density functional theory calculations,[25] it has been reported that halide interstitials and lead vacancies are the most stable defects in both MAPI and MAPB. For both these materials, it is argued that halide interstitials result in slight p-type behavior. In another work, Musiienko et al. found by first-principle calculations that cation vacancies and Br interstitials are the main acceptors in MAPB.[26] However, there are no detailed experimental studies focusing on the density and the type of trap states as well as the relationship between structure and trap states in MAPB perovskites.

In this chapter, time-resolved microwave conductivity (TRMC) was used to study trap states in bare MAPB and in bilayers of MAPB with a charge selective transport layer. We start off by comparing the time-resolved PL and time-resolved photoconductance measurements on MAPB with those on MAPI. These data suggest that one type of carrier in MAPB is trapped on short timescales resulting in photoconductance decays extending into the multi-microsecond time regime. Furthermore, we investigate how these trap states are affected by the domain size, which we manipulate by the addition of a small percent of hypophosphorous acid (HPA) to the precursor solution. Previous research

on the addition of HPA has improved the electronic properties of MAPI layers remarkably. In that work, it is argued that HPA, a strong reducing agent, avoids the oxidation of I^- and in addition retards the crystallization process yielding larger crystals.[27–29] Analysis of the TRMC traces of MAPB-HPA shows a reduction of the number of trap states by an order of magnitude, which is related to the increased grain size as exposed by atomic force microscopy (AFM). Additional PL and TRMC measurements on MAPB/SO and MAPB/C_{60} bilayer systems allowed us to determine the type of deep traps. Finally, we modeled the charge-carrier dynamics in the single and bilayers to extract hole transfer rates and charge-carrier collection efficiencies. Our findings provide valuable insight into how passivation of deep trap states in MAPB affects the charge-carrier dynamics, essential for optimizing perovskite-based optoelectronic devices and designing tandem solar cells.

2.2. Results and discussion

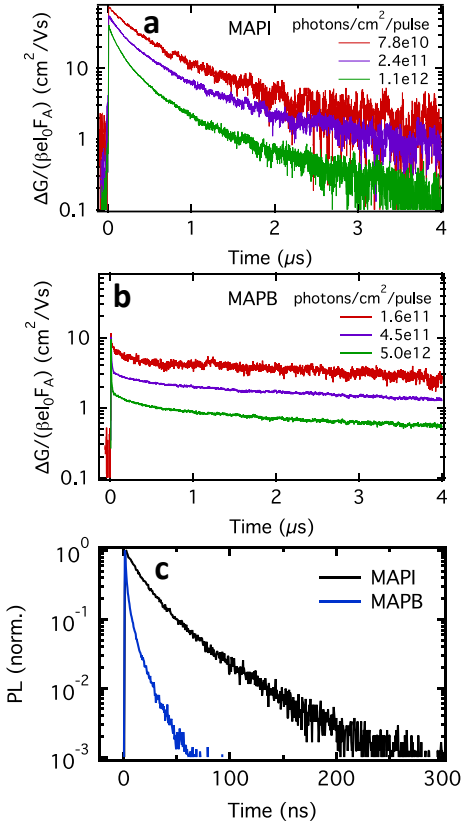

Figure 2.1: Photoconductance as a function of time for (a) MAPI and (b) MAPB recorded at intensities ranging from 10^{10} to 10^{12} photons cm^{-2} per pulse, corresponding to initial charge carrier densities of 10^{15} to 10^{17} cm^{-3}. (c) PL lifetimes of MAPI and MAPB thin films recorded using pulsed excitation at 405 nm.

MAPB thin films (~ 300 nm) were deposited on precleaned quartz substrates by spin-coating a N,N-dimethylformamide (DMF) solution containing the precursors methylammonium bromide (MABr) and lead acetate trihydrate in a 3:1 molar ratio. MAPI thin films (~ 250 nm) were prepared using the same procedure, with methylammonium iodide replacing MABr. The (100), (200) and (110), (220) main characteristic peaks in the X-ray diffraction (XRD) patterns (Figure 2A.1 in Appendices) confirm the cubic and tetragonal crystal structure of MAPB and MAPI films, respectively.[30] Absorption and fluorescence spectra of MAPI are provided in Figure 2A.2 in Appendices and correspond to previously reported spectra.[31]

Figures 2.1a and 2.1b show photoconductance traces (ΔG) normalized by the number of absorbed photons as a function of time on photoexcitation of MAPI (λ = 650 nm) and MAPB (λ = 500 nm) in a log-linear representation. The initial increase of the signal originates from the generation of free charge carriers, while the decay is attributed to recombination or to the immobilization of excess carriers by trapping. The traces recorded for MAPI are similar to those reported previously by some of us.[32–34] The signal heights for MAPI are substantially higher than that for MAPB, which can be attributed to the lower charge-carrier mobilities for the latter.[35] On increasing the laser intensity, the decay kinetics become faster, which can be explained by the fact that with higher initial charge densities the second-order band-to-band recombination leads to faster decay. Most intriguingly, the decay kinetics for the MAPB are substantially different compared to MAPI. Although at higher intensities the decay kinetics are initially faster, all traces are characterized by almost parallel tails at longer times, even extending into the microsecond timescales. Moreover, the same trend was also observed in MAPB films prepared from $PbBr_2$ (see Figure 2A.3 in Appendices), which indicates these long tails are independent of the lead precursor source. Furthermore, similar long-lived photoconductance and transient absorption traces have been previously reported for bromide-rich MHPs.[25,36]

The time-resolved photoluminescence (TRPL) traces for both materials displayed in Figure 2.1c show the opposite behavior: the lifetime of MAPB is substantially shorter than that of MAPI. Since the PL originates from the radiative decay of electrons and holes,[37] this observation implies that in MAPB one type of charge carrier is depleted within a few tens of nanoseconds. At the same time, we can deduce that the other type of charge carrier is mobile for prolonged timescales, as it is apparent from the TRMC traces. These results suggest that for MAPB, one type of carrier, is trapped on short timescales resulting in a rather different photophysical behavior in comparison to MAPI.

To further investigate the nature and origin of the trap states in MAPB, HPA was added to the precursor solution to manipulate the morphology of MAPB yielding thin films, denoted as MAPB-HPA.[38] HPA has been used as an additive in the MAPI and $MAPI_{3-x}Cl_x$ to improve the optoelectronic properties.[28,29,38,39] The XRD pattern of MAPB-HPA is very comparable to the pattern of the perovskite layer without HPA, denoted as MAPB-reference (MAPB-ref) (see Figure 2A.1 in Appendices). From X-ray photoemission spectroscopy (see Figure 2A.4 in Appendices), we observe only a small amount of P (2.5%) in the MAPB-HPA layer.

Figure 2.2a,b shows the atomic force microscopy (AFM) images of both MAPB films, respectively. It is apparent that the average perovskite domain size is significantly en-

larged on adding HPA: from ca. 200 nm to 700 nm. The substantial increase of the domain size in the HPA sample is due to the lower crystallization rate during the nucleation of perovskite, as previously reported.[28] Therefore, the total surface area related to the domain boundaries in MAPB-HPA is considerably smaller than in the MAPB-ref.

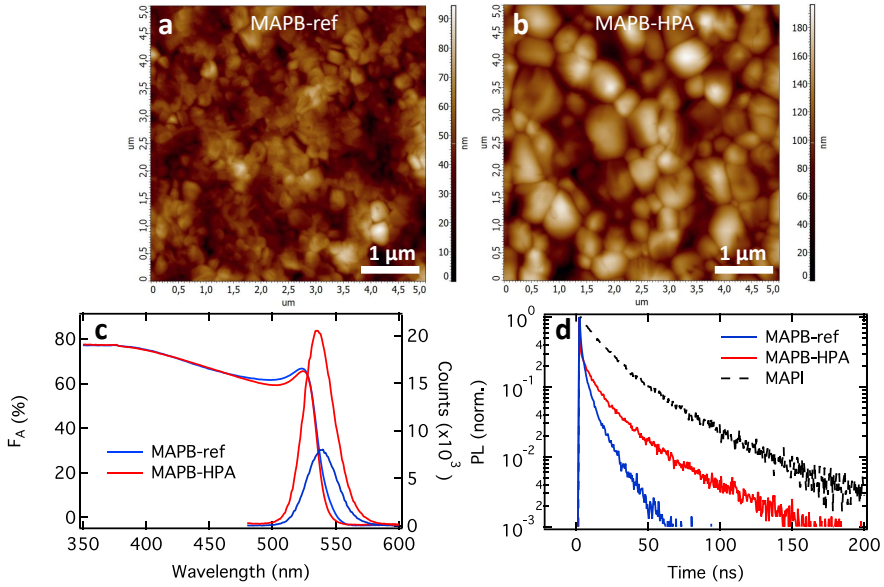

Figure 2.2: Atomic force microscopy (AFM) images for MAPB-ref (a) and -HPA-processed (b) films spin-coated on quartz substrates. (c) Fraction of light absorbed (F_A) by MAPB-ref and -HPA films (left axis) and corresponding PL spectra (right axis). (d) PL lifetimes of MAPB-ref and -HPA thin films photoexcited at 405 nm (1 MHz, 1.2×10^{12} photons cm^{-2}) recorded at the maximum emission wavelengths.

Then, we investigated the optical properties of these two MAPB perovskite layers. Figure 2.2c displays the fraction of absorbed light (F_A) and the PL emission of both thin films. For both samples, we find the contribution of the characteristic excitonic absorption at 524 nm to the absorption spectra. For MAPB-ref, a small red shift of approximately 5 nm of the absorption onset and of the maximum PL are observed. More importantly, the PL intensity of MAPB-HPA is about 4 times higher than that of MAPB-ref. Furthermore, TRPL measurements show that the PL lifetime of MAPB-HPA is increased by a factor of 2 in comparison to MAPB-ref. The improved optical properties of MAPB-HPA are expected to result from suppressed nonradiative recombination pathways due to the reduction of the number of trap states.[40] Assuming that the trap states are largely located at the grain surface, this decrease might be reasonably related to the reduced total surface area of MAPB-HPA. Photoluminescence mapping would be a better approach to try and provide ideas about the location of traps in the future.

To gain more insight into the trapping process by intra-band-gap states we measured the photoconductance traces in MAPB-ref and -HPA thin films (see Figure 2.3). A number of observations can be made on addition of HPA: first, the maximum signal height

is higher. This value represents the product of the free charge carrier generation yield, φ, and the sum of the electron and hole mobility, $\sum\mu$. Based on the thermal energy at 300 K and the exciton binding energy of MAPB, which is in the range of 14-60 meV,[19,41] we expect that the predominant part of the excitons is dissociated into free charges as detailed in Figure 2A.5 in Appendices. Therefore, we can assume φ is close to unity at room temperature for both samples. Apart from this increased signal height, we observe a substantial reduction in the initial decay kinetics on addition of HPA. To extract the mobilities and rate constants for various processes, we modeled photoconductance traces using a kinetic model (Figure 2.4) previously successfully used to describe the photophysical processes in MAPI.[32,36] For MAPB, the fits are calculated by taking into account the processes indicated by the black arrows and assuming slightly n-doped material as will be discussed later on. (see Appendices for a used set of differential Equations 2A.2 to 2A.5). The fits are added in Figure 2.3 as solid lines and are in good agreement with the experimental traces. All kinetic parameters are collected in Table 2.1.

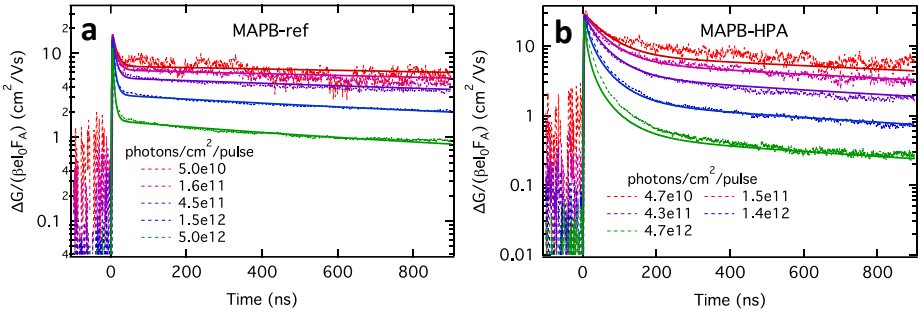

Figure 2.3: Photoconductance as a function of time for MAPB-ref (a) and processed with HPA (b) thin films for intensities ranging from 10^{10} to 10^{12} photons cm^{-2} per pulse (λ = 500 nm), corresponding to initial charge carrier densities of 10^{15} to 10^{17} cm^{-3}. The full lines are fits to the data points as described in the text.

Table 2.1: Kinetic fitting parameters extracted from TRMC traces for bare MAPB and MAPB/SO Bilayers.

	MAPB-ref	MAPB-ref/SO	MAPB-HPA	MAPB-HPA/SO
k_2 [$\times10^{-9}$ cm^3s^{-1}]	5.5	6.5	2.1	2.8
k_T [$\times10^{-9}$ cm^3s^{-1}]	2	2	2.5	2.5
k_D [$\times10^{-10}$ cm^3s^{-1}]	0.45	3.2	1.5	50
N_T [$\times10^{15}$ cm^{-3}]	35	35	3.5	3.5
n_0 [$\times10^{15}$ cm^{-3}]	3.5	3.5	3.5	3.5
k_h [$\times10^{6}$ s^{-1}]	-	5	-	10
k_e [$\times10^{6}$ s^{-1}]	-	<0.1	-	7
$\sum\mu$ [$cm^2(Vs)^{-1}$]	19	19	30	30

The $\sum\mu$ values are 19 and 30 $cm^2(Vs)^{-1}$ for MAPB-ref and MAPB-HPA, respectively. We attribute this increase to the expanded domain sizes of MAPB-HPA since the mea-

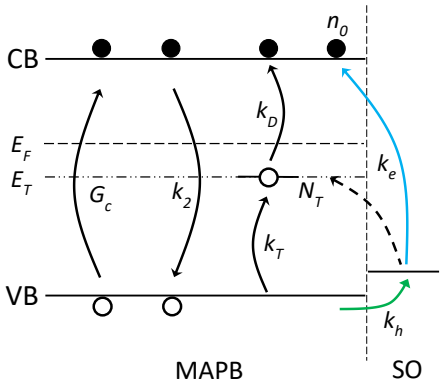

Figure 2.4: Kinetic model of charge carrier processes initiated by photo-excitation of MAPB. G_c represents the photogeneration of charge carriers; k_2 depicts the second-order recombination rate. Hole trap-mediated recombination is described by a trapping rate k_T and depopulation rate k_D. The Fermi level, E_F is located above the trap level, E_T implying that the material is n-type doped. In the presence of a SO hole transport layer, charges can be injected into SO with k_h (green arrow) and further recombine with electrons via k_e (blue arrow).

sured mobility at 8.5 GHz can be reduced by the domain boundaries. The resulting restriction in the charge-carrier motion reduces the measured effective AC mobility.[42] Also, k_2 representing the second-order recombination process is reduced from 5.5×10^{-9} to 2.1×10^{-9} cm^3s^{-1}. In addition to radiative band-to-band recombination, nonradiative trap-mediated decay can also give rise to the second-order decay process as we and others have experimentally observed.[32,37] Obviously, the reduced surface area of the MAPB-HPA has resulted in a lowering of the nonemissive part of k_2. This agrees with the enhancement in PL for the MAPB-HPA film. More importantly, the concentration of deep trap states, N_T, for MAPB-HPA is one order of magnitude lower as compared to the ref sample. The origin of the reduction of N_T could be attributed to the reduced total surface area of the MAPB-HPA layer. Moreover, the substantially higher N_T values in MAPB in comparison to those reported for MAPI[33] explain the differences observed with (TR)PL and TRMC, as shown in Figure 2.1.

Knowing the rate constants for the various processes allows us to model the TRPL signal, which is given by:[32]

$$TRPL = k_2 (n + n_0) p \tag{2.1}$$

Since the laser pulse used for the time-correlated single-photon counting (TCSPC) measurements is different from the TRMC experiments, we have to adapt the G_C term in the set of coupled differential equations (see Equations 2A.2 to 2A.5 in Appendices). Solving the equations again numerically yields the time-dependent concentrations of n and p. Via this approach the TRPL signals for both MAPB films are calculated and shown in Figure 2A.6 in Appendices. Although there is no exact match with Figure 2.2d, the similarity with experimental TRPL traces is clearly present.

To obtain more information about the type of traps and how trap states affect the charge collection, we deposited Spiro-OMeTAD (SO) (~ 250 nm) as a hole transport layer or C_{60} as an electron transport layer (~ 30 nm) on top of the same perovskite layers studied above. The absorption spectra of SO and C_{60} as well as their corresponding bilayers are shown in Figure 2A.7 in Appendices. For all bilayers, we observe a clear reduction in PL intensity on the introduction of SO as well as of C_{60} in comparison with the bare MAPB layer, indicating charge transfer to the transport layer. For the bilayers based on MAPB-HPA, the PL quenching was substantially stronger than for the MAPB-ref based bilayers (Figure 2A.8 in Appendices). In Figure 2.5 the normalized photoconductance traces of the bare ref and HPA perovskites together with their bilayer systems are shown. The samples were excited through the transport layer using an excitation wavelength of 500 nm. The non-normalized traces are provided in Figure 2A.9 in Appendices.

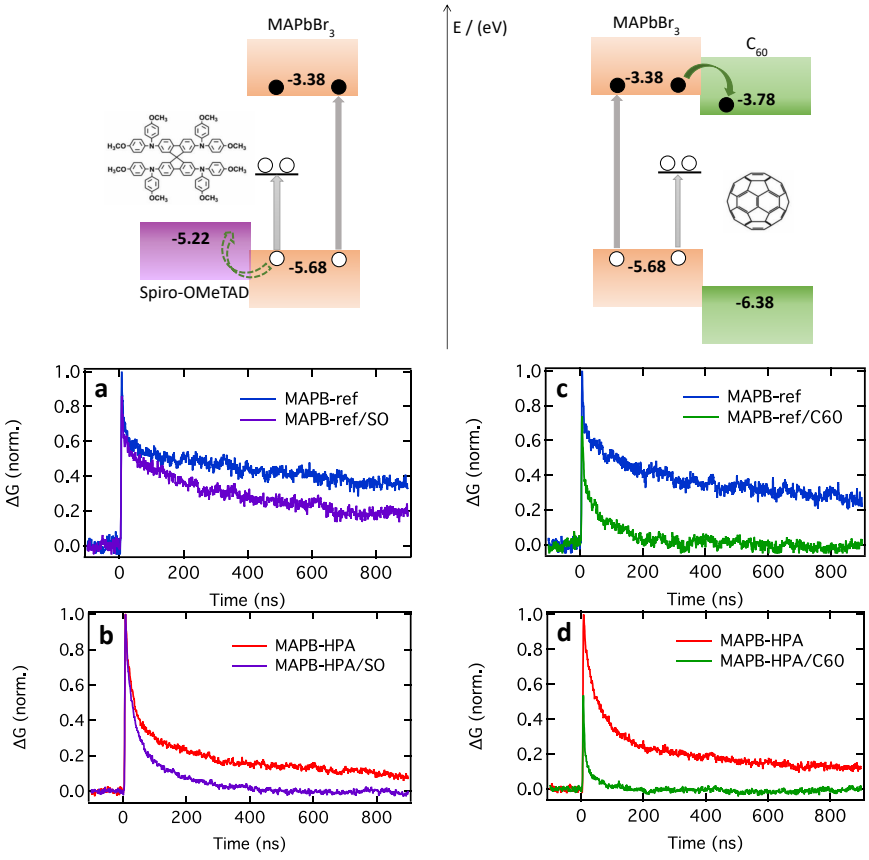

Figure 2.5: Energy diagrams and charge carrier processes occurring upon photoexcitation of MAPB/SO (top, left) and MAPB/C_{60} (top, right). TRMC traces for neat MAPB and MAPB/SO bilayers (a, b) and MAPB/C_{60} bilayers (c, d) for both ref (a, c) and HPA processed (b, d) samples recorded at initial charge carrier densities of 3×10^{15} cm^{-3} (λ = 500 nm). Maximum signal sizes of the single layers are normalized to 1, while bilayers are normalized with the same factor.

For MAPB-ref/SO a relatively small deviation from the single layer is visible, while for the MAPB-HPA/SO, the tail of the TRMC signal is decaying much faster than the bare layer (see also Figures 2A.10a and 2A.10b in Appendices for a log-linear representation). Note that the mobility of charges in SO (and also in C_{60}) is more than an order of magnitude smaller than in MHPs and that only mobile carriers contribute to the photoconductance.[43,44] The fact that the introduction of the SO layer on the MAPB-ref layer does not appreciably change the TRMC trace demonstrates that the holes do not contribute substantially to the TRMC signal in neither the bare layer nor the bilayer. Hence, in both samples, the excess electrons are responsible for the TRMC signal. From here, we can conclude that the majority of the excess holes in the bare MAPB-ref layer are rapidly trapped. Holes captured in trap states are not mobile and thus do not contribute to the conductance. This result is understandable in view of the initial charge-carrier density of 3×10^{15} cm^{-3} and the much larger value of N_T for the MAPB-ref. For the MAPB-HPA/SO bilayer, the situation is somewhat different since N_T is close to the initial charge-carrier density and hence partial hole transfer can be expected. As mentioned above, those injected holes in SO hardly contribute to photoconductance due to their low mobility. From the faster decay kinetics for both bilayers in comparison to the bare MAPB layers, we conclude that the recombination of holes with the mobile conduction band electrons is enhanced by the introduction of SO, which we will discuss in more detail below.

For both MAPB/C_{60} bilayers, we observe a drop in the initial signal size and a severe reduction in a lifetime as compared to the single perovskite layer (a log-linear representation is shown in Figures 2A.10c and 2A.10d in Appendices) The reduction of the initial photoconductance could be partially due to the fact that C_{60} has a nonzero absorption at 500 nm. More importantly, the long-lived tails clearly visible in the bare MAPB layer disappear in both MAPB/C_{60} bilayers. Realizing that the dominant part of the holes is trapped in the MAPB layer, and the fact that the TRMC signal goes quickly back to zero, proves that electron transfer from both MAPB layers into C_{60} is efficient which is in accordance with the PL quenching.

The above explanation for the TRMC measurements on the double layers brings us to the conclusion that the dominant type of traps in MAPB layers are hole traps. Then, we examine the decay kinetics in both MAPB/SO bilayers. For both bilayers, we observe a reduction in charge-carrier lifetime with those in bare MAPB layers. In contrast, we reported previously for MAPI/SO bilayers an enhancement in charge-carrier lifetimes, which was attributed to the fact that after charge transfer the charges are physically separated.[31,33] To obtain more insight into the recombination processes, we fitted the bilayers using the kinetic model of Figure 2.4 completed by an additional charge transfer process to the transport layer with rate constant k_h and recombination of a hole in the SO with a conduction band electron with rate k_e as indicated in green and blue, respectively. The TRMC traces and corresponding fits are provided in Figure 2A.11 in Appendices for a range of intensities. The used kinetic parameters are added to Table 2.1. For both MAPB/SO bilayers, we observe values of $5-10 \times 10^6$ s^{-1} for k_h, which confirms that hole transfer to the transport layer occurs. Although most found parameters are very comparable to the corresponding bare MAPB, we observe an increase of more than an order of magnitude for k_D. Obviously, the introduction of SO enhances the emptying of

occupied trap states. To explain this observation, we argue that (i) the location of the trap states is near or at the surface of the grains. This explains that for MAPB-HPA the effect is more severe than for the MAPB-ref layer since for the latter most of the grain boundaries are not in direct contact with SO. (ii) The energetic position of the trap states is located close to or above the highest occupied molecular orbital (HOMO) level of SO. In this way, the surface states offer an additional decay path for holes that have been injected into SO, as indicated by the dashed arrow in Figure 2.4. The increased decay rate from the trap states can be attributed to the fact that the injected holes in SO induce an internal electric field pulling electron density toward the interface. The increased electron concentration enhances the recombination of trapped holes with conduction band electrons. Both effects lead basically to an increase of the trap-mediated recombination, which might be one of the key reasons for the higher voltage deficit in the MAPB-based cells in comparison to the MAPI cells. However, we cannot exclude that the fast interfacial recombination observed at the interface between MAPB/C_{60} might be another reason for the voltage deficit. The lower concentration or absence of surface states for MAPI explains why, in contrast to MAPB/SO bilayers, an elongation of the charge-carrier lifetimes on hole transfer to SO is observed (see Figure 2A.12 in Appendices).[31,33]

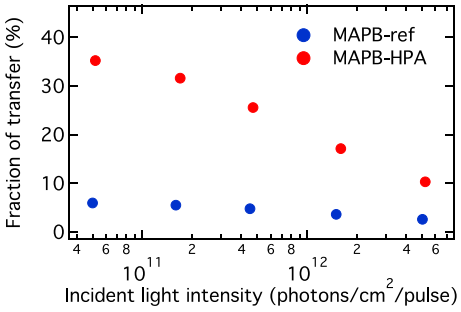

Figure 2.6: Fraction of initial photoinduced charge carriers that undergo charge transfer to the SO transport layer.

Knowing all the rate constants describing the bare and bilayer system allows us to determine the fraction of the initially generated excess carriers by the laser pulse, which has undergone charge transfer into SO. For both bilayers, this fraction is displayed in Figure 2.6 versus the laser intensity. In particular, at low intensities where the second-order recombination is less prominent, we can conclude that the charge collection for the MAPB-ref is almost a factor of 10 less efficient. This is in line with the much weaker PL quenching efficiency in the MAPB-ref/SO bilayer than in MAPB-HPA/SO. Although under steady-state illumination conditions the results may be somewhat different, we conclude that for MAPB-ref/SO hole collection is hampered, reducing the efficiency of a MAPB-ref based solar cell.

Combining all found information regarding the trap states in MAPB brings us to the following key features: spin-coated MAPB is characterized by a large amount of defect hole states, $N_T > 10^{16}$ cm^{-3}, residing at or near the surface of the perovskite grains. The introduction of HPA in the spin-coating solution considerably increases the grain sizes

and at the same time reduces the total concentration of the trap states by an order of magnitude. As mentioned in the Introduction section, undercoordinated atoms at the surface might give rise to such surface traps. The larger crystals of the MAPB-HPA layer resulting in the reduced surface area of the MAPB-HPA layer is likely the major origin of the reduced concentration of the defect states.

2.3. Conclusions

In this chapter, the optoelectronic properties of MAPB, which are markedly different from those of MAPI, are described, in particular how trap states affect the charge-carrier dynamics and charge collection. By addition of HPA to the precursor solution, the average crystal domain size is found to increase by more than a factor of 3, as revealed by AFM. Analysis of the photoconductance traces recorded by electrodeless time-resolved microwave measurements reveals that positive charges are trapped on short timescales. Most importantly, the concentration of deep trap states, N_T, for MAPB-HPA is reduced from 35×10^{15} to 3.5×10^{15} cm^{-3}. Furthermore, k_2 comprising both radiative and nonradiative second-order recombination, is reduced by a factor of 2. Both observations can be attributed to the reduced surface area of MAPB-HPA. From additional PL and TRMC measurements on MAPB-ref/SO and MAPB-HPA/C_{60} double layers, we conclude that charge transfers into C_{60} and SO occurs. However, for MAPB-ref/SO, the hole collection is hampered by the presence of excessive amounts of hole traps. In contrast to MAPI/SO, we observe a reduction of the charge-carrier lifetime in bilayers, which we attribute to the fact that interfacial recombination from the injected holes via the trap states is possible. More insight into the manipulation of the concentration of intra-band-gap states and their effect on the charge-carrier dynamics will contribute to a more complete understanding of the optoelectronic properties of MAPB. This is essential for optimizing perovskite-based optoelectronic devices in particular for bromide-containing perovskite top cells for application in tandem solar cells.

2.4. Experimental methods

Preparation of MHP films

Quartz substrates were rinsed with acetone and ethanol in an ultrasonic bath for 10 min each. Subsequently, oxygen plasma treatment was performed prior to layer deposition. To prepare MAPB/MAPI precursor solution, methylamine bromide (336 mg, 3.0 mmol) / methylamine iodide (480 mg, 3.0 mmol) and lead acetate trihydrate ($PbAc_2 \bullet 3H_2O$) (379 mg, 1.0 mmol) were dissolved in anhydrous N, N-Dimethylformamide (DMF) (1.77 mL). For the preparation of the MAPB-HPA layers, 4 μL of an HPA stock solution was added to the precursor solution yielding a 7.5% molar ratio of HPA to $PbAc_2$. The perovskite solutions were spin-coated on the substrates at 2000 rpm for 45 s and then annealed at 100 °C for 5 min after drying for 10 min at room temperature. For the Spiro-OMeTAD layer, a 75 mg mL^{-1} chlorobenzene solution was prepared, which was spin-coated at 1500 rpm for 45 s. The C_{60} layer (30 nm) was thermally evaporated.

Photoconductance measurements

The Time-Resolved Microwave Conductivity (TRMC) technique was determined to investigate the photoconductance as a function of time using an excitation wavelength of 500 nm for MAPB and 650 nm for MAPI. With this technique, the reduction in microwave power ($\Delta P(t)/P$) induced by a laser pulse (repetition rate: 10 Hz) was related to the change in conductance ($\Delta G(t)$) by the sensitivity factor K

$$\frac{\Delta P(t)}{P} = -K\Delta G(t) \tag{2.2}$$

The TRMC signal is expressed in the product of mobility ($\mu_e + \mu_h$) and charge-carrier yield φ, which was calculated from the maximum change in photoconductance ΔG_{max}

$$\varphi\left(\mu_e + \mu_h\right) = \frac{\Delta G_{max}}{F_A I_0 e \beta} \tag{2.3}$$

where F_A is the fraction of light absorbed by the sample at the excitation wavelength, I_0 is the laser intensity in the number of photons per unit area per pulse, e is the elementary charge, and β is the ratio of the inner dimensions of the microwave cell. The samples were placed in a sealed microwave cell inside the glovebox to ensure that they were not exposed to ambient conditions during the measurement.

Optical characterization

Absorption spectra were recorded with a PerkinElmer Lambda 1050 spectrophotometer equipped with an integrated sphere. The samples were placed inside the sphere to measure the total fraction of reflected and transmitted light (F_{R+T}). Then the fraction of absorbed light (F_A) was calculated by:

$$F_A = 1 - F_{R+T} \tag{2.4}$$

Photoluminescence spectra and lifetimes in the main text were carried out by using an Edinburgh LifeSpec spectrometer equipped with a single-photon counter. The films were excited at 405 nm using a picosecond pulsed diode laser ($I_0 = 1.2 \times 10^{12}$ photons cm^{-2}) at 1 MHz. On recording the transients at a repetition rate of 100 kHz limited no significant changes were observed. Photoluminescence spectra in the Appendices were recorded using an Edinburgh FLS980 spectrometer at an excitation wavelength of 470 nm.

Structural characterization

X-ray diffraction patterns were conducted on a Brucker D8 diffractometer in a Bragg-Brentano configuration using Co-Kα ($\lambda = 1.79$ Å) radiation.

The atomic force microscopy measurements were performed on an NTMDT Ntegra Aura AFM system in semicontact mode. The cantilevers used were Nanosensors PPP-NCHR with a resonance frequency of 350 kHz. The only post-processing performed was a linear line by line flattening.

X-ray photoemission spectroscopy (XPS) measurements were conducted using a Thermo Fisher Kα surface analysis machine.

References

[1] J. H. Heo, S. H. Im, J. H. Noh, et al. Efficient inorganic-organic hybrid heterojunction solar cells containing perovskite compound and polymeric hole conductors. *Nature Photonics* **7** (2013), 486–491.

[2] J. H. Im, C. R. Lee, J. W. Lee, S. W. Park, and N. G. Park. 6.5% Efficient Perovskite Quantum-Dot-Sensitized Solar Cell. *Nanoscale* **3** (2011), 4088–4093.

[3] H. S. Kim, C. R. Lee, J. H. Im, et al. Lead iodide perovskite sensitized all-solid-state submicron thin film mesoscopic solar cell with efficiency exceeding 9%. *Scientific Reports* **2** (2012), 591.

[4] A. Kojima, K. Teshima, Y. Shirai, and T. Miyasaka. Organometal halide perovskites as visible-light sensitizers for photovoltaic cells. *Journal of the American Chemical Society* **131** (2009), 6050–6051.

[5] H. Zhou, Q. Chen, G. Li, et al. Interface engineering of highly efficient perovskite solar cells. *Science* **345** (2014), 542–546.

[6] NREL. *Best Research-Cell Efficiencies: Rev. October 2023*. 2023.

[7] S. D. Stranks, G. E. Eperon, G. Grancini, et al. Electron-hole diffusion lengths exceeding 1 micrometer in an organometal trihalide perovskite absorber. *Science* **342** (2013), 341–344.

[8] E. M. Hutter, G. E. Eperon, S. D. Stranks, and T. J. Savenije. Charge Carriers in Planar and Meso-Structured Organic-Inorganic Perovskites: Mobilities, Lifetimes, and Concentrations of Trap States. *Journal of Physical Chemistry Letters* **6** (2015), 3082–3090.

[9] Y. Cao, N. Wang, H. Tian, et al. Perovskite light-emitting diodes based on spontaneously formed submicrometre-scale structures. *Nature* **562** (2018), 249–253.

[10] M. Saliba, T. Matsui, J. Y. Seo, et al. Cesium-containing triple cation perovskite solar cells: Improved stability, reproducibility and high efficiency. *Energy and Environmental Science* **9** (2016), 1989–1997.

[11] H. Wei, Y. Fang, P. Mulligan, et al. Sensitive X-ray detectors made of methylammonium lead tribromide perovskite single crystals. *Nature Photonics* **10** (2016), 333–339.

[12] D. P. McMeekin, G. Sadoughi, W. Rehman, et al. A mixed-cation lead mixed-halide perovskite absorber for tandem solar cells. *Science* **351** (2016), 151–155.

[13] I. J. Park, J. H. Park, S. G. Ji, et al. A Three-Terminal Monolithic Perovskite/Si Tandem Solar Cell Characterization Platform. *Joule* **3** (2019), 807–818.

[14] M. H. Futscher and B. Ehrler. Efficiency Limit of Perovskite/Si Tandem Solar Cells. *ACS Energy Letters* **1** (2016), 863–868.

[15] S. Albrecht, M. Saliba, J. P. Correa Baena, et al. Monolithic perovskite/silicon-heterojunction tandem solar cells processed at low temperature. *Energy and Environmental Science* **9** (2016), 81–88.

[16] J. H. Heo and S. H. Im. CH3NH3PbBr3–CH3NH3PbI3Perovskite–Perovskite Tandem Solar Cells with Exceeding 2.2 V Open Circuit Voltage. *Advanced Materials* **28** (2016), 5121–5125.

[17] A. M. Ulatowski, A. D. Wright, B. Wenger, et al. Charge-Carrier Trapping Dynamics in Bismuth-Doped Thin Films of MAPbBr3Perovskite. *Journal of Physical Chemistry Letters* **11** (2020), 3681–3688.

[18] N. Droseros, G. Longo, J. C. Brauer, et al. Origin of the Enhanced Photoluminescence Quantum Yield in MAPbBr3 Perovskite with Reduced Crystal Size. *ACS Energy Letters* **3** (2018), 1458–1466.

[19] M. Baranowski and P. Plochocka. Excitons in Metal-Halide Perovskites. *Advanced Energy Materials* **10** (2020).

[20] E. Aydin, M. De Bastiani, and S. De Wolf. Defect and Contact Passivation for Perovskite Solar Cells. *Advanced Materials* **31** (2019), 1–20.

[21] C. G. Wu, C. H. Chiang, and S. H. Chang. A perovskite cell with a record-high-Voc of 1.61 v based on solvent annealed CH3NH3PbBr3/ICBA active layer. *Nanoscale* **8** (2016), 4077–4085.

[22] N. Liu and C. Y. Yam. First-principles study of intrinsic defects in formamidinium lead triiodide perovskite solar cell absorbers. *Physical Chemistry Chemical Physics* **20** (2018), 6800–6804.

[23] X. Jiang, J. Hoffman, C. C. Stoumpos, M. G. Kanatzidis, and E. Harel. Transient Sub-Band-Gap States at Grain Boundaries of CH3NH3PbI3 Perovskite Act as Fast Temperature Relaxation Centers. *ACS Energy Letters* **4** (2019), 1741–1747.

[24] L. Chen, Y. Y. Tan, Z. X. Chen, et al. Toward Long-Term Stability: Single-Crystal Alloys of Cesium-Containing Mixed Cation and Mixed Halide Perovskite. *Journal of the American Chemical Society* **141** (2019), 1665–1671.

[25] S. G. Motti, D. Meggiolaro, S. Martani, et al. Defect Activity in Lead Halide Perovskites. *Advanced Materials* **31** (2019), 1–11.

[26] A. Musiienko, J. Pipek, P. Praus, et al. Deciphering the effect of traps on electronic charge transport properties of methylammonium lead tribromide perovskite. *Science Advances* **6** (2020).

[27] W. Zhang, S. Pathak, N. Sakai, et al. Enhanced optoelectronic quality of perovskite thin films with hypophosphorous acid for planar heterojunction solar cells. *Nature Communications* **6** (2015).

[28] T. Abzieher, F. Mathies, M. Hetterich, et al. Additive-Assisted Crystallization Dynamics in Two-Step Fabrication of Perovskite Solar Cells. *Physica Status Solidi (A) Applications and Materials Science* **214** (2017), 1–9.

[29] T. Leijtens, G. E. Eperon, A. J. Barker, et al. Carrier trapping and recombination: The role of defect physics in enhancing the open circuit voltage of metal halide perovskite solar cells. *Energy and Environmental Science* **9** (2016), 3472–3481.

[30] D. Shi, V. Adinolfi, R. Comin, et al. Low trap-state density and long carrier diffusion in organolead trihalide perovskite single crystals. *Science* **347** (2015), 519–522.

[31] V. M. Caselli, Z. Wei, M. M. Ackermans, et al. Charge Carrier Dynamics upon Subbandgap Excitation in Methylammonium Lead Iodide Thin Films: Effects of Urbach Tail, Deep Defects, and Two-Photon Absorption. *ACS Energy Letters* **5** (2020), 3821–3827.

[32] E. M. Hutter, G. E. Eperon, S. D. Stranks, and T. J. Savenije. Charge Carriers in Planar and Meso-Structured Organic-Inorganic Perovskites: Mobilities, Lifetimes, and Concentrations of Trap States. *Journal of Physical Chemistry Letters* **6** (2015), 3082–3090.

[33] E. M. Hutter, J. J. Hofman, M. L. Petrus, et al. Charge Transfer from Methylammonium Lead Iodide Perovskite to Organic Transport Materials: Efficiencies, Transfer Rates, and Interfacial Recombination. *Advanced Energy Materials* **7** (2017).

[34] T. J. Savenije, D. Guo, V. M. Caselli, and E. M. Hutter. Quantifying Charge-Carrier Mobilities and Recombination Rates in Metal Halide Perovskites from Time-Resolved Microwave Photoconductivity Measurements. *Advanced Energy Materials* **10** (2020), 1–12.

[35] L. M. Herz. Charge-Carrier Mobilities in Metal Halide Perovskites: Fundamental Mechanisms and Limits. *ACS Energy Letters* **2** (2017), 1539–1548.

[36] D. Guo, Z. Andaji Garmaroudi, M. Abdi-Jalebi, S. D. Stranks, and T. J. Savenije. Reversible Removal of Intermixed Shallow States by Light Soaking in Multication Mixed Halide Perovskite Films. *ACS Energy Letters* **4** (2019), 2360–2367.

[37] M. Abdi-Jalebi, Z. Andaji-Garmaroudi, S. Cacovich, et al. Maximizing and stabilizing luminescence from halide perovskites with potassium passivation. *Nature* **555** (2018), 497–501.

[38] W. Zhang, S. Pathak, N. Sakai, et al. Enhanced optoelectronic quality of perovskite thin films with hypophosphorous acid for planar heterojunction solar cells. *Nature Communications* **6** (2015).

[39] N. K. Noel, M. Congiu, A. J. Ramadan, et al. Unveiling the Influence of pH on the Crystallization of Hybrid Perovskites, Delivering Low Voltage Loss Photovoltaics. *Joule* **1** (2017), 328–343.

[40] D. Luo, R. Su, W. Zhang, Q. Gong, and R. Zhu. Minimizing non-radiative recombination losses in perovskite solar cells. *Nature Reviews Materials* **5** (2020), 44–60.

[41] N. Sestu, M. Cadelano, V. Sarritzu, et al. Absorption F-Sum Rule for the Exciton Binding Energy in Methylammonium Lead Halide Perovskites. *Journal of Physical Chemistry Letters* **6** (2015), 4566–4572.

[42] O. G. Reid, M. Yang, N. Kopidakis, K. Zhu, and G. Rumbles. Grain-Size-Limited Mobility in Methylammonium Lead Iodide Perovskite Thin Films. *ACS Energy Letters* **1** (2016), 561–565.

[43] D. Shi, X. Qin, Y. Li, et al. Spiro-OMeTAD single crystals: Remarkably enhanced charge-carrier transport via mesoscale ordering. *Science Advances* **2** (2016).

[44] P. W. Liang, C. C. Chueh, S. T. Williams, and A. K. Jen. Roles of fullerene-based interlayers in enhancing the performance of organometal perovskite thin-film solar cells. *Advanced Energy Materials* **5** (2015), 1–7.

Appendices

2.A. Appendices

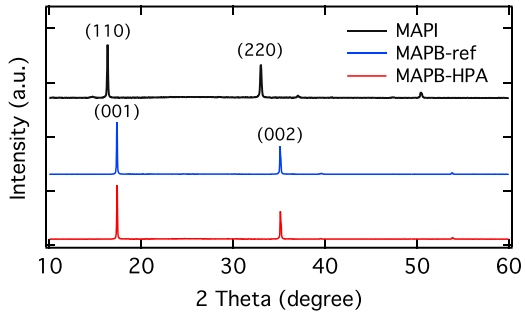

Figure 2A.1: X-ray diffraction (XRD) pattern using Co-Kα (λ = 1.79 Å) radiation of spin-coated MAPI, MAPB-ref, and MAPB-HPA processed thin films.

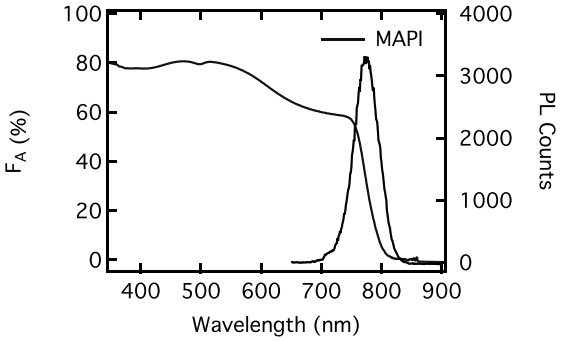

Figure 2A.2: Fraction of light absorbed (F_A) by MAPI films (left axis) and corresponding PL spectra (right axis).

The fraction of excitations resulting in free charges (x) can be calculated according to the Saha Equation:[1]

$$\frac{x^2}{1-x} = \frac{1}{n}\left(\frac{2\pi m^* k_B T}{h^2}\right)^{\frac{3}{2}} e^{\frac{E_B}{k_B T}} \tag{2A.1}$$

[1] V. D'innocenzo, et al. Excitons versus free charges in organo-lead tri-halide perovskites. *Nature Communications* **5** (2014), 3586.

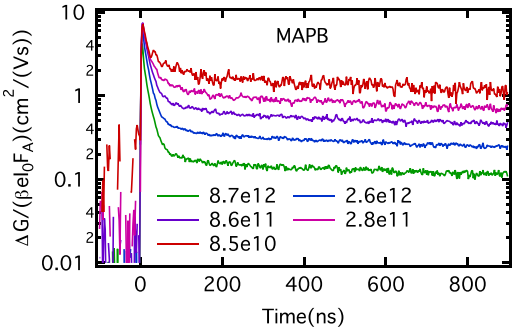

Figure 2A.3: Photoconductance in MAPB thin film prepared from $PbBr_2$ precursor.

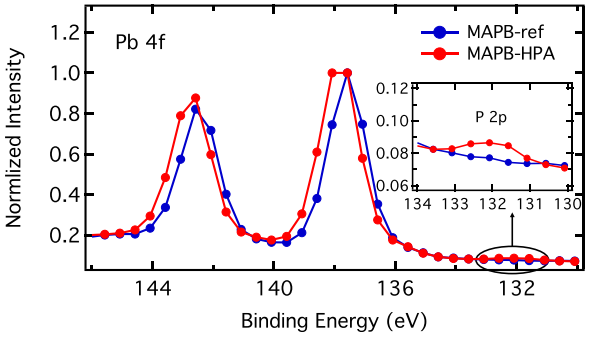

Figure 2A.4: The XPS spectra of Pb 4f spectra for both MAPB-ref and -HPA films spin-coated on quartz. The insert shows a magnification of the black circle area, corresponding to the P 2p spectra.

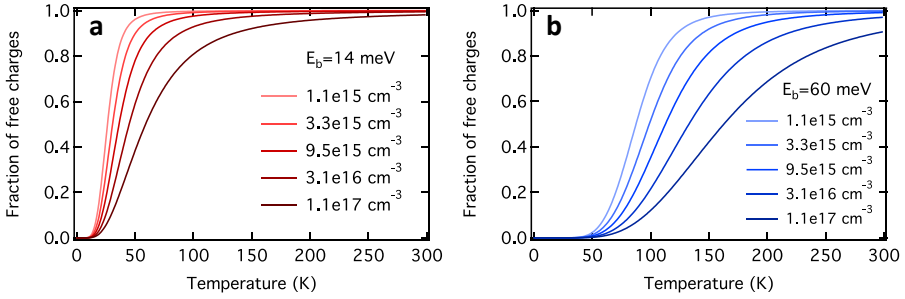

Figure 2A.5: Fraction of the initial charge carrier population leading to free charges as a function of temperature for exciton binding energies of 14 meV (a) and 60 meV (b) for charge carrier densities ranging from 10^{15} to 10^{17} cm^{-3}.

where n is the total initial excitation density and $\left(\frac{2\pi m^* k_B T}{h^2}\right)^{\frac{3}{2}}$ represents the density of states in the conduction band. Figure 2A.5 show the fraction, x as a function of temperature for initial excitation densities ranging from 10^{15} to 10^{17} cm^{-3} for binding energies of 14 meV and 60 meV. From these figures, we learn that the yield of free charges at room temperature is close to unity for both binding energies at room temperature.

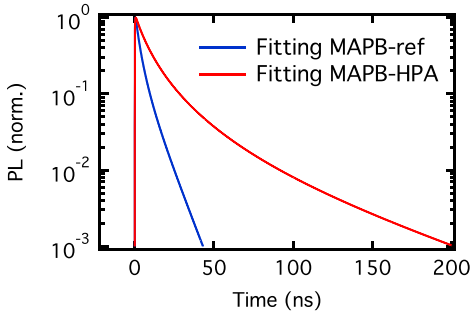

Figure 2A.6: The TRPL traces calculated by solving the differential equation for both MAPB-ref and -HPA films.

TRMC fitting differential equations:

$$\frac{dn_e}{dt} = G_C - k_2 (n_e + n_0) n_h - k_D n_t (n_e + n_0) \tag{2A.2}$$

$$\frac{dn_h}{dt} = G_C - k_2 (n_e + n_0) n_h - k_T (N_T - n_t) n_h \tag{2A.3}$$

$$\frac{dn_t}{dt} = k_T (N_T - n_t) n_h - k_D n_t (n_e + n_0) \tag{2A.4}$$

$$\frac{dn_{TL}}{dt} = k_h n_h - k_e (n_e + n_0) \tag{2A.5}$$

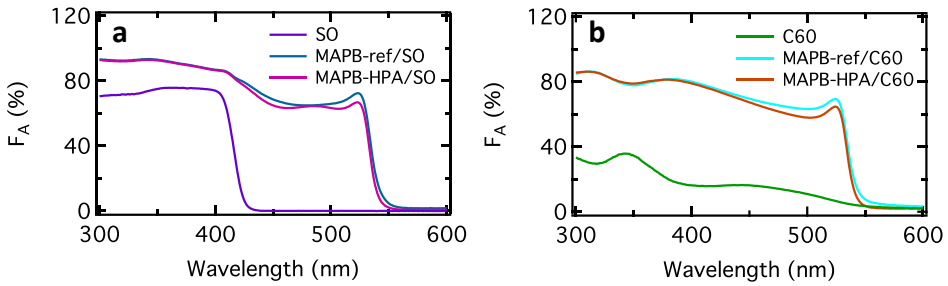

Figure 2A.7: Fraction of light absorbed (F_A) by MAPB/SO and SO (a) and MAPB/C_{60} and C_{60} (b) for MAPB-ref and processed with HPA films.

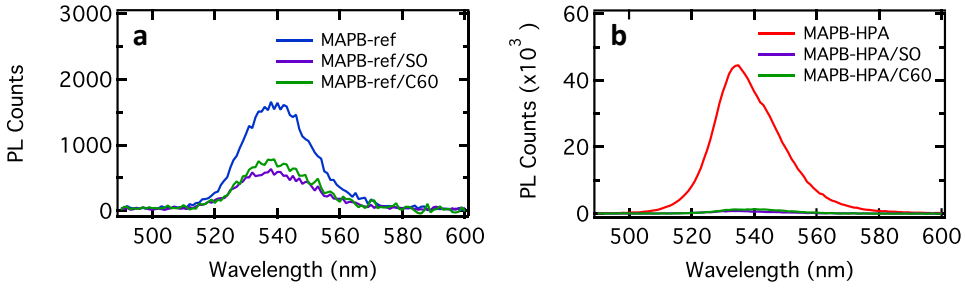

Figure 2A.8: Photoluminescence emission spectra for neat MAPB and MAPB/SO and C_{60} bilayers in MAPB-ref (a) and -HPA (b) thin films excited at 470 nm.

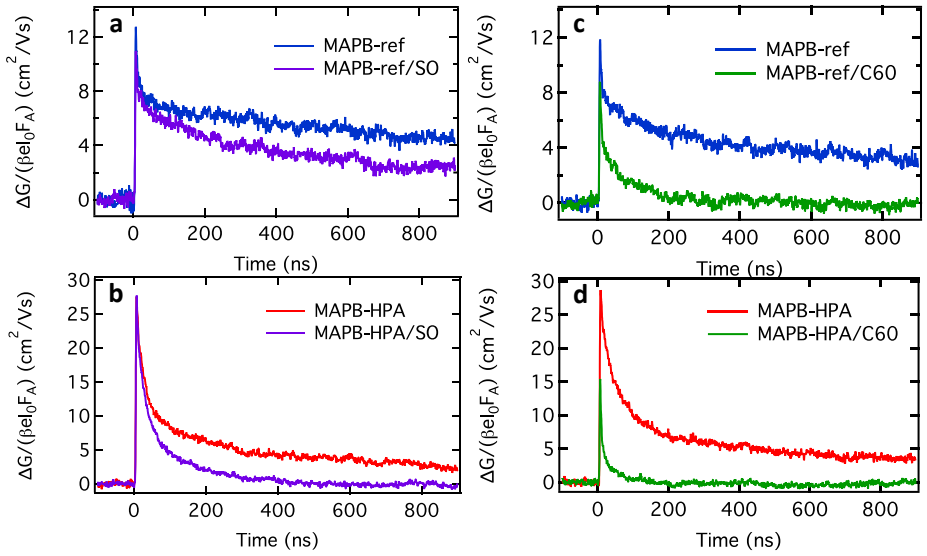

Figure 2A.9: The original TRMC traces for neat MAPB and MAPB/SO bilayers (a, b) and MAPB/C_{60} bilayers (c, d) for both ref (a, c) and HPA (b, d) samples recorded at initial charge carrier densities of 3×10^{15} cm^{-3} ($\lambda = 500$ nm).

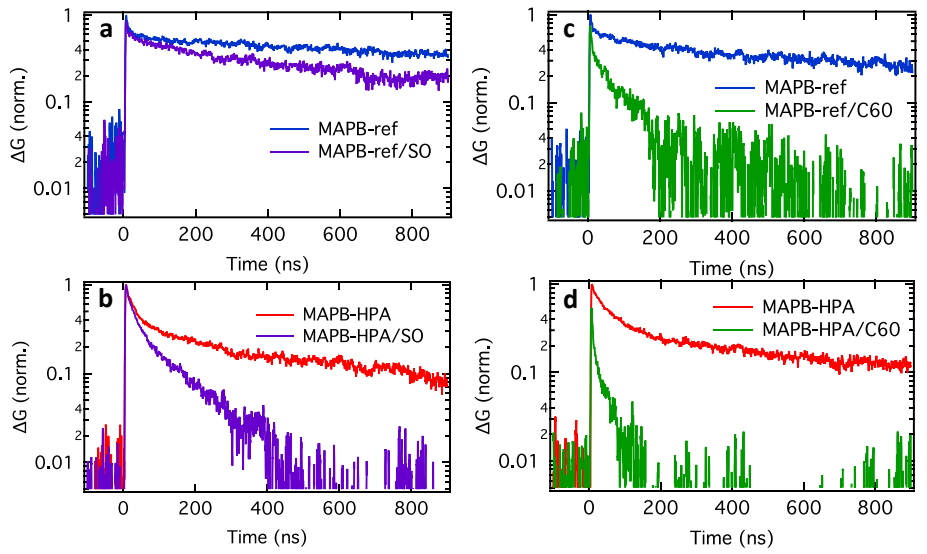

Figure 2A.10: TRMC traces on a logarithm-linear scale for neat MAPB and MAPB/SO bilayers (a, b) and MAPB/C_{60} bilayers (c, d) for both ref (a, c) and HPA (b, d) samples recorded at initial charge carrier densities of 3×10^{15} cm^{-3} ($\lambda = 500$ nm).

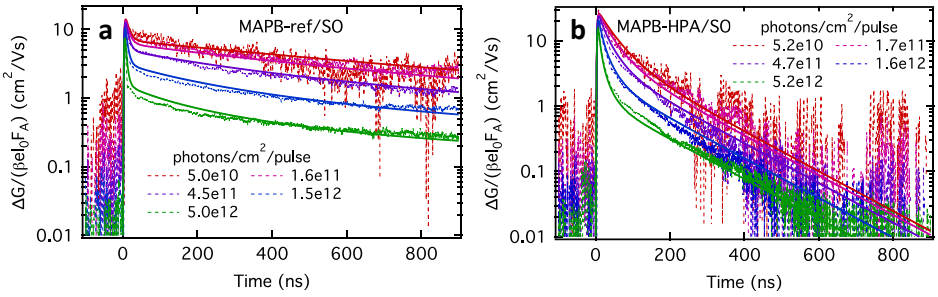

Figure 2A.11: TRMC traces for MAPB-ref and -HPA/SO bilayers (a, b) recorded at incident light intensities ranging from 10^{10} to 10^{12} photons cm^{-2} per pulse ($\lambda = 500$ nm), corresponding to initial charge carrier densities of 10^{15} to 10^{17} cm^{-3}. The full lines are fits to the experimental data, using the model in Figure 2.4, where holes can be injected via k_h in the presence of SO layer and the kinetic parameters listed in Table 2.1.

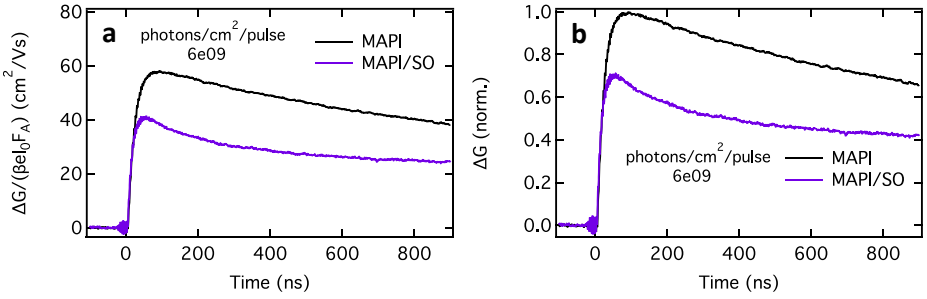

Figure 2A.12: (a) The original TRMC traces for neat MAPI and MAPI/SO bilayers samples recorded at an incident light intensity of 6×10^9 photons cm^{-2} per pulse ($\lambda = 650$ nm), corresponding to initial charge density of 1×10^{14} cm^{-3}. (b) Maximum signal sizes of the single layers are normalized to 1, while the bilayers are normalized with the same factor.

3

Carrier Dynamics in Co-evaporated $MAPbI_3$ with a Gradient in Composition

In this chapter, the structural and optoelectronic properties of co-evaporated $MAPbI_3$ films with a gradient in composition are analyzed. The I/Pb atomic ratio indicates MAI deficiencies that become more prominent with thicker films, resulting in differently n-doped regions across the thick $MAPbI_3$ films. More importantly, an elongation of the charge carrier lifetimes is observed on increasing thickness. These observations can be explained by the fact that excess carriers separate under the influence of the electric field, preventing rapid decay in the thick films.

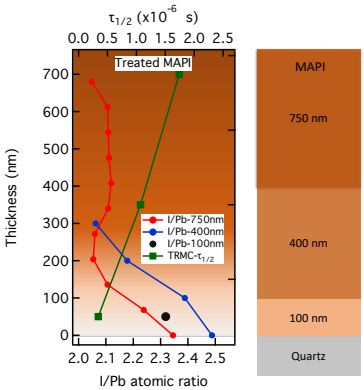

This chapter is based on

J. Zhao, J. Li, X. Liu, et al. Charge Carrier Dynamics in Co-evaporated $MAPbI_3$ with a Gradient in Composition. *ACS Applied Energy Materials* **5** (2022), 7049–7055.

3.1. Introduction

With unprecedented progress, metal halide perovskite (MHP) based solar cells have reached power conversion efficiencies (PCEs) of over 26% and are the most promising candidates for next-generation solar cells.[1–6] These remarkable developments are attributed to their intrinsic properties such as high absorption coefficients, relatively high charge carrier mobilities, and long lifetimes as well as low densities of electronically active trap states.[1,7,8] At the same time, MHPs are also emerging in other applications, such as X-ray detectors, light-emitting diodes, field effect transistors, and memory devices.[9–11]

In general, the production of the majority of MHP solar cells is based on solution-processed deposition techniques. However, deposition by thermal co-evaporation under vacuum conditions is an attractive alternative approach to obtaining uniform and compact thin films.[12–16] Elimination of solvents is beneficial to the fabrication of tandem solar cells and the preservation of the environment. More importantly, this method is scalable and allows precise control of the film thickness, even on textured surfaces.[17,18] The first work published in 2013 using thermal co-evaporation to deposit $MAPbI_{3-x}Cl_x$ reported a PCE of 15.4% for small-area devices.[12] To date, the PCEs of perovskite solar cells based on methylammonium lead iodide ($MAPbI_3$) prepared by co-evaporation reach over 20% in both n-i-p[19–24] and p-i-n[17] configurations on the small-area devices and over 18% on perovskite minimodules.[19,23]

Although the deposition of $MAPbI_3$ by wet chemical deposition has been extensively examined, the effects of the co-evaporation processing parameters on the structural and electronic properties of $MAPbI_3$ films are complex and still under investigation. Recently, it was reported that the deposition speed and polarity of the substrate can substantially affect the preferred crystal orientation and morphology of $MAPbI_3$ films.[14] In addition, by tuning the deposition rates of the precursors during the co-evaporation, the crystalline phase of $MAPbI_3$ can be varied from the cubic to the tetragonal phase.[25] On the other hand, Li et al. have shown that another key advantage of co-evaporation is the possibility to customize the active film for different device architectures. Recently, we demonstrated that using $MAPbI_3$ with a gradual change in precursors leading to a gradient in composition, a PCE above 20% can be achieved in a p-i-n configuration.[19] Co-evaporated perovskites have also shown to be very promising in enhancing the optoelectronic properties of light-emitting field effect (FET) transistors. Thanks to the reduced ionic motion and absence of tensile stress, it was possible to obtain light emission even at room temperature,[26] which was not possible with spin-coated perovskites.[27]

Herein, we study how the charge carrier dynamics are affected in $MAPbI_3$ films grown with a gradient in composition formed by applying a gradient in pressure during the growth process. We have used a constant source temperature for both precursors, that is, methylammonium iodide (MAI) and PbI_2, which results in a slowly varying background pressure during the deposition.[19] Since the perovskite growth can be largely influenced by the substrate material,[28] in this Chapter, we analyzed $MAPbI_3$ films with different thicknesses deposited on quartz substrates. We performed X-ray diffraction (XRD), scanning electron microscopy (SEM), and X-ray photoemission spectroscopy (XPS) to investigate the structural properties of the deposited films, with a focus on the I/Pb atomic ratio. It has been previously shown that variations in stoichiometry can affect the Fermi

level of the film.[29] Hence, we argue that on Fermi level alignment, an internal field is formed in the 400 and 750 nm $MAPbI_3$ films. This internal field has profound effects on the charge carrier dynamics as determined by time-resolved microwave conductivity (TRMC) measurements. We also analyzed the effect of a potassium-acetate (MAI + KAc) treatment previously developed for co-evaporated $MAPbI_3$ films on the gradient-grown $MAPbI_3$ films.[19,24] We show that the treatment does not impact the charge carrier lifetimes or trap densities but increases the effective carrier mobilities slightly. These findings provide more fundamental insight into how a gradual composition of co-evaporated $MAPbI_3$ films affects the optoelectronic properties.

3.2. Results and discussion

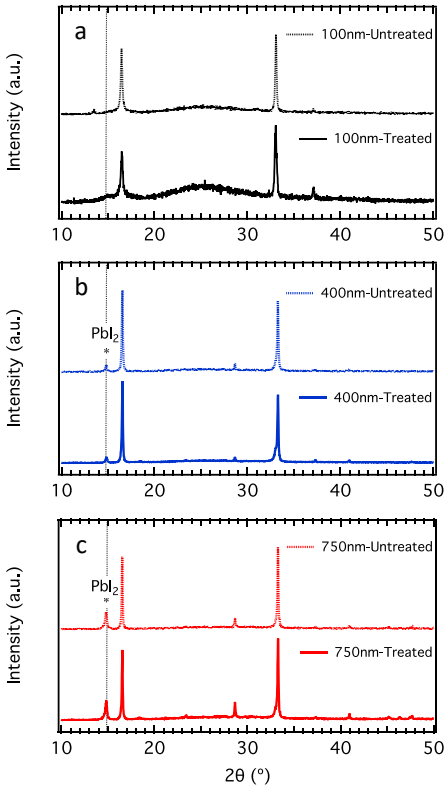

Figure 3.1: Normalized XRD patterns (Co Kα X-radiation) for untreated and treated co-evaporated $MAPbI_3$ films with the thicknesses of 100 (a), 400 (b), and 750 nm (c). The dashed vertical line indicates the diffraction peak position of excess PbI_2.

To investigate the optoelectronic properties of graded-$MAPbI_3$ films, films with different thicknesses (100, 400, and 750 nm) were deposited on quartz substrates by co-evaporation of PbI_2 and MAI, according to the procedure previously described.[17,19,24]

The pristine graded $MAPbI_3$ films are denoted hereafter as "untreated" films, while the graded $MAPbI_3$ films which underwent a post-deposition spin-coating treatment with an isopropanol solution containing KAc and MAI (MAI + KAc)[19] are denoted as "treated". Absorbance spectra of all $MAPbI_3$ films are shown in Figure 3A.1 in Appendices. Spectra of treated $MAPbI_3$ films are comparable to those of the pristine films. In the inset of Figure 3A.1 in Appendices the wavelength-dependent absorption spectra, determined from the reflection and transmission spectra (Figure 3A.2 in Appendices) are reported. For all samples, absorption coefficients close to 10^5 cm^{-1} at 500 nm have been found, similar to previously reported values for MAPbI3.[30]

Figure 3.1 shows normalized XRD patterns obtained with Co Kα X-radiation for the $MAPbI_3$ films of different thicknesses made by co-evaporation. The XRD measurements were performed in the Bragg-Brentano configuration. For all films, the two main characteristic peaks of the cubic perovskite phase located at 16.6° and 33.3°[31] indicate the good crystallization of $MAPbI_3$ with a highly preferred orientation. On increasing the thickness, the peak at 14.8° attributed to PbI_2 is visible in the 400 nm film (Figure 3.1b) and becomes even more pronounced in the 750 nm $MAPbI_3$ film (Figure 3.1c), implying that excess PbI_2 is far more present in the thicker samples.[32] On the other hand, in untreated and treated $MAPbI_3$ films with identical thickness, the amount of excess PbI_2 just slightly varies. It is worth noting that compositional information of various $MAPbI_3$ thin films at different depths was measured previously using grazing incidence X-ray diffraction with incident angles varying from 0.5° to 10°.[32] Those XRD patterns indicated that excess PbI_2 gradually decreases going from the top surfaces to the bottom in both thick $MAPbI_3$ films. This is in agreement with the low PbI_2 content found in the present 100 nm thick films.

In general, $MAPbI_3$ films reside at room temperature in the tetragonal phase, which is thermodynamically the most favorable phase.[33] In dry atmospheres, it is also possible that $MAPbI_3$ adopts a cubic crystal structure at room temperature using deposition by co-evaporation.[25] The absence of the (211) peak for these graded $MAPbI_3$ films prepared by co-evaporation and deposited on quartz substrates suggests that these $MAPbI_3$ films might have also a cubic phase (see Figure 3A.3 in Appendices). To obtain more structural information, XRD patterns were measured by varying the temperature stepwise between 25 °C and 85 °C (Figure 3A.4 in Appendices). Figures 3A.4a and 3A.4b show the (200) diffraction peak of the 750 nm $MAPbI_3$ film, which shifts towards lower angles upon heating due to the thermal expansion of the lattice.[34] The (200) peak is asymmetric with a minor contribution at lower angles (see Figure 3A.4c in Appendices), indicating the presence of some tetragonal phase. On increasing the temperature, the latter contribution becomes even smaller, which might be related to the tetragonal-to-cubic conversion. This indicates that the cubic phase coexists with the tetragonal phase in the 750 nm co-evaporated $MAPbI_3$ films on quartz at room temperature. We speculate that the excess PbI_2 in combination with the quartz substrate might hamper complete conversion to the tetragonal phase. Such phase retention of $MAPbI_3$ films on quartz substrates has been reported previously.[35]

To examine the morphology and grain size in the $MAPbI_3$ films with thickness and treatment, SEM was performed and top-view images are shown in Figure 3A.5 in Appendices. In agreement with previous reports on $MAPbI_3$ films prepared by co-

evaporation,[15,16,19,21,24,32] all $MAPbI_3$ films consist of relatively small crystalline domains (~ 100 nm) forming a uniform and compact film. In previous work,[19] we have already shown that the combined MAI and KAc treatment effectively improved the film morphology as proved by the reduced presence of pin-holes and the increased grain sizes for 750 nm films, and here we show that this result is consistent for all three thicknesses investigated.

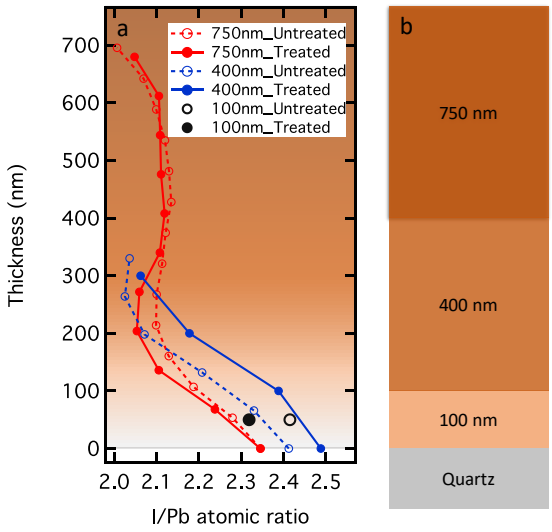

Figure 3.2: XPS depth profile (a). The atomic percentage ratio of I (iodine) and Pb (lead) is displayed as a function of thickness for various $MAPbI_3$ films. For 100 nm $MAPbI_3$ films, two black dots represent the average I/Pb atomic ratio of the entire 100 nm film. For the thicker $MAPbI_3$ films, the curves show the trends of the I/Pb atomic ratio evolving with the thickness during the growth of $MAPbI_3$. Note: Due to the effects of surface adsorbents at the surface including, for example, oxygen, the first measurement before etching has been excluded for all films. The schematic diagram of $MAPbI_3$ films deposited on quartz with the corresponding thicknesses (b).

To obtain compositional information on the $MAPbI_3$ thin films, we performed a depth profile analysis using XPS. In Figure 3.2 the depth profiles of the atomic I/Pb ratio are shown for all films. The detailed atomic percentage plots of all elements in $MAPbI_3$ films are provided in Figure 3A.6 in Appendices. For the 100 nm thick film, we used the average ratio in the center of the $MAPbI_3$ film yielding ratios of 2.42 and 2.32 for the untreated and treated films, respectively.

For both thicker films, two regimes in the I/Pb ratio can be discerned. In the first 200 nm next to the quartz substrate, the I/Pb ratio reduces from about 2.4 to 2.1, implying that the MAI deficiency rises with increasing film thickness. Above 200 nm, the I/Pb ratio remains fairly constant yielding a rather homogeneous, thick top film. Ratios below 3 indicate an MAI deficiency, however, the obtained I/Pb ratio might to some extent, diverge from the actual ratio due to inaccuracies in the detection and analysis. Nevertheless, trends in I/Pb atomic ratios within a single sample as well as differences in the I/Pb atomic ratios between various samples can still be compared and analyzed. In ad-

dition, trends in I/Pb atomic ratios are consistent with XPS results previously reported, showing that I/Pb ratios at the top surface reduced from 2.7±0.3 for the 100 nm $MAPbI_3$ film to 2.2±0.3 for the 750 nm $MAPbI_3$ film.[32]

To confirm the elemental compositions of the $MAPbI_3$ films, we performed additional electron dispersive spectroscopy (EDS). In Figures 3A.7 and 3A.8 in Appendices, the average atomic ratios of I/Pb in the entire film of 400 and 750 nm are found to be 2.8 and 2.5, respectively. Although these values are higher than those found by XPS, the trend is similar. Moreover, the XPS, as well as EDS results, are in line with the conclusions from XRD showing an excess of PbI_2 for the 400 nm and 750 nm.

As expected, the trend of the I/Pb ratio followed the background pressure during the deposition,[32] which is dominated by the partial pressure of MAI.[28] Hence a reduction in the vacuum pressure leads to a decrease in the deposition rate of MAI, which thus results in the increasing MAI deficiency in the top part of the thick $MAPbI_3$ films.

As previously reported, an MAI deficiency or an excess of PbI_2 can lead to n-type doping of the $MAPbI_3$ film.[29,36–40] With increasing MAI deficiencies the film becomes more n-type doped i.e. the Fermi level increases as shown also by the ultraviolet photoelectron spectroscopy (UPS) data in our previous paper.[32] Hence, we conclude that the initial part close to the substrate is less n-doped than the top part. To understand how this affects the charge carrier dynamics, we put forward a simplified band structure diagram as provided in Figure 3.3 consisting of 2 n-type semiconductors but with different Fermi energy levels. In equilibrium an internal electric field is formed, forcing the excess electrons to drift towards the top part, while holes drift towards the bottom region. This hypothesis implies that light-induced excess carriers will be rapidly separated by drift independent from the optical excitation side, resulting in longer charge carrier lifetimes in the thick $MAPbI_3$ films.

To further verify our hypothesis regarding the band diagram, we carried out TRMC experiments. Note that using this approach we can probe excess carriers as long as they are mobile. Figure 3.4 shows photoconductance traces (ΔG) normalized by the number of absorbed photons as a function of time. The initial increase of the signal originates from the generation of free charge carriers, while the decay is attributed to the immobilization of excess charge carriers via trapping or the recombination of electrons and holes. With increasing the light intensity, the decay kinetics become faster, which is due to enhanced second-order electron-hole recombination (see Figure 3A.9 in Appendices). More importantly, on increasing the thickness of the $MAPbI_3$ films the lifetimes of mobile carriers become substantially longer for both untreated (Figure 3.4a) and treated films (Figure 3.4b). This is in line with the assumption that in thick $MAPbI_3$ films the internal electric field separates the excess holes and electrons, suppressing recombination and leading to longer charge carrier lifetimes. In addition, excitation at longer wavelengths (see Figure 3A.10 in Appendices), leading to a more homogeneous excitation profile within the thick perovskite layers (see Figure 3A.12 in Appendices), yields similar decay kinetics, which is in agreement with our model. The decay kinetics are only slightly slower than those displayed by time-resolved photoluminescence (TRPL) (See Figure 3A.11 in Appendices and ref[19]). While TRPL is only sensitive to radiative band-to-band recombination, TRMC probes carriers in the bands providing a complementary picture of the charge carrier dynamics in perovskites, as also previously observed in lat-

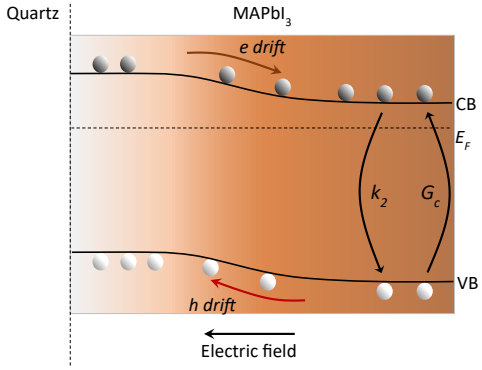

Figure 3.3: Simplified band diagram of a co-evaporated /ceMAPbI3 film with a gradient composition assuming the top part is more heavily n-type doped than the bottom part. On Fermi level alignment, a depletion film with an internal electric field is formed. Hence, on optical excitation, excess holes and electrons are separated by the internal electric field independent of the excitation side. G_c represents the photogeneration of charge carriers; k_2 depicts the second-order recombination rate.

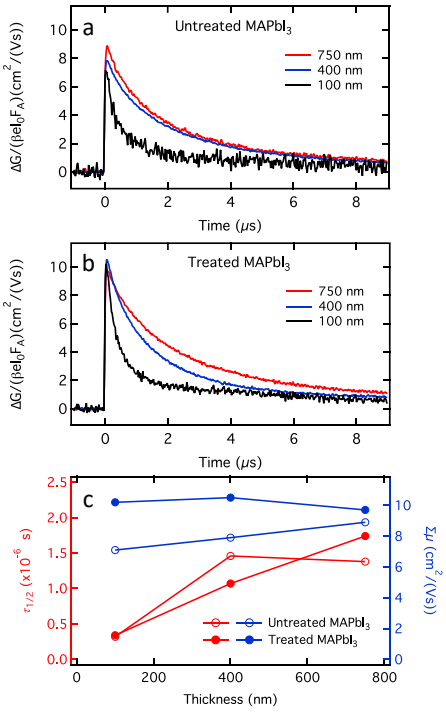

Figure 3.4: TRMC traces for untreated (a) and treated (b) with the thickness of 100, 400, and 750 nm recorded on excitation at 500 nm with incident light intensities corresponding to initial charge carrier densities of 10^{14} cm^{-3} and normalized for the amount absorbed photons. In (c) the half lifetime (left axis) and mobility (right axis) extracted from TRMC traces as a function of thickness for both untreated and treated $MAPbI_3$ films are shown.

eral perovskite homojunction.[41] For both untreated and treated films the signal heights which are corrected for the number of absorbed photons, are almost independent of the film thickness, meaning that the yield and mobility for the different thicknesses are very comparable.

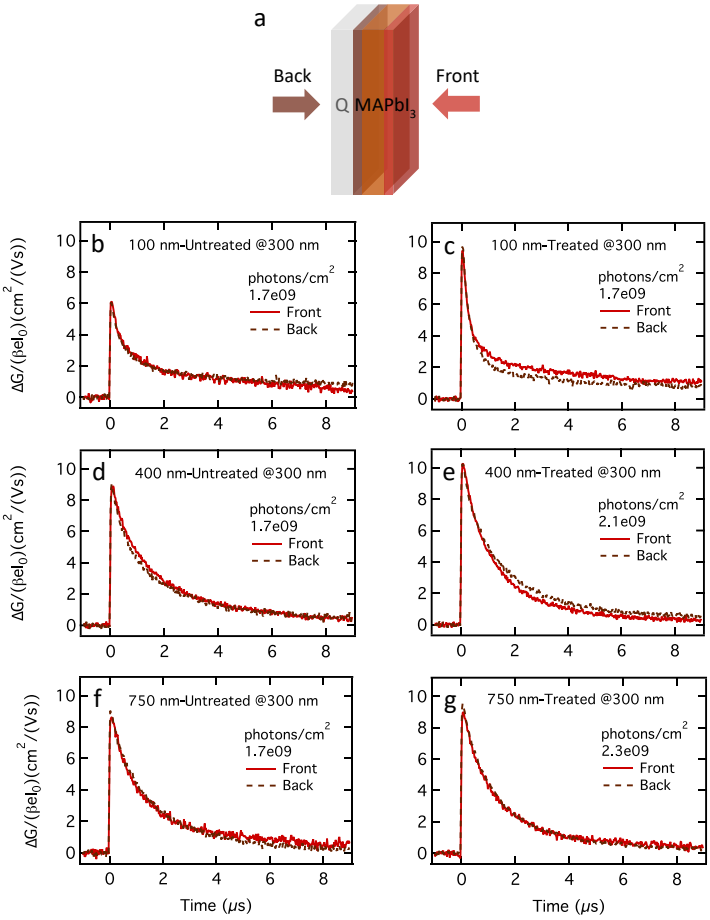

Figure 3.5: Schematic representation of laser illumination from the backside (Q: quartz) and front side (a). Intensity-normalized TRMC traces for (b, c) 100, (d, e) 400, and (f, g) 750 nm evaporated $MAPbI_3$ films recorded on excitation at 300 nm for front (brick red solid lines) and back (dark red dashed lines) excitation at an incident intensity of around 2×10^9 photons cm^{-2} per pulse. Left and right panels are for untreated and treated $MAPbI_3$, respectively.

Figure 3.4c shows a 20% increase in the maximum signal height on post-treatment. Given the low exciton binding energy of approximately 15 meV of $MAPbI_3$,[42] we can assume that the free charge carrier generation yield, φ, is close to unity at room temperature for $MAPbI_3$. Therefore, we conclude that the summation of electron and hole mobilities, $\sum\mu$ increases from ~ 8.5 to 11.2 $cm^2(Vs)^{-1}$ for the untreated and treated $MAPbI_3$,

respectively. This increase in effective mobility can be related to the expanded crystal domain size, as previously shown in spin-coated films[43] induced here by the KAc+MAI treatment.

To further study the large difference in charge carrier lifetimes, we measured the photoconductance using either front- or back-side excitation at a wavelength of 300 nm (Figure 3.5a). Since the penetration depth at 300 nm is less than 100 nm (see Figure 3A.11 in Appendices), we can selectively excite the top (using the front side) or bottom part (using the back side) of the $MAPbI_3$ film. Previously, TRMC traces recorded with front and back illumination showed at very short timescales of tens of nanoseconds a variation in rise time, which was linked to the presence of excess PbI_2 at the top surface for the 400 and 750 nm films.[19] In Figures 3.5b-g, the intensity normalized photoconductance traces of $MAPbI_3$ films recorded on excitation from both sides on 100 times longer timescales are shown. For the 100 nm film (Figure 3.5b,c), the front- and back-side TRMC traces do not reveal appreciable differences in the charge carrier dynamics. This is consistent because identical regions are probed regardless of the illumination side. Interestingly also for both thick films overlapping TRMC traces are found for excitation from the front- and back-side (Figure 3.5d-g). The negligible differences in the charge carrier lifetime in the bottom and top parts imply that in both cases the internal electric field effectively separates the excess carriers. This means electrons are effectively pulled towards the top part while holes drift towards the substrate side. By comparing Figures 3.5d with 3.5e, and 3.5f with 3.5g, we conclude that the untreated and treated films with identical thickness show comparable trends. This implies that it is not the post-treatment but the actual growth in film thickness during the co-evaporation deposition process that is responsible for the elongation of charge carrier lifetimes. The gradual composition as discussed above is in line with these observations. In addition, we can rule out that the $MAPbI_3$ region facing the quartz surface is of lower quality.

3.3. Conclusions

In this Chapter, the structural and optoelectronic properties of co-evaporated $MAPbI_3$ films with compositional gradients with and without potassium acetate treatment are investigated. XPS depth analysis shows that the I/Pb atomic ratio decreases with depth, indicating MAI deficiencies become more prominent with thicker films, resulting in differently n-doped regions. We suggest that on equilibration of the Fermi levels in these differently n-doped regimes, a depletion film is formed. To investigate how the band diagram affects the optoelectronic properties, TRMC was used showing a consistent elongation of the charge carrier lifetimes with increasing thickness. This can be explained by the drift of excess carriers, induced by the internal electric field, leading to physical separation and preventing rapid recombination. TRMC results on selective excitation at 300 nm prove that charge transport of holes and electrons to the top and bottom part of the film, respectively occurs equally well. There is no sign that the quality of the initially formed film is inferior to the top part in terms of mobility or trap state density. In addition, we observed an increase in the electrons and holes mobilities by 20% when introducing the MAI + KAc treatment, which can be related to the enlarged grain size of treated $MAPbI_3$. The results from this work provide valuable insight into the optoelectronic properties of $MAPbI_3$ films with a graded composition.

3.4. Experimental methods

Preparation of the $MAPbI_3$ films

The $MAPbI_3$ perovskite film was deposited on amorphous quartz substrates with various thicknesses using a co-evaporation deposition method developed in previous works.[19,24,32] The substrates were attached to a rotating plate (10 rpm rotation speed) without temperature control (i.e., floating temperature) and the target to substrate distance was around 30 cm. The perovskite was deposited by co-evaporating PbI_2 powder (TCI) and MAI powder (Lumtec) in effusion sources. The chamber was first pumped down to a high vacuum condition of $< 8 \times 10^{-6}$ Torr. Then PbI_2 source was heated at 260 °C and MAI at 100 °C, respectively. After the MAI temperature increased to >70 °C, the chamber pressure increased to $> 2 \times 10^{-5}$ Torr. The total deposition time was around 20 min for 100 nm film, 100 min for 400 nm film, and 180 min for 750 nm film.17 For the treated films, the as-prepared $MAPbI_3$ perovskite film was post-treated by 20 mM KAc and MAI (1:1 in molar ratio) mixed solution in isopropanol (IPA). The pristine film and post-treated film were annealed at 100 °C for 30 min, according to the procedure previously described.[19,24]

Structural characterization

X-ray photoemission spectroscopy measurements were conducted using a Thermo Fisher K-α surface spectrometer with a monochromatic Al Kα X-ray beam. XPS depth profiles are collected by etching with an ionized Ar gun. Elemental quantification based on survey spectra from which a Shirley-type background was subtracted. This analysis is performed with the Advantage software.

X-ray diffraction patterns were conducted on a Bruker D8 ADVANCE diffractometer in Bragg-Brentano configuration using Co-Kα (λ = 1.79 Å) radiation at room temperature. Temperature-dependent X-ray diffraction patterns were performed with a Bruker D8 DISCOVER diffractometer (Cu-Kα, λ = 1.54 Å) in combination with an Anton Paar XRK 900 Reactor chamber. The measurements were performed in a Bragg-Brentano configuration with a variable slit size to keep the footprint on the sample constant. The temperature was stepwise changed to 5 K/min and the measurements were performed under vacuum. The dwell time was set to 5 min.

The morphologies of perovskite films were characterized using SEM (FESEM; JEJOL JSM-7600F). The perovskites were deposited on glass/FTO substrates. Electron dispersive spectroscopy spectra were carried out on SEM (JEOL; JSM-6010LA) using a Silicon Drift Detector.

References

[1] A. Kojima, K. Teshima, Y. Shirai, and T. Miyasaka. Organometal halide perovskites as visible-light sensitizers for photovoltaic cells. *Journal of the American Chemical Society* **131** (2009), 6050–6051.

[2] J. H. Im, C. R. Lee, J. W. Lee, S. W. Park, and N. G. Park. 6.5% Efficient Perovskite Quantum-Dot-Sensitized Solar Cell. *Nanoscale* **3** (2011), 4088–4093.

[3] H. S. Kim, C. R. Lee, J. H. Im, et al. Lead iodide perovskite sensitized all-solid-state submicron thin film mesoscopic solar cell with efficiency exceeding 9%. *Scientific Reports* **2** (2012), 591.

[4] J. H. Heo, S. H. Im, J. H. Noh, et al. Efficient inorganic-organic hybrid heterojunction solar cells containing perovskite compound and polymeric hole conductors. *Nature Photonics* **7** (2013), 486–491.

[5] H. Zhou, Q. Chen, G. Li, et al. Interface engineering of highly efficient perovskite solar cells. *Science* **345** (2014), 542–546.

[6] NREL. *Best Research-Cell Efficiencies: Rev. October 2023*. 2023.

[7] S. D. Stranks, G. E. Eperon, G. Grancini, et al. Electron-hole diffusion lengths exceeding 1 micrometer in an organometal trihalide perovskite absorber. *Science* **342** (2013), 341–344.

[8] D. Shi, V. Adinolfi, R. Comin, et al. Low trap-state density and long carrier diffusion in organolead trihalide perovskite single crystals. *Science* **347** (2015), 519–522.

[9] H. Wei, Y. Fang, P. Mulligan, et al. Sensitive X-ray detectors made of methylammonium lead tribromide perovskite single crystals. *Nature Photonics* **10** (2016), 333–339.

[10] H. Cho, S.-H. Jeong, M.-H. Park, et al. Overcoming the electroluminescence efficiency limitations of perovskite light-emitting diodes. *Science* **350** (2015), 1222–1225.

[11] C. Gu and J.-S. Lee. Flexible hybrid organic–inorganic perovskite memory. *ACS nano* **10** (2016), 5413–5418.

[12] M. Liu, M. B. Johnston, and H. J. Snaith. Efficient Planar Heterojunction Perovskite Solar Cells by Vapour Deposition. *Nature* **501** (2013), 395–398.

[13] L. Gil-Escrig, C. Dreessen, F. Palazon, et al. Efficient Wide-Bandgap Mixed-Cation and Mixed-Halide Perovskite Solar Cells by Vacuum Deposition. *ACS Energy Letters* **6** (2021), 827–836.

[14] N. Klipfel, C. Momblona, H. Kanda, et al. Crystallographically Oriented Hybrid Perovskites via Thermal Vacuum Codeposition. *Solar RRL* **5** (2021), 2100191.

[15] E. M. Hutter, R. J. Sutton, S. Chandrashekar, et al. Vapour-Deposited Cesium Lead Iodide Perovskites: Microsecond Charge Carrier Lifetimes and Enhanced Photovoltaic Performance. *ACS Energy Letters* **2** (2017), 1901–1908.

[16] Y. Vaynzof. The Future of Perovskite Photovoltaics—Thermal Evaporation or Solution Processing? *Advanced Energy Materials* **10** (2020), 2003073.

[17] J. Li, H. A. Dewi, H. Wang, et al. Co-Evaporated MAPbI3 with Graded Fermi Levels Enables Highly Performing , Scalable , and Flexible p-i-n Perovskite Solar Cells. *Adv. Funct. Mater.* **2103252** (2021).

[18] J. Werner, F. Sahli, F. Fu, et al. Perovskite/Perovskite/Silicon Monolithic Triple-Junction Solar Cells with a Fully Textured Design. *ACS Energy Letters* **3** (2018), 2052–2058.

[19] J. Li, H. Wang, X. Y. Chin, et al. Highly Efficient Thermally Co-evaporated Perovskite Solar Cells and Mini-modules. *Joule* **4** (2020), 1035–1053.

[20] M. Roß, L. Gil-Escrig, A. Al-Ashouri, et al. Co-Evaporated p-i-n Perovskite Solar Cells beyond 20% Efficiency: Impact of Substrate Temperature and Hole-Transport Layer. *ACS Applied Materials and Interfaces* **12** (2020), 39261–39272.

[21] H. A. Dewi, J. Li, H. Wang, et al. Excellent Intrinsic Long-Term Thermal Stability of Co-Evaporated MAPbI3 Solar Cells at 85 °C. *Advanced Functional Materials* **31** (2021), 1–9.

[22] E. Erdenebileg, H. Wang, J. Li, et al. Low-Temperature Atomic Layer Deposited Electron Transport Layers for Co-Evaporated Perovskite Solar Cells. *Solar RRL* **6** (2022), 2100842.

[23] J. Li, H. A. Dewi, H. Wang, et al. Design of Perovskite Thermally Co-Evaporated Highly Efficient Mini-Modules with High Geometrical Fill Factors. *Solar RRL* **4** (2020), 2000473.

[24] J. Li, H. Wang, H. A. Dewi, et al. Potassium acetate-based treatment for thermally co-evaporated perovskite solar cells. *Coatings* **10** (2020), 1163.

[25] F. Palazon, D. Pérez-del-Rey, B. Dänekamp, et al. Room-Temperature Cubic Phase Crystallization and High Stability of Vacuum-Deposited Methylammonium Lead Triiodide Thin Films for High-Efficiency Solar Cells. *Advanced Materials* **31** (2019), 1902692.

[26] M. Klein, J. Li, A. Bruno, and C. Soci. Co-Evaporated Perovskite Light-Emitting Transistor Operating at Room Temperature. *Advanced Electronic Materials* **7** (2021), 1–8.

[27] F. Maddalena, X. Y. Chin, D. Cortecchia, A. Bruno, and C. Soci. Brightness Enhancement in Pulsed-Operated Perovskite Light-Emitting Transistors. *ACS Applied Materials and Interfaces* **10** (2018), 37316–37325.

[28] T. Abzieher, T. Feeney, F. Schackmar, et al. From Groundwork to Efficient Solar Cells: On the Importance of the Substrate Material in Co-Evaporated Perovskite Solar Cells. *Advanced Functional Materials* (2021), 2104482.

[29] J. Emara, T. Schnier, N. Pourdavoud, et al. Impact of Film Stoichiometry on the Ionization Energy and Electronic Structure of CH3NH3PbI3 Perovskites. *Advanced Materials* **28** (2016), 553–559.

[30] E. M. Hutter, G. E. Eperon, S. D. Stranks, and T. J. Savenije. Charge Carriers in Planar and Meso-Structured Organic-Inorganic Perovskites: Mobilities, Lifetimes, and Concentrations of Trap States. *Journal of Physical Chemistry Letters* **6** (2015), 3082–3090.

[31] E. M. Hutter, G. E. Eperon, S. D. Stranks, and T. J. Savenije. Charge Carriers in Planar and Meso-Structured Organic-Inorganic Perovskites: Mobilities, Lifetimes, and Concentrations of Trap States. *Journal of Physical Chemistry Letters* **6** (2015), 3082–3090.

[32] T. Li, S. Wang, J. Yang, et al. Multiple functional groups synergistically improve the performance of inverted planar perovskite solar cells. *Nano Energy* **82** (2021), 105742.

[33] A. Poglitsch and D. Weber. Dynamic disorder in methylammoniumtrihalogenoplumbates (II) observed by millimeter-wave spectroscopy. *The Journal of Chemical Physics* **87** (1987), 6373–6378.

[34] T. J. Jacobsson, L. J. Schwan, M. Ottosson, A. Hagfeldt, and T. Edvinsson. Determination of Thermal Expansion Coefficients and Locating the Temperature-Induced Phase Transition in Methylammonium Lead Perovskites Using X-ray Diffraction. *Inorganic Chemistry* **54** (2015), 10678–10685.

[35] A. Osherov, E. M. Hutter, K. Galkowski, et al. The Impact of Phase Retention on the Structural and Optoelectronic Properties of Metal Halide Perovskites. *Advanced Materials* **28** (2016), 10757–10763.

[36] Q. Wang, Y. Shao, H. Xie, et al. Qualifying composition dependent p and n self-doping in CH3NH3PbI3. *Applied Physics Letters* **105** (2014), 163508.

[37] B. Dänekamp, C. Müller, M. Sendner, et al. Perovskite-Perovskite Homojunctions via Compositional Doping. *Journal of Physical Chemistry Letters* **9** (2018), 2770–2775.

[38] P. Cui, D. Wei, J. Ji, et al. Planar p–n homojunction perovskite solar cells with efficiency exceeding 21.3%. *Nature Energy* **4** (2019), 150–159.

[39] P. Fassl, Y. Zakharko, L. M. Falk, et al. Effect of density of surface defects on photoluminescence properties in MAPbI3 perovskite films. *Journal of Materials Chemistry C* **7** (2019), 5285–5292.

[40] J. Euvrard, Y. Yan, and D. B. Mitzi. Electrical doping in halide perovskites. *Nature Reviews Materials* **6** (2021), 531–549.

[41] Y. Lin, T. Li, Y. Liu, et al. Perovskite solar cells with embedded homojunction via nonuniform metal ion doping. *Cell Reports Physical Science* **2** (2021), 100415.

[42] A. Miyata, A. Mitioglu, P. Plochocka, et al. Direct measurement of the exciton binding energy and effective masses for charge carriers in organic-inorganic tri-halide perovskites. *Nature Physics* **11** (2015), 582–587.

[43] O. G. Reid, M. Yang, N. Kopidakis, K. Zhu, and G. Rumbles. Grain-Size-Limited Mobility in Methylammonium Lead Iodide Perovskite Thin Films. *ACS Energy Letters* **1** (2016), 561–565.

Appendices

3.A. Appendices

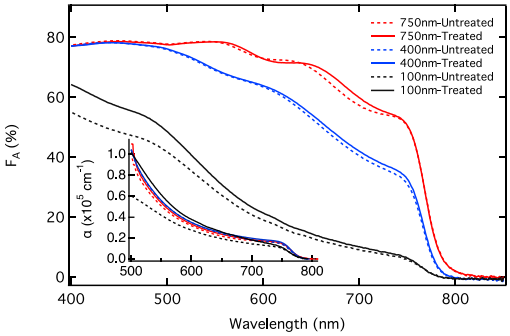

Figure 3A.1: Optical attenuation spectra and corresponding absorption coefficient spectra (inset) of $MAPbI_3$ films with different thicknesses.

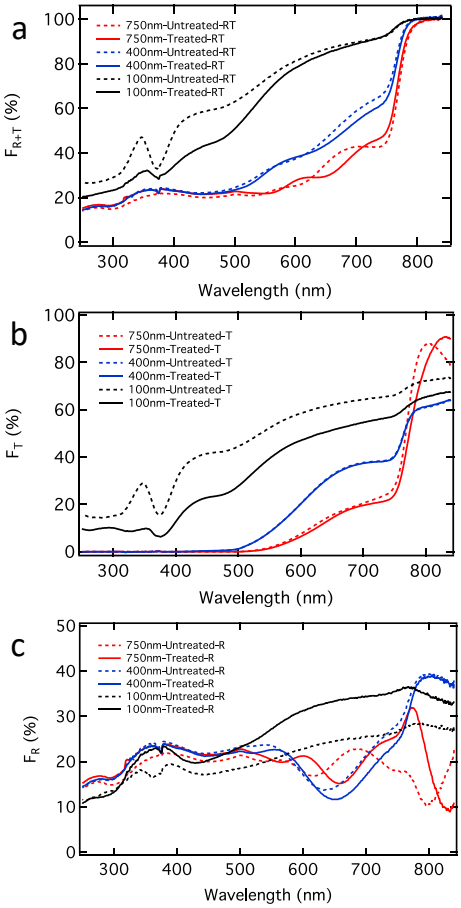

Figure 3A.2: Fraction of light reflected and transmitted (a), transmitted (b), and reflected (c) by /ceMAPbI3 films with different thicknesses and without/with treatment.

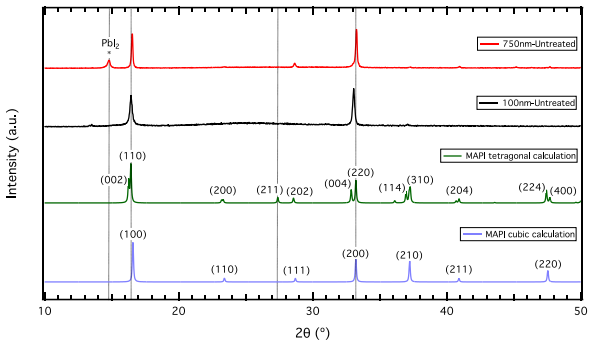

Figure 3A.3: Normalised X-ray Diffraction (XRD) patterns (Co Kα X-radiation) of evaporated $MAPbI_3$ films of 100 and 750 nm. The two lower patterns are the simulations of $MAPbI_3$ tetragonal and cubic phases.[1]

[1] C. C. Stoumpos, et al. Semiconducting tin and lead iodide perovskites with organic cations: phase transitions, high mobilities, and near-Infrared photoluminescent properties. *Inorganic Chemistry* **15** (2013), 9019–9038.

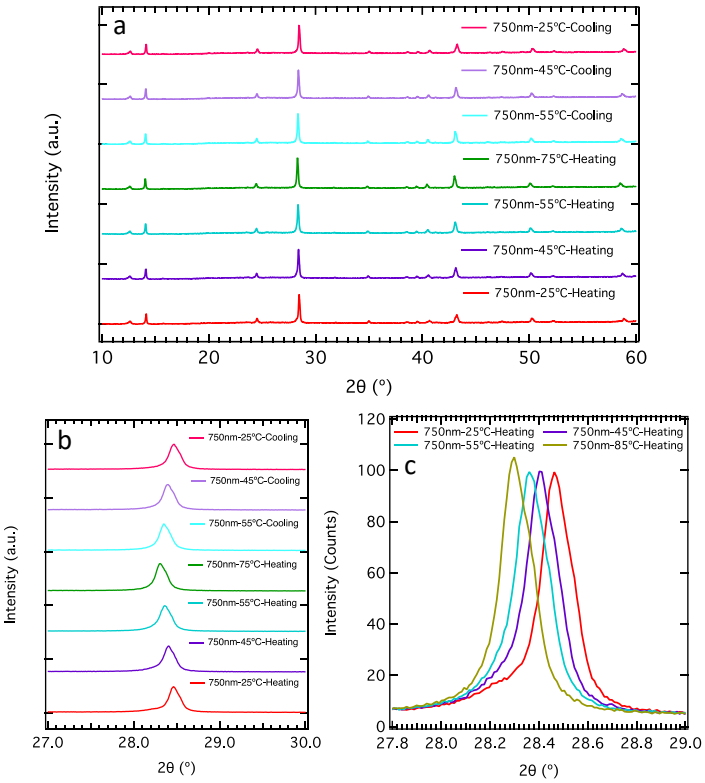

Figure 3A.4: XRD patterns (Cu Kα X-radiation) of 750 nm treated (a, b, c) $MAPbI_3$ films at different temperatures under vacuum. Panel (a) displays the full pattern and panels (b and c) a selection of the XRD patterns around 28 degrees.

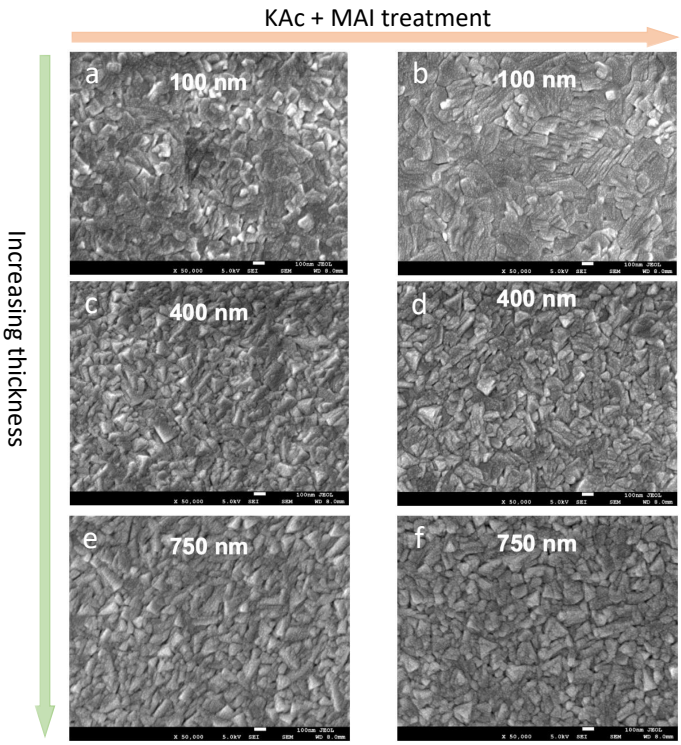

Figure 3A.5: Scanning Electron Microscope (SEM) top-view images for (a) 100, (c) 400, (e) 750 nm untreated (left panels), and (b) 100, (d) 400, (f) 750 nm treated (right panels) evaporated $MAPbI_3$ films.

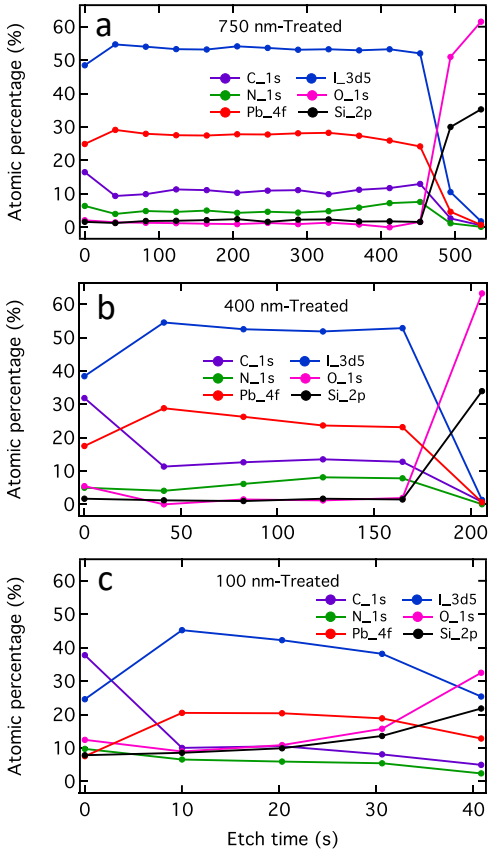

Figure 3A.6: The atomic percentage ratio of I, Pb, C, N, O, and Si as a function of etching time for 750 (a), 400 (b), and 100 nm (c) treated $MAPbI_3$ films, respectively.

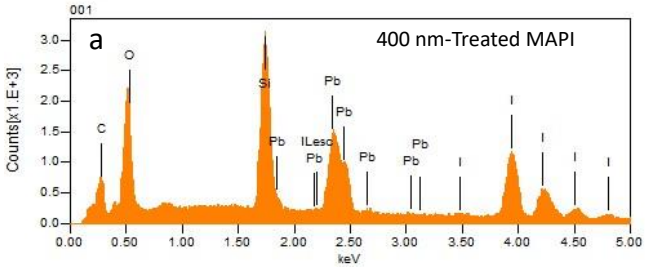

Figure 3A.7: Electron dispersive spectroscopy (EDS) spectra of all elements involved and corresponding quantitative tables of 400 (a) and 750 nm (b) treated $MAPbI_3$ films deposited on the quartz substrate. The atomic ratios of I/Pb in 400 and 750 nm $MAPbI_3$ films are close to 2.8 and 2.5, respectively. Given the limitation of EDS, 100 nm $MAPbI_3$ film is too thin to be measured.

Table 3A.1: SEM-EDS analysis of 400 nm treated $MAPbI_3$.

Chemical formula	Mass [%]	Atom [%]	Sigma	Net	K ratio	Line
C	4.47	22.51	0.01	13247	0.0106264	K
O	5.55	10.97	0.03	40885	0.0964698	K
Si	11.35	24.42	0.07	105824	0.2901857	K
I	49.73	23.68	0.27	98947	1.0927178	L
Pb	28.89	8.42	0.22	90360	0.4931808	M
Total	100	100	-	-	-	-

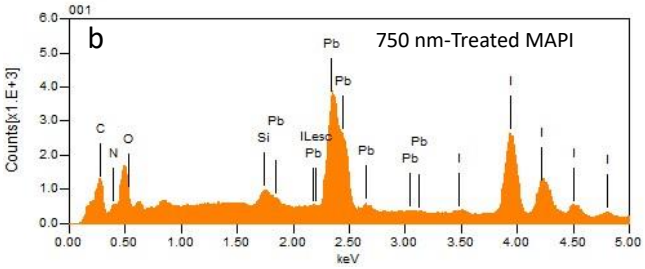

Figure 3A.8: Electron dispersive spectroscopy (EDS) spectra of all elements involved and corresponding quantitative tables of 400 (a) and 750 nm (b) treated $MAPbI_3$ films deposited on the quartz substrate. The atomic ratios of I/Pb in 400 and 750 nm $MAPbI_3$ films are close to 2.8 and 2.5, respectively. Given the limitation of EDS, 100 nm $MAPbI_3$ film is too thin to be measured.

Table 3A.2: SEM-EDS analysis of 750 nm treated $MAPbI_3$.

Chemical formula	Mass [%]	Atom [%]	Sigma	Net	K ratio	Line
C	3.11	27.19	0.01	21379	0.0171502	K
N*	0.16	1.22	0.02	683	0.0043408	K
O*	0.22	1.43	0.01	3218	0.0075927	K
Si	0.81	3.04	0.03	14241	0.0390502	K
I	57.80	47.89	0.21	221784	2.4492583	L
Pb	37.90	19.24	0.18	232288	1.2678120	M
Total	100	100	-	-	-	-

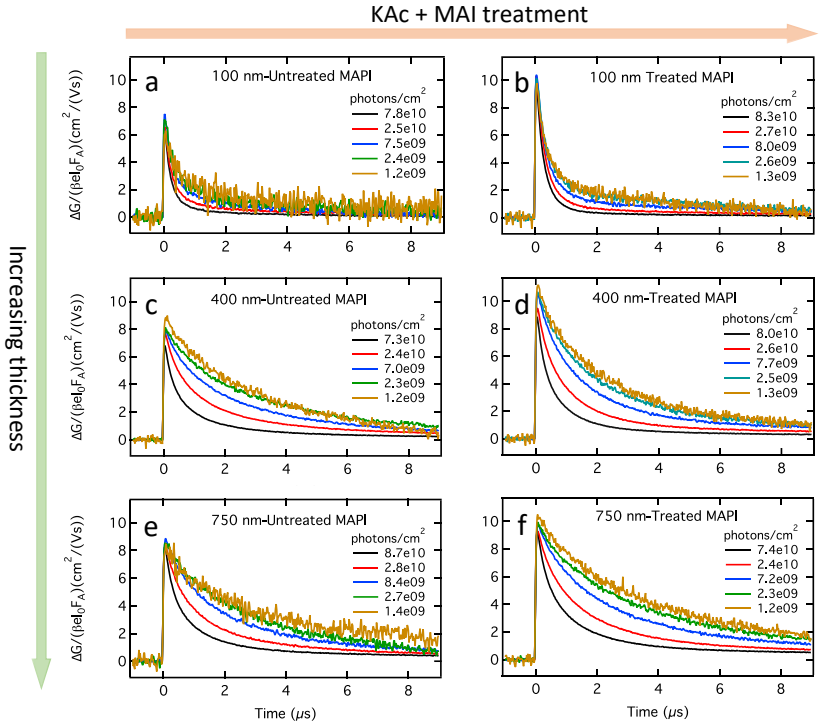

Figure 3A.9: Time-resolved microwave conductivity (TRMC) traces for (a, b) 100, (c, d) 400, and (e, f) 750 nm untreated (left panels) and treated (right panels) recorded on excitation at 500 nm with the incident light intensities ranging from 10^9 to 10^{10} photons cm^{-2} per pulse and normalized for the amount absorbed photons.

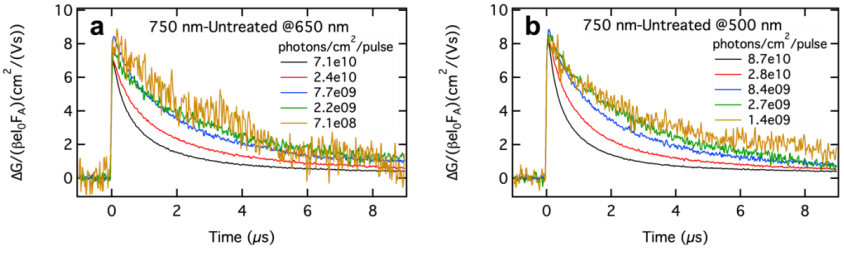

Figure 3A.10: Comparison of TRMC traces for 750 nm untreated films recorded on excitation at (a) 500 and (b) 650 nm with light intensities ranging from 10^9 to 10^{10} photons cm^{-2} per pulse and normalized for the amount absorbed photons.

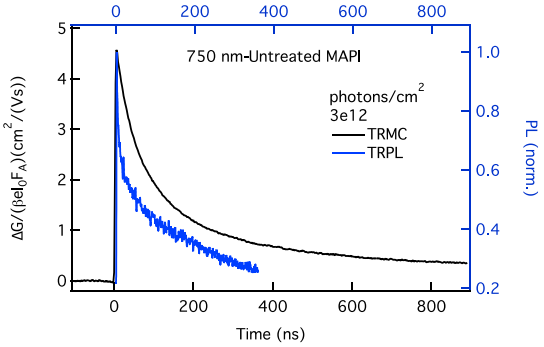

Figure 3A.11: Comparison of TRMC and TRPL signals. The TRMC trace is recorded using an excitation wavelength of 500 nm, while the sample is excited at 405 nm for the TRPL. The incident number of photons is around 10^{12} photons cm^{-2} per pulse for both methods.

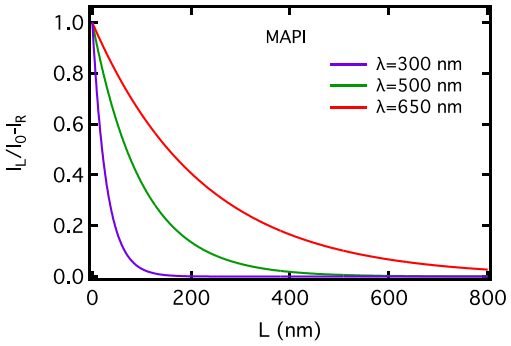

Figure 3A.12: Initial charge carrier generation profile for $MAPbI_3$ at an excitation wavelength of 300 and 500 nm.

4

Temperature-dependent Structure and Carrier Dynamics in CsMAFA-based Perovskites

State-of-the-art triple cation, mixed halide perovskites are extensively studied in perovskite solar cells, showing very promising performance and stability. In this Chapter, an in-depth fundamental understanding of how the phase behavior in $Cs_{0.05}FA_{0.85}MA_{0.10}Pb(I_{0.97}Br_{0.03})_3$ (CsMAFA) affects the optoelectronic properties is studied. Analysis of temperature-dependent XRD measurements on CsMAFA shows phase transitions at around 280 and 180 K and a gradual change of tensile to compressive microstrain. From additional photoconductivity measurements, the lowest concentration of traps corresponds to the smallest amount of microstrain in the β-phase at around 240 K.

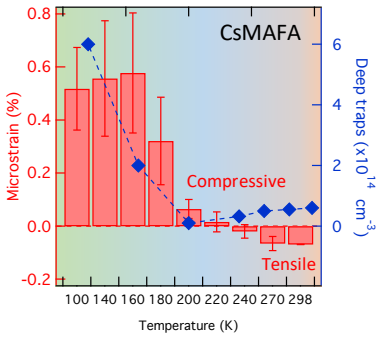

This chapter is based on

J. Zhao, X. Liu, Z. Wu, et al. Temperature-dependent Interplay between Structural and Charge Carrier Dynamics in CsMAFA-based Perovskites. *Advanced Functional Materials* (2023), 2311727.

4.1. Introduction

Over the last decade metal halide perovskites (MHPs) have attracted a tremendous amount of attention owing to their favorable intrinsic optoelectronic properties, such as high absorption coefficients (~ 10^5 cm^{-1}), fairly balanced effective carrier mobilities (tens of $cm^2(Vs)^{-1}$), remarkable defect tolerance ($10^{13} - 10^{16} cm^{-3}$), as well as ease of fabrication, etc.[1–5] Hence, a variety of applications ranging from thin-film photovoltaics (PV) to light-emitting devices have been developed.[5–7] Recently, the rapid progress in the development of single-junction perovskite solar cells (PSCs) achieved a certified power conversion efficiency (PCE) of 26.1%.[8] These high PCEs are generally found in FA-rich MHPs combined with a small amount of Cs and/or MA.[9–16] Previous work has shown that the improved phase stability of FA-rich MHPs is achieved by manipulating the Goldschmidt tolerance factor by mixing MA, Cs, and Br.[17]

Beyond terrestrial applications, PSCs are promising candidates for space applications due to their unique features such as their superior radiation resistance.[18] Recent work on complete solar cells at low temperatures[19,20] has shown that the performance of CsMAFA-based PSCs increased by 8% at 220 K in comparison to room temperature due to the improved open-circuit voltage, which was linked to the elimination of intrinsic defects present at that temperature.[19] Another study on the temperature-dependent performance of a $(Cs_{0.05}FA_{0.79}MA_{0.16}Pb(I_{0.83}Br_{0.17})_3)$ device revealed that inhibition of carrier extraction across interfaces leads to severe performance losses at $T < 200$ K.[20] Despite these insights, there is little knowledge of how the optoelectronic properties of FA-rich MHPs are affected by temperature. Therefore, it is of great interest to investigate the fundamental optoelectronic properties of these intrinsic absorber layers with temperature in an effort to explain the superior properties of this class of materials and eventually to come to compositions with even improved potentials.

In general, cooling MHPs in the range between 300-100 K is accompanied by one or more structural phase transitions.[21] The change of the crystal structure largely influences the photoluminescence (PL) and charge carrier recombination processes in $(FAPbI_3)_{0.85}(MAPbBr_3)_{0.15}$ layers.[22] However, the underlying relationship between their structural and optoelectronic properties is not fully understood and there are still several open questions to be further resolved. For instance, how does temperature-induced lattice microstrain play a role in the formation of defect states and how do these defects affect the charge carrier recombination dynamics? Furthermore, shallow defects are generally considered to be not detrimental to the PCE since they are close to the edges of the bands.[23] It is unclear how these shallow defects affect the dynamics upon cooling. Besides, there is typically a mismatch in thermal expansion coefficients between the MHP layer and substrate affecting the phase behavior and optoelectronic properties. In addition, excess PbI_2 has been widely used in MHPs as a passivation strategy to improve the performance of PSCs, and its impact on the structure and recombination kinetics as well as stability has also been extensively investigated.[24–29] However, systematic studies on the role of excess PbI_2 on the low-temperature structural and optoelectronic properties of FA-rich MHPs are still missing. For these reasons it is important to investigate how the temperature affects the structure and consecutively the optoelectronic properties and stability in CsMAFA-based MHPs.

In this Chapter, we studied the relationship between structural and optoelectronic

properties of CsMAFA layers as a function of temperature by means of XRD, absorption, and PL, as well as contactless photoconductivity measurements. This Chapter starts with the temperature-dependent XRD analysis of CsMAFA with a small excess of PbI_2. The XRD patterns are all refined revealing an $\alpha - \beta$ phase transition between 298 and 270 K and a further phase transition to the γ-phase at around 180 K. We continue with optical measurements, which show that the band gap monotonically reduces without discontinuities from 298 K to 100 K. Then time-resolved microwave photoconductivity measurements over the same temperature range are carried out using a short laser pulse at an excitation wavelength of 600 nm. By recording multiple traces with various intensities at each temperature, the effect of the intensity on the decay kinetics is studied in detail. These traces are fitted using a kinetic model including shallow and deep states in the band structure.

From the fits, we conclude that first, upon cooling, the mobility is enhanced in the β-phase due to reduced phonon scattering. Upon further cooling, the mobility decreases again in the γ-phase because of a substantial increase in deep traps, rather than a change in the effective mass of electrons and holes, as shown by density functional theory calculations. Furthermore, shallow states affect the charge carrier dynamics negatively due to the reduced thermal energy upon cooling. Moreover, on entering the γ-phase, the deep trap density increases at least one order of magnitude compared with the density at 200 K. This is most likely related to the increase in microstrain in the γ-phase. Finally, we find that excess PbI_2 inhibits phase retention in CsMAFA layers by reducing the mismatch of the thermal expansion coefficient between the quartz and perovskite. Most importantly, CsMAFA exhibits the lowest deep trap density at 200 K in the β-phase, consistent with the highest PCE in FA-rich based PSC at 220 K.[19] This is in line with the fairly balanced electron and hole charge carrier diffusion lengths, which we calculated using the kinetic constants found at 200 K.

4.2. Results and discussion

$Cs_{0.05}MA_{0.10}FA_{0.85}Pb(I_{0.97}Br_{0.03})_3$ (CsMAFA) layers (of about 500 nm thickness) were deposited on quartz substrates by spin-coating followed by the introduction of the antisolvent to accelerate the nucleation and growth of the perovskite layer.[30,31] A 5% excess PbI_2 was used in the precursor solution to improve the structural properties (see Experimental Methods for more detailed information). In Figure 4A.1a in Appendices the optical attenuation spectrum of CsMAFA is provided, showing optical absorption onset at around 800 nm (1.55 eV) in line with the literature.[32,33] Figure 4A.1b in Appendices presents the XRD pattern confirming that the layer indeed shows excess PbI_2 by the diffraction peaks located at $2\theta = 12.7°, 25.4°$, and $38.1°$. Figure 4A.1c in Appendices shows the top view SEM image of CsMAFA displaying the compact and polycrystalline nature of the perovskites.

In order to identify where the excess PbI_2 is located in the CsMAFA sample, we carried out grazing-incidence XRD (GIXRD) measurements with incident angles ranging from $\omega = 0.2°$ to $5°$, as shown in Figure 4.1a. Using this approach, we are able to investigate the nature of the layer at various depths, since the larger the incident angle, the deeper the layer is probed. The ratios of the PbI_2 peak at $2\theta = 12.7°$ and the perovskite (100) peak at $2\theta = 14°$ are collected in Table 4A.1 in Appendices for the different incident angles.

Initially, the ratio reduces with increasing the angle from $\omega = 0.2°$ to 1°, which may be partly caused by the strong preferred orientation of the PbI_2. Since only the (002) peak of PbI_2 is observed (Figure 4A.1b in Appendices) and the fact that changing the incident angle changes the direction of the Q-vector/probed lattice vector, a decrease of the PbI_2 reflection at $2\theta = 12.7°$ with increasing ω is also expected. Most importantly, the ratio increases significantly from 3° to 5° implying that the excess PbI_2 is most likely residing at the bottom part of the layer instead of the bulk.

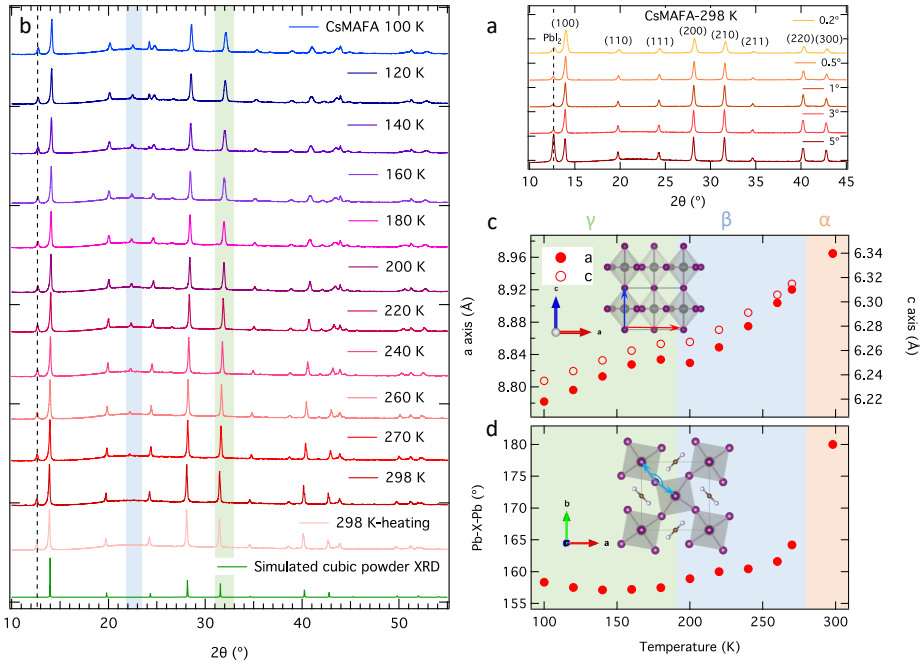

Figure 4.1: (a) Normalized grazing-incidence XRD patterns with incident angles ranging from 0.2° to 5° for the CsMAFA layer at 298 K. (b) Temperature dependence of an overview of the Bragg-Brentano XRD patterns (Cu Kα X-radiation) of the CsMAFA layer deposited on quartz, (c) Lattice parameters a (left axis, indicated by the red arrow) and c (right axis, indicated by the blue arrow), (d) Pb-X-Pb bond angles (indicated by light blue arrows) extracted from the refinement of XRD as a function of temperature.

To study how the structure of the CsMAFA layer changes with temperature, X-ray diffraction (XRD) was performed between 298 K and 100 K. Figure 4.1b shows an overview of the XRD patterns with the peak at 12.7°, indicated by the vertical dashed line, confirming the presence of excess PbI_2 in the CsMAFA sample. All peaks at 298 K correspond to the cubic (α)-phase of the perovskite indicated by the pattern at the bottom of Figure 4.1b (See also Figure 4.1a for corresponding planes).[34,35] At 270 K, a new peak at 22.2° starts to appear and becomes more pronounced on cooling, marked by the blue shade. This is attributed to the phase transition from the α- to the tetragonal (β)-phase between 298 and 270 K, consistent with the $\alpha-\beta$ phase transition at 285 K reported in pure $FAPbI_3$.[36] Furthermore, at 180 K, an obvious peak broadening at ~ 32° and 41°

is observed (green shade), implying a second phase transition to a tetragonal γ-phase (retaining *P4/mbm*, no.127) in agreement with the $\beta-\gamma$ phase transition reported for $FAPbI_3$.[35,36] It is worth noting here that the phase transition temperature can be slightly shifted for the FA-rich mixed cation and mixed halide perovskites in comparison to pure $FAPbI_3$.[37] On lowering the temperature down to 140 K, additional peak splitting leads to a narrow and broad peak at ~ 24°, indicative of a small amount of additional phase consistent with the (111) peak of the α-phase. Importantly, when the layer is heated up to 298 K, a fully reversible conversion to the original cubic phase is observed and no phase segregation occurs.

To better understand and quantify how the crystal structure varies, we refined the XRD patterns at each temperature and were able to extract the unit cell parameters as well as the corresponding Pb-X-Pb bond angle using the space group *P4/mbm* no.127 (See Figure 4A.2 in Appendices for the refinement of XRD). We should note here that the refinement of thin film-based XRD data is somewhat limited as compared to the refinement of XRD data recorded on powders. Nevertheless, since we intend to link the optical and conductivity properties to the structure in the thin film, we focused in this Chapter on layers and did not measure any powder samples. In addition, due to the polycrystalline nature and weak preferential orientation of the CsMAFA layer, the XRD patterns show for example at room temperature all diffraction peaks expected for cubic powder XRD as shown at the bottom of Figure 4.1b, making the refinement still feasible and reliable.

Figures 4.1c and 4.1d show the lattice parameters a,c and the Pb-X-Pb bond angle in the ab plane, respectively, as a function of temperature (see Figure 4A.3 in Appendices for the evolution of the ratio $a/\sqrt{2}c$ with temperature). In Figure 4.1c, the sizes of the a- and c-axes continuously decrease due to lattice contraction upon cooling.[36,38] At ~ 180 K, an inflection point in both directions corresponds to the phase transition from the β- to γ-phase.[22,35,36] The discontinuity at ~ 180 K in the a-direction is slightly larger compared to the c-direction, indicating that the titling of PbI_6 octahedra is more severe in the ab plane than the distortion along the c-direction. Figure 4.1d shows that the Pb-X-Pb bond angle abruptly reduces from 180° to 165° corresponding from the α- to the β-phase,[35] implying that the crystal structure is more distorted in the ab plane than in the c-direction in the β-phase. In addition, the unit cell volume vs. temperature is given in Figure 4A.4 in Appendices. The volumetric thermal expansion coefficients, α_v, in the β- and γ-phases are $422 \pm 20 \times 10^{-6}$ K^{-1} and $204 \pm 15 \times 10^{-6}$ K^{-1}, respectively, which are in agreement with previously reported values for $FAPbI_3$.[35]

Distortion of the ideal crystal structure, by either expansion or contraction of the unit cell, leads to an increase of the lattice strain in perovskites. A common lattice strain in polycrystalline films is microstrain (ε), which can be evaluated by peak broadening. The relationship between the peak width (β) and microstrain can be represented by the Williamson-Hall plot (W-H plot) method (See Note S1 in more detail).[39,40] To quantitatively reveal how temperature affects the microstrain in the CsMAFA layer, we analyzed the microstrain evolution during cooling using the W-H plot. Figure 4.2a shows the plot of $\beta\cos\theta$ as a function of $\sin\theta$, from which the microstrain can be deduced from the slope. It is worth noting that a negative slope indicates a tensile strain, while a positive slope originates from a compressive strain. Interestingly, a small tensile strain is

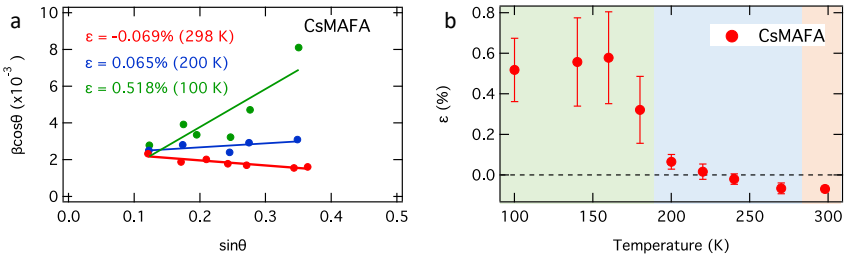

Figure 4.2: (a) Williamson-Hall plot of the CsMAFA layer at three phases. (b) Evolution of microstrain (ε) with the temperature ranging from 298 to 100 K.

observed in the CsMAFA layer at 298 K. It is most likely due to the cooling process after annealing during the fabrication of the CsMAFA layers. In Figure 4.2b, as temperature decreases, the tensile strain reduces to 0 and eventually becomes compressive, reaching maximum values in the γ-phase. Therefore, the smallest microstrain is observed at around 220 K. Moreover, we should note that the fit becomes worse below 200 K, as shown by the large error bars in Figure 4.2b. These relatively large errors in the γ-phase indicate the presence of anisotropic microstrain.

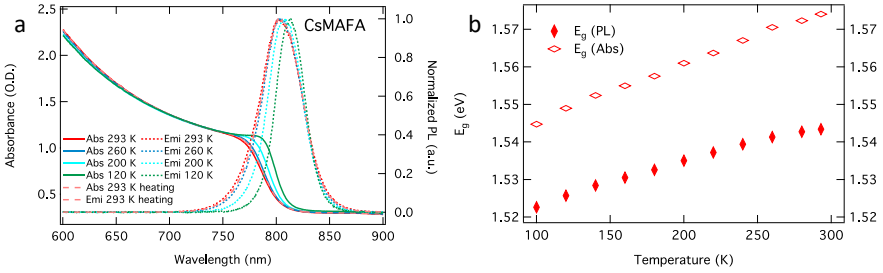

Figure 4.3: (a) Temperature dependence of the absorption (solid line, left axis) and normalized photoluminescence spectra (dotted line, right axis) of the CsMAFA layer excited with violet LED light (λ = 405 nm). Dashed lines indicate the data recorded upon heating. (b) Evolution of bandgap energy (E_g) extracted from PL and absorption as a function of temperature for the CsMAFA layer.

Next, to gain more insight into the optical properties of CsMAFA, temperature-dependent absorption, and PL spectra were recorded in the range from 293 K to 100 K, as shown in Figure 4.3a. (See Figures 4A.5 and 4A.6 in Appendices for more temperatures). It can be observed that as temperature decreases, the onset of the absorption gradually shifts to higher wavelengths, corresponding to a similar redshift of the PL emission maximum. The absorption and PL spectra recorded upon heating overlap with the spectra recorded upon cooling, as given by the dashed lines, indicating that the evolution of the optical properties with temperature is fully reversible and changes in the spectra are not caused by the decomposition or degradation of the samples.

In Figure 4.3b, we plot the optical band gap (E_g Abs) and the maximum PL emission

(E_g PL) as a function of temperature. Based on the reported binding energies of FA-rich perovskites,[41–45] we expect that the contribution of excitons to the absorption and PL spectra is limited in the studied temperature range. This is substantiated by our calculations on the ratio between free charges and excitons using the Saha equation (See equation 2A.1 in Appendices). On decreasing the temperature, E_g monotonically reduces without discontinuities comparable to other FA-rich perovskites.[22,41] This implies that neither the tilting of the inorganic octahedra nor the rotational degree of freedom of the organic cation changes abruptly. Otherwise, these structural changes would lead to an abrupt energetic shift like in $MAPbI_3$ for the transition from the β- to γ-phase.[21,46] The continuous reduction in E_g upon cooling in CsMAFA is similar to that of other perovskites, in contrast to general semiconductors.[47,48] This is commonly attributed to the fact that as the lattice shrinks, the Pb-*s* and I-*s* orbitals overlap increases, leading to a rise of both the valence band maximum (VBM) and the conduction band minimum (CBM). Since the band edge shift of the VBM is larger than that of the CBM,[49,50] E_g becomes smaller as temperature decreases, as illustrated in Figure 4.6.

To investigate the optoelectronic properties of the CsMAFA layer upon cooling, we conducted temperature-dependent time-resolved microwave conductivity (TRMC) measurements from 298 K down to 120 K on pulsed excitation at λ = 600 nm. A photo and explanation describing the adapted microwave cell enabling it to vary temperature are provided in Figure 4A.13 in Appendices. Figures 4.4a-d show the photoconductance traces (ΔG) normalized by the number of absorbed photons as a function of time at 298, 260, 200, and 120 K. The initial increase of the signal originates from the generation of free charge carriers, while the decay is attributed to the immobilization of excess charge carriers via trapping or the recombination of electrons and holes. At low intensities, the decay kinetics are predominantly determined by non-radiative, first-order recombination mediated via deep trap states. With increasing laser pulse intensities, the decay kinetics become faster, which is due to enhanced second-order electron-hole recombination. This type of behavior has been observed and described previously for MHPs.[51–54]

The maximum signal height represents the product of the free charge carrier generation yield, φ, and the sum of the electron and hole mobility, $\sum\mu$. (See Equation 2.3 in the Experimental Methods in Chapter 2) Given the low exciton binding energy of 10-24 meV reported for FA-rich MHPs in different phases,[41–44,55] the majority of the excitons will dissociate into free charges, and the free charge carrier generation yield, φ, will be close to unity in both α- and β-phases (Figure 4A.7 in Appendices). Hence on comparing Figures 4.4a and 4.4b, corresponding to the conversion from the α- to the α-phase, the rise in signal size can be attributed to the increase of $\sum\mu$ in the β-phase.

On reducing the temperature to 120 K corresponding to the γ-phase, three important observations can be noticed: first, the maximum TRMC signal significantly reduces (Figure 4.4d). It is worth noting here that even at 120 K we can still assume that φ is close to unity considering the relatively low carrier densities (See calculations in Figure 4A.7 in Appendices using the Saha Equation 2A.1[55] in Appendices in Chapter 2. Most importantly, the carrier lifetimes become evidently longer with decay times extending up to hundreds of microseconds (Figure 4A.8 in Appendices). Finally, the charge carrier decay dynamics exhibit a completely different intensity dependence than in the α- and β-phases, with most of the TRMC traces overlapping at low incident light intensities.

These observations suggest a substantial increase in trap states. Note, that the charge carrier dynamics are fully reversible when the CsMAFA layer is heated up back to 298 K (Figure 4A.9 in Appendices), implying that all phenomena observed at low temperatures are related to the phase transitions and changes in thermal energy.

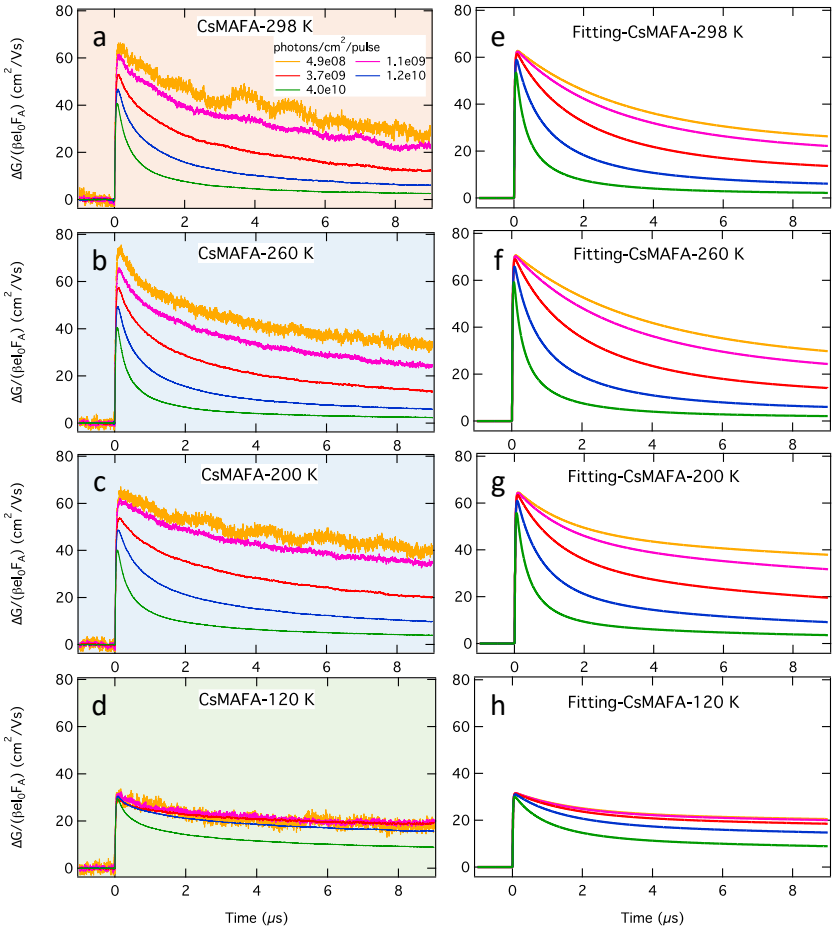

Figure 4.4: Experimental photoconductance traces (left panels) and corresponding fitting (right panels) for the CsMAFA sample at 298 K (a, e), 260 K (b, f), 200 K (c, g), and 120 K (d, h) recorded on excitation at 600 nm with incident light intensities ranging from 10^8 to 10^{10} photons cm^{-2} per pulse.

Basically, the mobility of electrons and holes is determined by their effective masses and scattering time. To understand the origin of the increase in $\sum\mu$, density functional theory (DFT) calculations were carried out to obtain the effective mass of electrons (m_e) and holes (m_h) at different phases. As input, we used the crystal structures and lattice parameters obtained from the refinement of the XRD patterns, as shown in Figure 4A.10 in Appendices (See Note S2 for detailed information). The calculation of me and m_h was

performed in two different directions/paths from Z to A and from Z to Γ in the Brillouin zone (Figure 4A.11 in Appendices). From Figure 4A.12 in Appendices it is clear that m_e and m_h remain fairly constant with small fluctuations across a temperature range from 298 to 100 K, regardless of the phases, in line with previous reports.[42] Hence, we can conclude that the enhancement of $\sum\mu$ in the β-phase is not due to the change in the effective mass of the electrons or holes. The increased mobility is most likely a result of the reduced phonon scattering with decreasing temperature, in good agreement with previous findings in FA-rich MHPs.[43] Moreover, we can also rule out that the reduction in the TRMC signal observed at 120 K is attributed to a change in the effective mass of both carriers. Instead, this reduction is most likely due to the substantial increase in deep and shallow traps. In addition, the calculation also demonstrates that m_e and m_h are fairly comparable, with a ratio close to 1:1 irrespective of the perovskite phases. Therefore, the lowering of the TRMC signal at 120 K is likely connected to the formation of a substantial increase in trap states for one of the carriers.

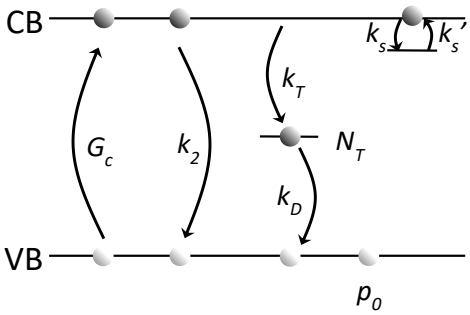

Figure 4.5: Kinetic model of charge carrier processes initiated by photoexcitation of CsMAFA. G_C represents the photo generation of charge carriers; k_2 depicts the second-order recombination rate. Electron trap-mediated recombination is described by a trapping rate, k_T, and a depopulation rate, k_D. The two small opposite arrows indicate the immobilization of electrons in shallow trap states with trapping rate k_s and thermal release rate k_s'.

To verify our above hypothesis, we modeled the photoconductance traces using an adapted kinetic model including shallow states (See Figure 4.5), previously successfully used to describe the photophysical processes in $(FA_{0.79}MA_{0.15}Cs_{0.06})Pb(I_{1-x}Br_x)_3$ (See Note S3 in Appendices for a used set of differential Equations 4A.4 to 4A.7).[52] The detailed global, iterative fitting procedure is summarized in Note S3 in Appendices. Important to note here is that a shallow state is defined as a state from which a charge can thermally escape back to the CB. In contrast, a deep electron defect only recombines with a corresponding hole in the VB. Since the optical absorption measurements indicate that the absorption coefficient does not vary a lot with temperature and the fact that the absorption and band-to-band recombination are basically coupled processes,[56] we tried to keep the second-order recombination constant during the fitting procedure.[57] Furthermore, we kept the ratio between electron and hole mobility constant at 1, since the ratio of me and m_h remains similar with temperature. The fits are shown in Figures 4.4e-h, matching the experimental traces well (See Figure 4A.14 in Appendices for

Table 4.1: Rate constants, trap densities, and mobilities extracted from the fits to TRMC traces of CsMAFA at different temperatures.

CsMAFA \ T [K]	298	280	260	240	200	160	120
k_2 [$\times 10^{-9}$ cm^{3}s^{-1}]	5.5	6	6	5	5	5	5
k_T [$\times 10^{-9}$ cm^{3}s^{-1}]	4	4	4	4	4	4	4
k_D [$\times 10^{-10}$ cm^{3}s^{-1}]	6	6	6	3	1	1	1
N_T [$\times 10^{14}$ cm^{-3}]	0.6	0.55	0.5	0.32	0.1	2	6
p_0 [$\times 10^{14}$ cm^{-3}]	0.6	0.55	0.5	0.32	0.1	10	10
k_s [$\times 10^{7}$ s^{-1}]	0	0	0	0.005	0.03	5.5	10
k'_s [$\times 10^{7}$ s^{-1}]	0	0	0	0.005	0.03	2	2.5
μ_e [cm^2(Vs)$^{-1}$]	32	34	36	35	33	35	27
μ_h [cm^2(Vs)$^{-1}$]	32	34	36	35	33	35	27

other temperatures in log-lin representations). All kinetic parameters are collected in Table 4.1. First of all, the $\sum\mu$ in the α-phase amounts to 64 cm^2(Vs)$^{-1}$ and increases to 72 cm^2(Vs)$^{-1}$ at 260 K in the β-phase. Although all other parameters remain fairly constant, the concentration of deep traps (N_T) reduces to 1×10^{13} cm^{-3} at 200 K. This seems to be consistent with the previously reported device efficiencies peaking at 220 K.[19] Moreover, below 240 K, shallow trap states start to play a role in the carrier recombination processes with comparable values between trapping (k_s) and de-trapping rate (k'_s). When entering the γ-phase, in addition to the shallow traps, the number of deep traps, N_T increases and is at least one order of magnitude higher than at 200 K. Furthermore, the ratio of k_s/k'_s increases to 4, implying that the electrons are most of the time residing in shallow states. These observations are all in line with the band diagram depicted in Figure 4.6 for the different phases of CsMAFA.

Knowing all these rate constants enables us to calculate the charge carrier diffusion lengths (Λ) for electrons and holes (see Figure 4.7a) at low carrier densities, where defect trapping plays an important role. These values are calculated by determining the half-lifetimes of electrons and holes and multiplying them by their respective mobility. Above 200 K we observe high values of Λ around 15 and 80 μm for electrons and holes, respectively. Below 200 K the Λ values for holes halve but for electrons, the reduction in Λ is more severe yielding values less than 1 μm. This large asymmetry in Λ could lead to space charge-limited current, heavily reducing the power conversion efficiency of the corresponding cell. Above 200 K, Λ values for electrons and holes are adequately high and relatively balanced with a small maximum at around 240 K. Apart from the diffusion length, the resulting concentrations of mobile electrons and holes generated under AM 1.5 steady-state illumination are important for the resulting Fermi level splitting, which determines the eventual voltage of a corresponding solar cell. In Figure 4.7b the resulting carrier concentrations are provided as a function of temperature. Since the Fermi level splitting is defined by:

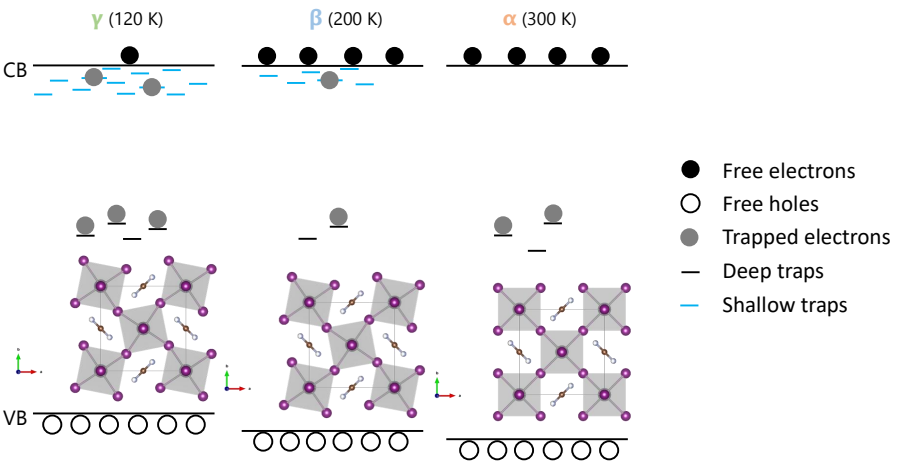

Figure 4.6: An illustration of the proposed energy band diagram at different phases. The crystal structures are visualized by VESTA[58] (see the inset of Figure 4.1c for a side view of the crystal structure).

$$\mu_{\mathrm{F}} = \frac{kT}{q} \ln \frac{(n_0 + \Delta n)\left(p_0 + \Delta p\right)}{n_{\mathrm{i}}^2} \tag{4.1}$$

where the kT is the thermal energy, q the elementary charge, n_{i} is the intrinsic carrier concentration, n_0 and p_0 are thermal-equilibrium concentrations of electrons and holes, and Δn and Δp are the concentrations of photogenerated excess electrons and holes, respectively. Since the product of excess electrons and holes ($\Delta n \Delta p$) remains more or less constant as a function of temperature we deduce that the voltage is not heavily affected by the defects formed in the γ-phase.

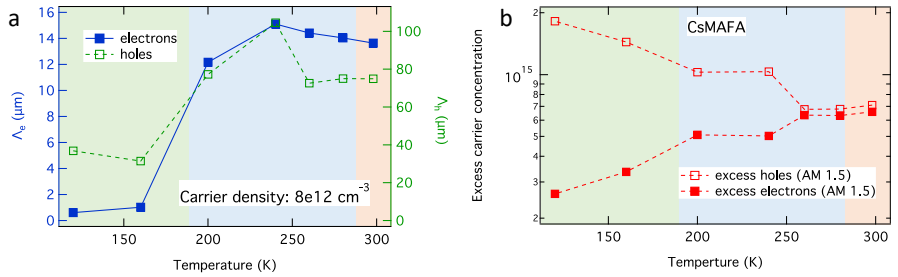

Figure 4.7: (a) Charge carrier diffusion length of electrons (left axis, blue) and holes (right axis, green) (b) Excess carrier concentration of holes (open squares) and electrons (closed squares) as a function of temperature for the CsMAFA layer.

To investigate how excess PbI_2 affects the structural and optoelectronic properties

in FA-rich MHPs, we prepared CsMAFA samples with a stoichiometric ratio, denoted as CsMAFA-st, and performed the same set of measurements, without the excess PbI_2. First, from the top view SEM images (Figures 4A.15a,b in Appendices), the average crystal domain size of CsMAFA (~ 200 nm) is almost twice as large as that of the CsMAFA-st (~ 100 nm), as demonstrated in the insets, in good agreement with XRD patterns showing that CsMAFA reveals narrower diffraction peaks in comparison to the CsMAFA-st (Figure 4A.15d). Secondly, XRD measurements as a function of temperature were performed, but we did not apply data refinement and microstrain calculations to CsMAFA-st, which will be discussed later on. To picture what happens in this layer, similar optical and TRMC measurements were carried out (See Figures 4A.17 and 4A.18 in Appendices). The absorption spectra for the two layers are comparable, but the PL intensity of CsMAFA is almost a factor of 2 higher as compared to that of CsMAFA-st at 298 K (Figure 4A.17b in Appendices). This can be explained by that defects at the grain boundaries are suppressed due to the increased crystal domain size in CsMAFA. Regarding the TRMC measurements at room temperature, the signal height for CsMAFA-st is almost a factor of 2 lower in comparison to the CsMAFA. We attribute this reduction to the lower effective mobility that is related to the smaller crystal domain size of CsMAFA-st,[59] confirmed by our SEM measurements (Figures 4A.15a,b in Appendices). Previously, similar effects on $MAPbI_3$ and other compositions with excess PbI_2 have been reported.[29,60–62]

Then, we investigated the photoconductivity of CsMAFA-st at various temperatures (Figure 4A.18 in Appendices). Most interestingly we observed on front side excitation at low temperatures an unusual, delayed signal rise on a μs timescale only for the CsMAFA-st (Figure 4A.18d in Appendices), while for the CsMAFA no delayed rise is visible. Such delayed growth implies that photogenerated carriers diffuse towards a region in which the carriers obtain higher mobility or the number of shallow traps is less. Therefore we expect that at low temperatures, the CsMAFA-st layer is non-homogeneous. To verify this asymmetric nature, we performed TRMC measurements using front and back-side excitation at 298 K (Figures 4.8a and 4.8b) and 130 K (Figures 4.8c and 4.8d) for both layers. (See Figure 4A.19 in Appendices for TRMC traces recorded at various intensities and Figure 4A.20 in Appendices for non-normalized TRMC traces of CsMAFA-st on front and back excitations at 298 and 130 K). At 298 K, the front- and back-side TRMC traces do not reveal appreciable differences in the charge carrier dynamics, indicating negligible differences in the top and bottom regions. i.e. the entire perovskite layer is homogeneous in the α-phase. The slight difference found using back illumination in comparison to the front side for the CsMAFA is most likely attributed to the presence of some PbI_2 at the bottom layer, as discussed in Figure 4.1a. In addition, in Figure 4A.20 in Appendices, a slight increase in signal height using back excitation is observed, which is due to the anti-reflection effect of the quartz substrate.

On comparing Figures 4.8c and 4.8d recorded at 130 K, the TRMC traces observed on the front and back side excitation of the CsMAFA-st layer are substantially different, while for the CsMAFA layer, they are much more comparable. Based on optical spectra (Figure 4A.5 in Appendices) and free carrier yield calculations (Figure 4A.7 in Appendices), excitons do not appear to play a role in CsMAFA-st at 130 K. Hence it is suggested that the CsMAFA-st layer is not completely converted to the γ-phase at 130 K. Given the more than 2 orders of magnitude difference in thermal expansion coefficient between

quartz ($\alpha_v = 0.54 \times 10^{-6}$ K^{-1}) and MHPs ($\alpha_v = 100 - 400 \times 10^{-6}$ K^{-1}),[35,63–65] some phase retention in the CsMAFA-st layer might occur as described previously for other MHPs.[66] This implies that on cooling to 130 K, the top part of the CsMAFA-st perovskite layer has converted to γ-phase, but the bottom part close to the quartz substrate is still in the β-phase (See Figure 4.8e). Hence on front excitation of CsMAFA-st, the generated carriers in the top part can diffuse from the γ-phase to the bottom region which is in the β-phase. Since the diffusion of electrons is in competition with the shallow trapping process in the γ-phase, the resulting rise in signal growth occurs very slowly i.e. within a few μs. However, after this period the excess carriers have obtained an on average higher mobility.

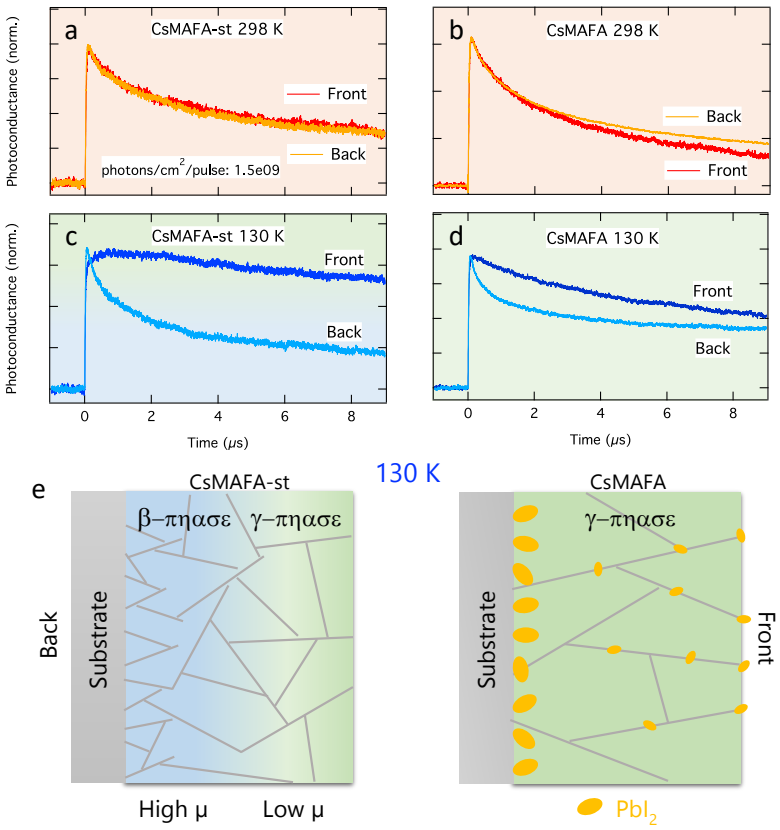

Figure 4.8: Normalized TRMC traces for (a, c) CsMAFA-st, (b, d) CsMAFA layers recorded at (a, b) 298 K and (c, d) 130 K on excitation at 600 nm for the front and back excitation at an incident intensity of around 2×10^9 photons cm^{-2} per pulse. (e) An illustration of the proposed structural phase transition at 130 K in the CsMAFA-st (left) and CsMAFA (right) layers deposited on the quartz substrate, respectively. The blue shade represents the β-phase, and the green shade is the γ-phase. The yellow dots are denoted as excess PbI_2. In addition, the grey lines indicate the crystal domain size from the cross-section view.

To further verify the asymmetric nature within the entire layer, we recorded the photoconductance traces using front-side excitation wavelengths of 650, 550, and 450 nm,

respectively (Figure 4A.21 in Appendices). Since the penetration depth at 450 nm is less than that at 650 nm, we are able to selectively excite the top part, meaning the initially generated free carriers are more distant from the β-phase. Figure 4A.21b in Appendices shows indeed that the shorter the excitation wavelengths, the slower the delayed signal of TRMC traces. Instead, the excitation-dependent TRMC traces at 298 K are nicely overlapping (Figure 4A.21a in Appendices). Furthermore, the normalized TRMC traces from back excitation nearly overlap, independent of excitation wavelength (Figure 4A.21c in Appendices). Combining these observations, we can rule out that excitons have a decisive influence on the TRMC decay. This indeed confirms our hypothesis that the delayed rise in TRMC signal in the CsMAFA-st layer originates from charge carriers diffusing from the top part residing in the γ-phase to the bottom part which is still in the β-phase. For the CsMAFA layer, showing no delayed rise and little difference between front and back excitation, the layer is completely converted into the γ-phase at 130 K. The absence of substantial phase retention is probably due to the presence of excess PbI_2 ($\alpha_v = 40 \times 10^{-6}$ K^{-1}) residing between the substrate and CsMAFA layer as concluded from the GIXRD measurement. We anticipate that the excess PbI_2 at the interface detaches the CsMAFA layer from the quartz. Moreover, the enlarged crystal domain size in CsMAFA may also facilitate the phase transition as some of the crystal domains go through the entire layer (See the cross-section SEM images in Figure 4A.22 in Appendices).

Now we get back to the original question of how temperature-induced structural changes affect the optoelectronic properties of the CsMAFA layer. As mentioned no abrupt changes in structural or optical properties are visible, which means that the phase transitions are gradual processes. As argued previously,[67] this might be due to the fact that for FA-rich MHPs the driving force for a phase transition is rather small. Effects of grain sizes or substrates can accelerate or retard the phase transition.[66,68]

Next, it is of interest to evaluate which type of defects are responsible for the observed charge carrier dynamics. (band structures for the different phases are provided in Figure 4.6). On lowering the temperature from 298 K to 200 K we find lower concentrations of deep defects. We speculate that this reduction in deep defects in the β-phase is likely linked to the drop in tensile microstrain since we observe the smallest microstrain at around 240 K. Furthermore, in the γ-phase we find that both the number of deep and shallow states increases substantially. Considering the latter, it has been reported that the FA_i interstitial and V_I vacancy form point defects close to the CBM in $FAPbI_3$ MHPs.[69–71] Hence we anticipate that although these point defects are harmless at 298 K as they are located above/close to the CBM, on cooling they become harmful since the thermal energy ($k_B T$) reduces or the energy difference between CBM and shallow defect level increases. This implies that in the γ-phase most of the time electrons are immobilized in the shallow states and the dominant contribution to the photoconductance is from the mobile holes, leading to the long tails in TRMC signals (Figure 4.4d).

Finally, from the TRMC measurements, we conclude that the concentration of deep defects also increases substantially in the γ-phase. However, at these low temperatures, spontaneous defect formation becomes less likely. Yet, from the analysis of the XRD patterns a steep rise in microstrain is observed, which might be related to the increased concentration of defects in the γ-phase. On cooling stacking faults or edge dislocations previously observed by atomic-resolution scanning transmission electron microscopy

(TEM)[72] might be formed in the γ-phase. Such types of defects can be expected to be fully reversible in line with the reversible structural and optoelectronic changes observed. Future research into cryogenic atomic-resolution scanning TEM may help to learn more about the nature of shallow and deep defects, combined with DFT calculations to gain insight into the corresponding defect levels.

To find out to what extent the observed optoelectronic properties of CsMAFA and CsMAFA-st are applicable to other FA-rich MHPs, we prepared CsMAFA lacking 5% of PbI_2 (CsMAFA-shortage) and CsMAFA treated with phenethylammonium iodide (CsMAFA+PEAI). Using temperature-dependent TRMC as shown in Figure 4A.23 in Appendices the charge carrier decay dynamics for CsMAFA+PEAI are very similar to those we observed in CsMAFA without post-treatment. More specifically at 110 K, most of the TRMC traces overlap at low incident light intensities implying that the concentration of deep defects is again relatively large in the γ-phase, which implies that indeed defects in the bulk are responsible for the observed behaviour. In contrast, the decay kinetics in CsMAFA-shortage exhibit a behavior close to that of the stoichiometric CsMAFA-st, with the delayed signal rise at 130 K. From the fact that there is no excess PbI_2 at the interface between quartz and CsMAFA-shortage (Figure 4A.24 in Appendices) we can expect phase retention near the quartz substrate leading to a non-homogeneous sample giving rise to the delayed ingrowth. Hence, we can conclude that the observed variations in optoelectronic properties coupled with the amount of PbI_2 are quite common in FA-rich MHPs. Moreover, for both types of samples, the effect of shallow states is according to our measurements at room temperature very limited, while the concentration of deep defects shows a minimum at around 200 K.

4.3. Conclusions

In this Chapter, the structural and optoelectronic properties of CsMAFA in different crystal phases were investigated by XRD, optical, and TRMC measurements. First, CsMAFA undergoes an $\alpha - \beta$ phase transition between 298 and 270 K and a further phase transition to the γ-phase at around 180 K. It is found the E_g monotonically reduces without discontinuities across the range of 298 and 100 K. Moreover, as temperature decreases, the effective carrier mobility is enhanced in the β-phase, which is attributed to a reduction of phonon scattering, since the effective masses of both carriers, as shown by DFT calculations, remain very comparable. From the photoconductance measurements, we conclude that CsMAFA exhibits the longest charge carrier diffusion lengths with the lowest deep trap densities close to 240 K, in line with the highest efficiency reported for CsMAFA-based devices at 220 K. Since the microstrain in CsMAFA amounts close to 0 at this temperature, we expect that this plays an essential role in the formation of deep defects in FA-rich perovskites.

On conversion from the β- to the γ-phase shallow defects close to the CB become detrimental to the charge carrier dynamics in MHPs. Although these point defects are harmless at 298 K as they are located above/close to the CBM, on cooling they become harmful since the thermal energy reduces or the energy difference between CBM and shallow defect level increases. Hence in the γ-phase most of the time electrons are immobilized in the shallow states. Apart from the shallow states the magnitude of deep traps in the γ-phase increases by an order of magnitude, which is most likely directly cor-

related with the enhancement in compressive microstrain. The presence of both shallow and deep defects leads to a huge unbalance between electron and hole diffusion lengths.

In contrast to CsMAFA containing a small excess of PbI_2, stoichiometric CsMAFA-st suffers from phase retention of the CsMAFA close to the substrate, which yields an inhomogeneous layer at 130 K comprising a γ-phase on top and a β-phase near the quartz surface. Carriers formed in the top slowly diffuse towards the bottom leading to a remarkable delayed rise in the photoconductance measurements. For the sample with excess PbI_2, it is expected that the PbI_2 residing at the interface detaches the CsMAFA from the quartz substrate leading to a homogeneous layer. Our work provides valuable insight into the temperature-dependent interplay between the structure and the charge carrier dynamics in CsMAFA. Basically, it shows that for FA-rich samples, the β-phase seems the most optimal phase from both structural and optoelectronic points of view.

4.4. Experimental methods

Preparation of CsMAFA perovskite layers

Quartz substrates were rinsed with acetone and ethanol in an ultrasonic bath for 10 min each. Subsequently, an oxygen plasma treatment was performed prior to layer deposition. To prepare the $Cs_{0.05}FA_{0.85}MA_{0.10}Pb(I_{0.97}Br_{0.03})_3$ (CsMAFA) precursor solution, PbI_2 (1.6 mmol, 735.3 mg), FAI (1.31 mmol, 224.4 mg), MABr (0.15 mmol, 16.2 mg), and CsI (0.08 mmol, 19.8 mg) were dissolved in 1 mL of a mixed organic solvent system comprising anhydrous DMF and anhydrous DMSO at a volume ratio of DMF : DMSO of 4:1. For the excess PbI_2 CsMAFA, 5% excess PbI_2 was added to the precursor solution.[73] A stoichiometric ratio of the precursors was prepared for the control sample denoted with CsMAFA-st. The precursor solution was stirred overnight under ~ 70 °C. The perovskite layer was deposited using an antisolvent method. A volume of 80 μL of the precursor solution was deposited evenly onto the quartz substrate, and a two-step spin-coating method was applied in a nitrogen-filled glovebox. The first step was carried out at 2000 rpm with an acceleration rate of 200 rpm/s for 10 s. The second step is at 6000 rpm with an acceleration rate of 2000 rpm/s for 30 s. As antisolvent 150 μL of diethyl ether was introduced 5 seconds before the end of the second step. The films were annealed at 120 °C for 15 min. The thickness of the perovskite layer is about 500 nm measured by the profiler meter and the cross-section SEM image.

Structural characterization

The low-temperature XRD data were recorded on the Panalytical X'pert Pro Diffractometer in Bragg-Brentano mode with a Cu-Kα anode at 45 kV, 40 mA, 1D X'Celerator detector, 0.04 Rad Soller slit, 1/2 degrees fixed exit and divergence slit. The sample was positioned inside the Anton Paar TTK 450 with Kapton windows, an Anton Paar TCU 100 temperature control unit, and a motorized controlled height stage that automatically corrects the height for the thermal expansion and measured under vacuum ($P < 7 \times 10^{-2}$ mbar). Cooling was performed with Liquid N_2 and at each temperature we waited 15 min after reaching the temperature to ensure the sample was in thermal equilibrium.

Grazing-incidence XRD was conducted on a Bruker D8 DISCOVER diffractometer (Cu-Kα) in combination with an Anton Paar XRK 900 Reactor chamber equipped with Be

windows. The measurements were performed in Bragg-Brentano configuration under vacuum (10^{-4} mbar) with variable incident angles of 0.2, 0.5, 1, 3, and 5° to tune the probed depth. On the primary side, a Goebel mirror was used together with a fixed slit of 0.1, 0.1, 0.2, 0.6, and 1.0 mm, respectively, for the incident angles to control the footprint on the film. On the secondary side, a Soller 2.5° slit was used, and the LYNXEYE XE detector was operated in 0D high-resolution mode.

Structure modeling was performed on the basis of the low-temperature XRD data. PROFEX 5.1[74] was used for both La Bail and Rietveld refinement with a pseudo-Voigt profile function. The La Bail method allows us to refine peak positions and intensities without a structure model. PROFEX 5.1 involves an instrument profile that matches our XRD configuration to correct for the broadening of the diffractometer and the background. The primary structural models used in the refinement are based on the space group *Pm-3m* (no.221) and *P4/mbm* (no.127) at 298 K, and the space group *P4/mbm* (no.127) at 270-100 K. Pure $FAPbI_3$ was assumed to suffice since CsMAFA contains only a small amount (3%) of Br and the contribution of organic cations to the XRD pattern is minimal. For the cubic phase, the FA position was fixed at C (0.5, 0.5, 0.5) and N (0.275, 0.5, 0.5) with C-N = 1.43 Å. The occupancies of C and N match with the actual situation, only the peak shape and Uiso of Pb and I were refined. For the refinement of the tetragonal phase, the same strategy is applied. In addition to the fixed FA position, two independent I positions I1(0, 0, 0) and I2(x, 0.5+x, 0.5) were refined.

Before applying the Williamson-Hall plot analysis, we stripped XRD patterns from the Kα_2 contribution at all temperatures using the DIFFRAC.EVA software from Brucker AXS. The diffraction peaks were fitted with the Voigt function to obtain peak widths.

References

[1] M. Grätzel. The light and shade of perovskite solar cells. *Nature Materials* **13** (2014), 838–842.

[2] S. D. Stranks, G. E. Eperon, G. Grancini, et al. Electron-hole diffusion lengths exceeding 1 micrometer in an organometal trihalide perovskite absorber. *Science* **342** (2013), 341–344.

[3] H. Tan, A. Jain, O. Voznyy, et al. Efficient and stable solution-processed planar perovskite solar cells via contact passivation. *Science* **355** (2017), 722–726.

[4] E. M. Tennyson, T. A. Doherty, and S. D. Stranks. Heterogeneity at multiple length scales in halide perovskite semiconductors. *Nature Reviews Materials* **4** (2019), 573–587.

[5] N. G. Park and K. Zhu. Scalable fabrication and coating methods for perovskite solar cells and solar modules. *Nature Reviews Materials* **5** (2020), 333–350.

[6] Y. He, M. Petryk, Z. Liu, et al. CsPbBr3 perovskite detectors with 1.4% energy resolution for high-energy γ-rays. *Nature Photonics* **15** (2021), 36–42.

[7] A. Fakharuddin, M. K. Gangishetty, M. Abdi-Jalebi, et al. Perovskite light-emitting diodes. *Nature Electronics* **5** (2022), 203–216.

[8] NREL. *Best Research-Cell Efficiencies: Rev. October 2023*. 2023.

[9] L. Liu, A. Mei, X. Li, et al. Incorporation of rubidium cations into perovskite solar cells improves photovoltaic performance. *Science* **354** (2016), 206–209.

[10] T. Bu, J. Li, F. Zheng, et al. Universal passivation strategy to slot-die printed SnO2 for hysteresis-free efficient flexible perovskite solar module. *Nature Communications* **9** (2018), 1–10.

[11] Y. Zhao, H. Tan, H. Yuan, et al. Perovskite seeding growth of formamidinium-lead-iodide-based perovskites for efficient and stable solar cells. *Nature Communications* **9** (2018), 1–10.

[12] M. M. Tavakoli, M. Saliba, P. Yadav, et al. Synergistic Crystal and Interface Engineering for Efficient and Stable Perovskite Photovoltaics. *Advanced Energy Materials* **9** (2019), 1–8.

[13] S. Wang, J. Jin, Y. Qi, et al. δ-CsPbI3 Intermediate Phase Growth Assisted Sequential Deposition Boosts Stable and High-Efficiency Triple Cation Perovskite Solar Cells. *Advanced Functional Materials* **30** (2020).

[14] X. Zheng, Y. Hou, C. Bao, et al. Managing grains and interfaces via ligand anchoring enables 22.3%-efficiency inverted perovskite solar cells. *Nature Energy* **5** (2020), 131–140.

[15] T. Li, S. Wang, J. Yang, et al. Multiple functional groups synergistically improve the performance of inverted planar perovskite solar cells. *Nano Energy* **82** (2021), 105742.

[16] S. You, H. Zeng, Y. Liu, et al. Radical polymeric p-doping and grain modulation for stable, efficient perovskite solar modules. *Science* **379** (2023), 288–294.

[17] M. Saliba, T. Matsui, J. Y. Seo, et al. Cesium-containing triple cation perovskite solar cells: Improved stability, reproducibility and high efficiency. *Energy and Environmental Science* **9** (2016), 1989–1997.

[18] A. S. Bati, Y. L. Zhong, P. L. Burn, et al. Next-generation applications for integrated perovskite solar cells. *Communications Materials* **4** (2023), 1–24.

[19] Y. Chen, S. Tan, N. Li, et al. Self-Elimination of Intrinsic Defects Improves the Low-Temperature Performance of Perovskite Photovoltaics. *Joule* **4** (2020), 1961–1976.

[20] H. Afshari, B. K. Durant, A. R. Kirmani, et al. Temperature-Dependent Carrier Extraction and the Effects of Excitons on Emission and Photovoltaic Performance in Cs0.05FA0.79MA0.16Pb(I0.83Br0.17)3Solar Cells. *ACS Applied Materials and Interfaces* **14** (2022), 44358–44366.

[21] R. L. Milot, G. E. Eperon, H. J. Snaith, M. B. Johnston, and L. M. Herz. Temperature-Dependent Charge-Carrier Dynamics in CH3NH3PbI3 Perovskite Thin Films. *Advanced Functional Materials* **25** (2015), 6218–6227.

[22] C. Greenland, A. Shnier, S. K. Rajendran, et al. Correlating Phase Behavior with Photophysical Properties in Mixed-Cation Mixed-Halide Perovskite Thin Films. *Advanced Energy Materials* **10** (2020), 1–11.

[23] G. W. Kim and A. Petrozza. Defect Tolerance and Intolerance in Metal-Halide Perovskites. *Advanced Energy Materials* **10** (2020), 1–6.

[24] T. J. Jacobsson, J. P. Correa-Baena, E. Halvani Anaraki, et al. Unreacted PbI2 as a Double-Edged Sword for Enhancing the Performance of Perovskite Solar Cells. *Journal of the American Chemical Society* **138** (2016), 10331–10343.

[25] T. Meier, T. P. Gujar, A. Schönleber, et al. Impact of excess PbI2 on the structure and the temperature dependent optical properties of methylammonium lead iodide perovskites. *Journal of Materials Chemistry C* **6** (2018), 7512–7519.

[26] A. Merdasa, A. Kiligaridis, C. Rehermann, et al. Impact of Excess Lead Iodide on the Recombination Kinetics in Metal Halide Perovskites. *ACS Energy Letters* **4** (2019), 1370–1378.

[27] J. Euvrard, O. Gunawan, and D. B. Mitzi. Impact of PbI2 Passivation and Grain Size Engineering in CH3NH3PbI3 Solar Absorbers as Revealed by Carrier-Resolved Photo-Hall Technique. *Advanced Energy Materials* **9** (2019), 1–10.

[28] B. Roose, K. Dey, Y. H. Chiang, R. H. Friend, and S. D. Stranks. Critical Assessment of the Use of Excess Lead Iodide in Lead Halide Perovskite Solar Cells. *Journal of Physical Chemistry Letters* **11** (2020), 6505–6512.

[29] Y. Gao, H. Raza, Z. Zhang, W. Chen, and Z. Liu. Rethinking the Role of Excess/Residual Lead Iodide in Perovskite Solar Cells. *Advanced Functional Materials* (2023).

[30] Y. Vaynzof. The Future of Perovskite Photovoltaics—Thermal Evaporation or Solution Processing? *Advanced Energy Materials* **10** (2020), 2003073.

[31] A. D. Taylor, Q. Sun, K. P. Goetz, et al. A general approach to high-efficiency perovskite solar cells by any antisolvent. *Nature Communications* **12** (2021), 1–11.

[32] L. Chen, Y. Y. Tan, Z. X. Chen, et al. Toward Long-Term Stability: Single-Crystal Alloys of Cesium-Containing Mixed Cation and Mixed Halide Perovskite. *Journal of the American Chemical Society* **141** (2019), 1665–1671.

[33] Z. Li, B. Li, X. Wu, et al. Organometallic-functionalized interfaces for highly efficient inverted perovskite solar cells. *Science* **376** (2022), 416–420.

[34] C. C. Stoumpos, C. D. Malliakas, and M. G. Kanatzidis. Semiconducting tin and lead iodide perovskites with organic cations: Phase transitions, high mobilities, and near-infrared photoluminescent properties. *Inorganic Chemistry* **52** (2013), 9019–9038.

[35] D. H. Fabini, C. C. Stoumpos, G. Laurita, et al. Reentrant Structural and Optical Properties and Large Positive Thermal Expansion in Perovskite Formamidinium Lead Iodide. *Angewandte Chemie* **128** (2016), 15618–15622.

[36] O. J. Weber, D. Ghosh, S. Gaines, et al. Phase Behavior and Polymorphism of Formamidinium Lead Iodide. *Chemistry of Materials* **30** (2018), 3768–3778.

[37] S. Kawachi, M. Atsumi, N. Saito, et al. Structural and Thermal Properties in Formamidinium and Cs-Mixed Lead Halides. *Journal of Physical Chemistry Letters* **10** (2019), 6967–6972.

[38] M. Keshavarz, M. Ottesen, S. Wiedmann, et al. Tracking Structural Phase Transitions in Lead-Halide Perovskites by Means of Thermal Expansion. *Advanced Materials* **31** (2019), 1–8.

[39] E. G. Moloney, V. Yeddu, and M. I. Saidaminov. Strain Engineering in Halide Perovskites. *ACS Materials Letters* **2** (2020), 1495–1508.

[40] G. F. Harrington and J. Santiso. Back-to-Basics tutorial: X-ray diffraction of thin films. *Journal of Electroceramics* **47** (2021), 141–163.

[41] F. Ruf, M. F. Aygüler, N. Giesbrecht, et al. Temperature-dependent studies of exciton binding energy and phase-transition suppression in (Cs,FA,MA)Pb(I,Br)3 perovskites. *APL Materials* **7** (2019).

[42] K. Galkowski, A. Mitioglu, A. Miyata, et al. Determination of the exciton binding energy and effective masses for methylammonium and formamidinium lead trihalide perovskite semiconductors. *Energy and Environmental Science* **9** (2016), 962–970.

[43] C. L. Davies, J. Borchert, C. Q. Xia, et al. Impact of the Organic Cation on the Optoelectronic Properties of Formamidinium Lead Triiodide. *Journal of Physical Chemistry Letters* **9** (2018), 4502–4511.

[44] P. Umari, E. Mosconi, and F. De Angelis. Infrared Dielectric Screening Determines the Low Exciton Binding Energy of Metal-Halide Perovskites. *Journal of Physical Chemistry Letters* **9** (2018), 620–627.

[45] M. Baranowski and P. Plochocka. Excitons in Metal-Halide Perovskites. *Advanced Energy Materials* **10** (2020).

[46] A. D. Wright, C. Verdi, R. L. Milot, et al. Electron-phonon coupling in hybrid lead halide perovskites. *Nature Communications* **7** (2016).

[47] Y. P. Varshni. Temperature dependence of the energy gap in semiconductors. *Physica* **34** (1967), 149–154.

[48] M. Ledinsky, T. Schönfeldová, J. Holovský, et al. Temperature Dependence of the Urbach Energy in Lead Iodide Perovskites. *Journal of Physical Chemistry Letters* **10** (2019), 1368–1373.

[49] B. J. Foley, D. L. Marlowe, K. Sun, et al. Temperature dependent energy levels of methylammonium lead iodide perovskite. *Materials Engineering and Sciences Division 2015 - Core Programming Area at the 2015 AIChE Annual Meeting* (2015), 581–586.

[50] M. I. Dar, G. Jacopin, S. Meloni, et al. Origin of unusual bandgap shift and dual emission in organic-inorganic lead halide perovskites. *Science Advances* **2** (2016).

[51] E. M. Hutter, R. J. Sutton, S. Chandrashekar, et al. Vapour-Deposited Cesium Lead Iodide Perovskites: Microsecond Charge Carrier Lifetimes and Enhanced Photovoltaic Performance. *ACS Energy Letters* **2** (2017), 1901–1908.

[52] D. Guo, Z. Andaji Garmaroudi, M. Abdi-Jalebi, S. D. Stranks, and T. J. Savenije. Reversible Removal of Intermixed Shallow States by Light Soaking in Multication Mixed Halide Perovskite Films. *ACS Energy Letters* **4** (2019), 2360–2367.

[53] J. Zhao, V. M. Caselli, M. Bus, B. Boshuizen, and T. J. Savenije. How Deep Hole Traps Affect the Charge Dynamics and Collection in Bare and Bilayers of Methylammonium Lead Bromide. *ACS Applied Materials and Interfaces* **13** (2021), 16309–16316.

[54] T. J. Savenije, D. Guo, V. M. Caselli, and E. M. Hutter. Quantifying Charge-Carrier Mobilities and Recombination Rates in Metal Halide Perovskites from Time-Resolved Microwave Photoconductivity Measurements. *Advanced Energy Materials* **10** (2020), 1–12.

[55] V. D'Innocenzo, G. Grancini, M. J. Alcocer, et al. Excitons versus free charges in organo-lead tri-halide perovskites. *Nature Communications* **5** (2014), 1–6.

[56] C. L. Davies, M. R. Filip, J. B. Patel, et al. Bimolecular recombination in methylammonium lead triiodide perovskite is an inverse absorption process. *Nature Communications* **9** (2018), 1–9.

[57] V. M. Caselli and T. J. Savenije. Quantifying Charge Carrier Recombination Losses in MAPbI3/C60 and MAPbI3/Spiro-OMeTAD with and without Bias Illumination. *Journal of Physical Chemistry Letters* **13** (2022), 7523–7531.

[58] K. Momma and F. Izumi. VESTA3 for three-dimensional visualization of crystal, volumetric and morphology data. *Journal of Applied Crystallography* **44** (2011), 1272–1276.

[59] O. G. Reid, M. Yang, N. Kopidakis, K. Zhu, and G. Rumbles. Grain-Size-Limited Mobility in Methylammonium Lead Iodide Perovskite Thin Films. *ACS Energy Letters* **1** (2016), 561–565.

[60] Q. Chen, H. Zhou, T. B. Song, et al. Controllable self-induced passivation of hybrid lead iodide perovskites toward high performance solar cells. *Nano Letters* **14** (2014), 4158–4163.

[61] D. Bi, W. Tress, M. I. Dar, et al. Efficient luminescent solar cells based on tailored mixed-cation perovskites. *Science Advances* **2** (2016).

[62] Q. Jiang, Z. Chu, P. Wang, et al. Planar-Structure Perovskite Solar Cells with Efficiency beyond 21%. *Advanced Materials* **29** (2017), 1–7.

[63] T. J. Jacobsson, L. J. Schwan, M. Ottosson, A. Hagfeldt, and T. Edvinsson. Determination of Thermal Expansion Coefficients and Locating the Temperature-Induced Phase Transition in Methylammonium Lead Perovskites Using X-ray Diffraction. *Inorganic Chemistry* **54** (2015), 10678–10685.

[64] F. Brivio, J. M. Frost, J. M. Skelton, et al. Lattice dynamics and vibrational spectra of the orthorhombic, tetragonal, and cubic phases of methylammonium lead iodide. *Physical Review B - Condensed Matter and Materials Physics* **92** (2015), 144308.

[65] D. J. Xue, Y. Hou, S. C. Liu, et al. Regulating strain in perovskite thin films through charge-transport layers. *Nature Communications* **11** (2020).

[66] A. Osherov, E. M. Hutter, K. Galkowski, et al. The Impact of Phase Retention on the Structural and Optoelectronic Properties of Metal Halide Perovskites. *Advanced Materials* **28** (2016), 10757–10763.

[67] B. A. Rosales, K. Schutt, J. J. Berry, and L. M. Wheeler. Leveraging Low-Energy Structural Thermodynamics in Halide Perovskites. *ACS Energy Letters* **8** (2023), 1705–1715.

[68] C. Stavrakas, S. J. Zelewski, K. Frohna, et al. Influence of Grain Size on Phase Transitions in Halide Perovskite Films. *Advanced Energy Materials* **9** (2019), 1–7.

[69] H. Xue, G. Brocks, and S. Tao. Intrinsic defects in primary halide perovskites: A first-principles study of the thermodynamic trends. *Physical Review Materials* **6** (2022), 1–11.

[70] L. Cheng, B. Xu, Y. Zeng, and L. Meng. Intrinsic defects at the interface of the FAPbI3/MAPbI3 superlattice: insight from first-principles calculations. *Physical Chemistry Chemical Physics* **25** (2023), 6369–6379.

[71] N. Liu and C. Y. Yam. First-principles study of intrinsic defects in formamidinium lead triiodide perovskite solar cell absorbers. *Physical Chemistry Chemical Physics* **20** (2018), 6800–6804.

[72] M. Uller Rothmann, J. S. Kim, J. Borchert, et al. Atomic-scale microstructure of metal halide perovskite. *Science* **370** (2020).

[73] H. Zhu, Z. Shen, L. Pan, et al. *Low-Cost Dopant Additive-Free Hole-Transporting Material for a Robust Perovskite Solar Cell with Efficiency Exceeding 21%*. 2021.

[74] N. Doebelin and R. Kleeberg. Profex: a graphical user interface for the Rietveld refinement program BGMN. *Journal of Applied Crystallography* **48** (2015), 1573–1580.

Appendices

4.A. Appendices

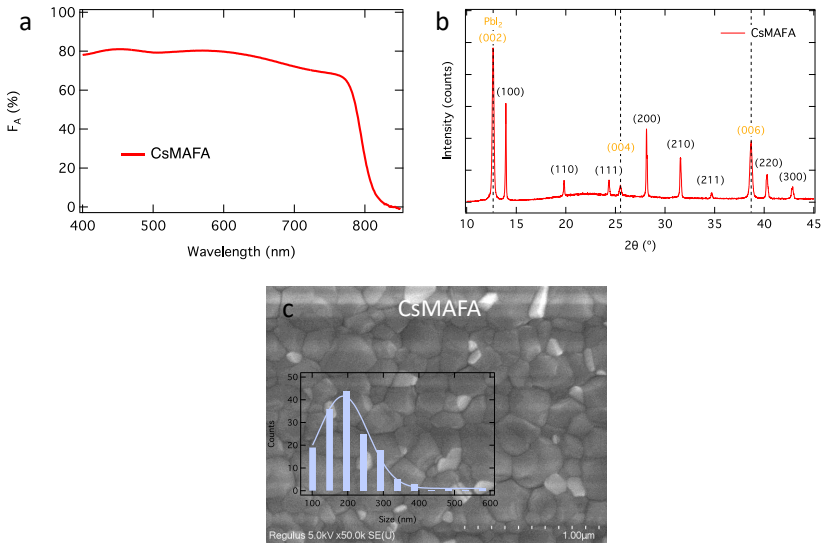

Figure 4A.1: (a) Optical absorption spectrum, (b) XRD pattern (Cu Kα X-radiation), and (c) The top view of the SEM image of the CsMAFA layer with excess PbI_2.

Table 4A.1: The XRD peak ratio of PbI_2 and (100) of CsMAFA perovskite in CsMAFA with excess PbI_2 layer.

Incident angle [°]	0.2	0.5	1	3	5
$PbI_{2(002)}$ / $CsMAFA_{(100)}$	0.247	0.153	0.112	0.157	1.184

Note S1 Williamson-Hall plot method

To quantify how the change in crystal structure affects the strain, the Williamson-Hall equation was used.[1]

$$\beta \cos\theta_{hkl} = \frac{K\lambda}{D} = 4\varepsilon \sin\theta_{hkl} \tag{4A.1}$$

[1] G. F. Harrington, et al. Back-to-Basics tutorial: X-ray diffraction of thin films. *Journal of Electroceramics* **47** (2021), 141.

Where β is the full width at half maximum (FWHM) of the peak and K is a geometrical constant, normally taken as 0.94. The λ is the X-ray wavelength, D is the crystal domain size, and ε is the strain. In the plot $\beta\cos\theta$ as a function of $\sin\theta$, ε can be deduced from the slope. If the slope is negative indicating a tensile strain in the system. On the contrary, a positive slope means the strain is compressive.

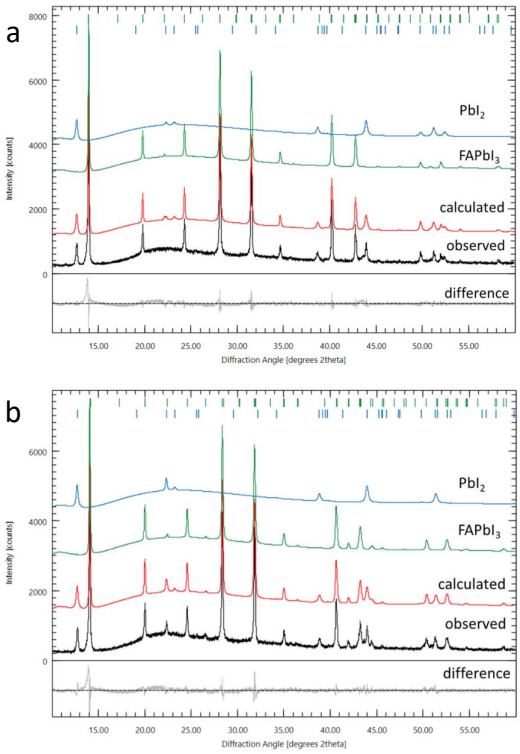

Figure 4A.2: Rietveld refinement of XRD of CsMAFA at 298 K (a, top) and 240 K (b, bottom), respectively. The recorded experimental pattern is indicated by the black line, modeled by the red line with contributions from PbI_2 (blue line) and $FAPbI_3$ (green line), and the difference by the grey line below.

Note S2 Effective mass computational method

The structure optimizations were performed using density functional theory (DFT) within the generalized gradient approximation (GGA)[2] as carried out within the Vienna ab initio simulation package (VASP).[3] The PBE exchange-correlation functional (XC functional) was used as parameterized by Predew, Burke, and Ernzerhof.[4] The crys-

[2] J. P. Perdew, et al. Accurate and simple density functional for the electronic exchange energy: Generalized gradient approximation. *Physical Review B* **33** (1986), 8800.

[3] J. P. Perdew, et al. Efficiency of ab-initio total energy calculations for metals and semiconductors using a plane-wave basis set. *Computational Materials Science* **6** (1996), 15.

[4] J. P. Perdew, et al. Generalized gradient approximation made simple. *Physical Review Letters* **77** (1996), 3865.

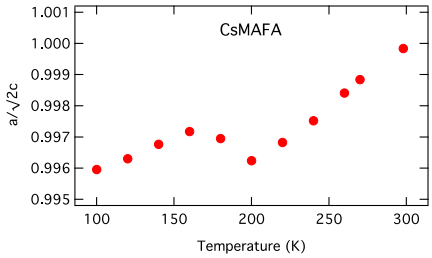

Figure 4A.3: The evolution of the lattice parameter ratio $a/\sqrt{2}c$ with temperature of the CsMAFA layer with excess PbI_2.

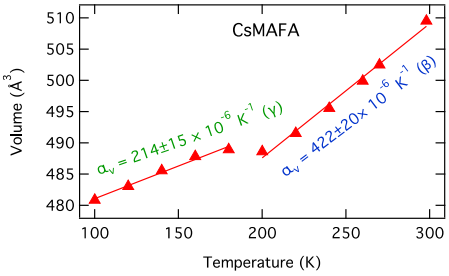

Figure 4A.4: The unit cell volume of the CsMAFA layer with excess PbI_2. The solid lines are fitted to calculate thermal expansion coefficients for the different phases.

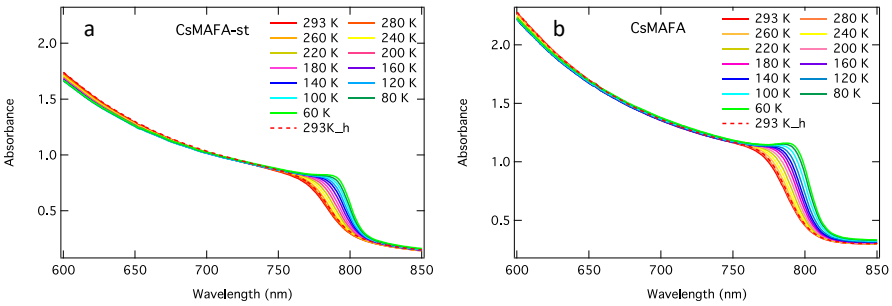

Figure 4A.5: Temperature dependence of absorption spectra of (a) the CsMAFA-st and (b) CsMAFA with excess PbI_2 layers measured using the halogen lamp output of a DH-200 Mikropack UV-VIS-NIR light source.

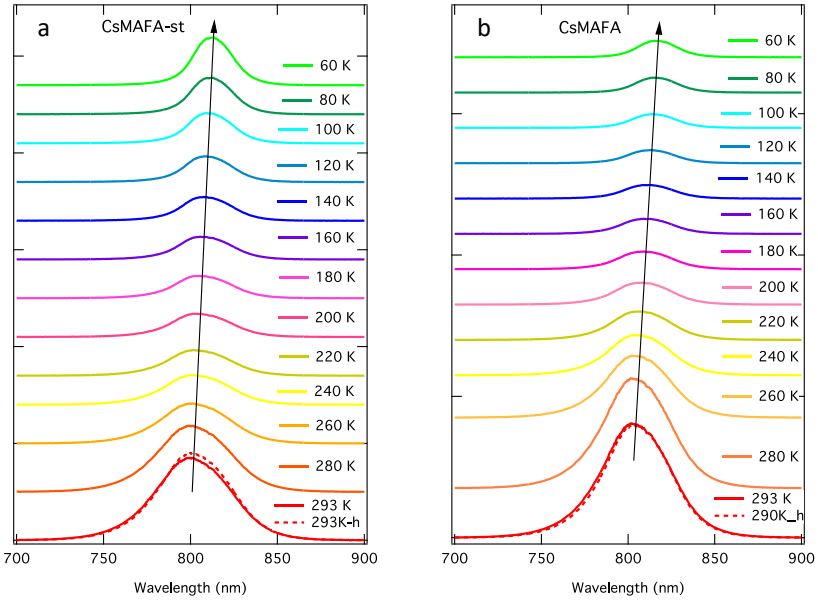

Figure 4A.6: Temperature dependence of photoluminescence spectra of (a) the CsMAFA-st and (b) CsMAFA with excess PbI_2 excited with a violet LED light (λ = 405 nm).

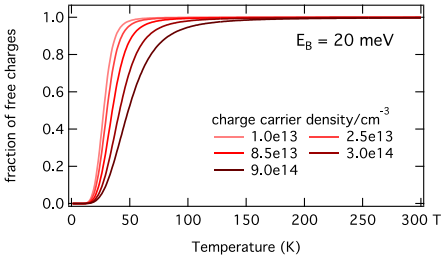

Figure 4A.7: Fraction of the initial charge carrier population leading to free charges as a function of temperature for the binding energy of 20 meV with charge carrier densities ranging from $10^{13} - 10^{14}$ cm^{-3}.

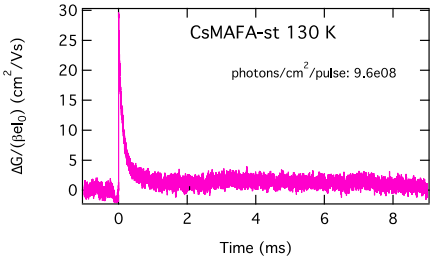

Figure 4A.8: TRMC trace recorded on a millisecond scale for the CsMAFA-st layer at 130 K with an excitation wavelength of 650 nm and an incident light intensity of 1×10^9 photons cm^{-2} per pulse.

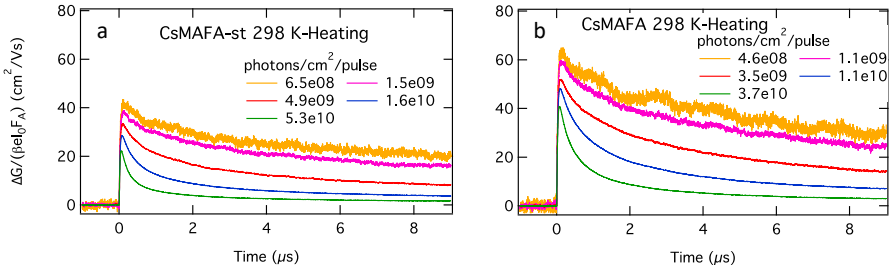

Figure 4A.9: Photoconductance traces for (a) CsMAFA-st and (b) CsMAFA with excess PbI_2 samples recorded back to 298 K upon heating on excitation at 600 nm with incident light intensities ranging from $10^8 - 10^{10}$ photons cm^{-2} per pulse.

tal structure of $FAPbI_3$ was used in the DFT simulation instead of CsMAFA-based perovskite. This approximation is fairly valid since their initial structures were obtained from the refinement of XRD measurements, except for the case of 298 K. At this temperature, XRD only provides the time-averaged positions of atoms, failing to capture the structural distortion. To address this limitation, we started the structure optimization from structures obtained at 260 K, with the lattice parameters from 298 K. In all calculations, only the organic part of the structures was allowed to relax. A $3 \times 3 \times 5$ Monkhorst-Pack k-point mesh and an energy cutoff of 500 eV were employed. Figure 4A.10 in Appendices illustrates some of the initial structures and the observed phase transitions as the temperature increases.

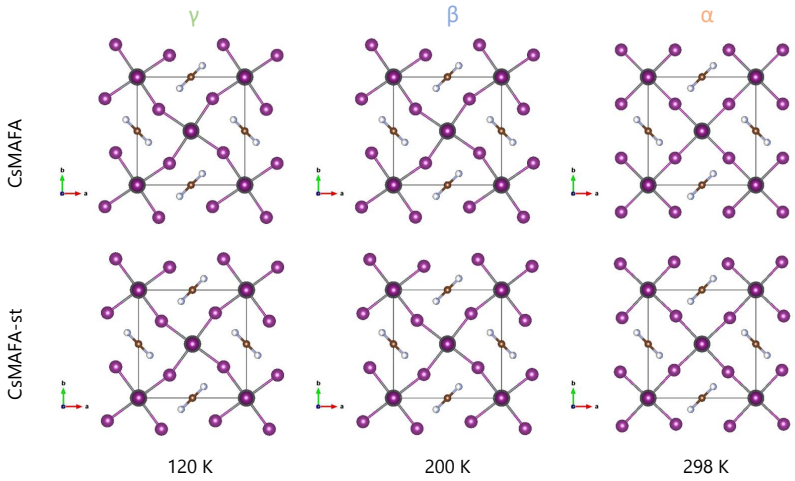

Figure 4A.10: The unit cells of CsMAFA perovskites with excess PbI_2 (top) and CsMAFA-st (bottom) at 120 K (left panels), 220 K (middle panels), and 298 K (right panels), respectively. Visualized by VESTA.

The subsequent electronic structure calculations include spin-orbit coupling (SOC) to improve the accuracy of the band structure predictions. The Brillouin zone and corresponding high-symmetry k-point path employed in the calculations are illustrated in Figure 4A.11 in Appendices.[5] The calculated data is post-processed by using the VASPKIT package.[6] Near the VBM and the CBM, the carrier effective masses satisfy:

$$m_{\text{effect}}^{-1} = \hbar^{-2} \frac{\partial^2 E}{\partial k^2} \tag{4A.2}$$

where k is the wave vector and E is the energy. To obtain the effective mass, the second-order derivative of energy with respect to the wave vector is calculated. This calculation

[5] W. Setyawan, et al. High-throughput electronic band structure calculations: Challenges and tools. *Computational Materials Science* **49** (2010), 299.
[6] V. Wang, et al. VASPKIT: A user-friendly interface facilitating high-throughput computing and analysis using VASP code. *Computer Physics Communications* **267** (2021), 108033.

was performed in two different directions from Z to A and from Z to Γ along the k-points path in the Brillouin zone. Subsequently, the m_{effect} was obtained as follows:

$$m_{\text{effect}} = \frac{\hbar^2}{\frac{\partial^2 E}{\partial k^2} \mid k=k_0} \tag{4A.3}$$

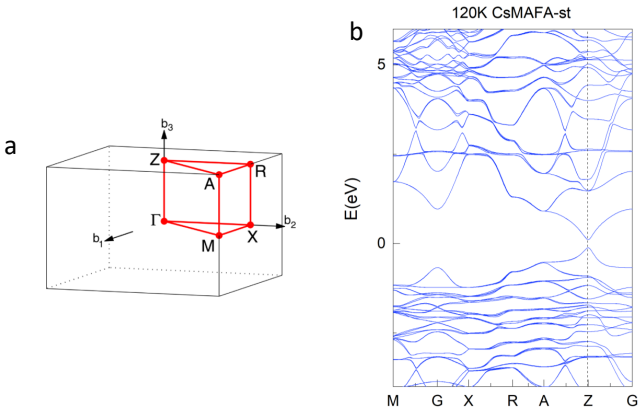

Figure 4A.11: (a) The Brillouin zone of a tetragonal lattice. (b) The band structure of CsMAFA-st at 120 K.

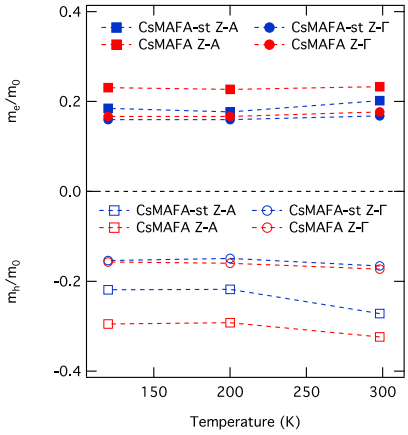

Figure 4A.12: The calculated effective mass of electrons and holes for CsMAFA-st and CsMAFA with excess PbI_2 at 298, 200, and 120 K, respectively, including the spin-orbit coupling effect.

Note S3 TRMC fitting differential equations

Table 4A.2: The calculated effective mass of electrons and holes for CsMAFA-st and CsMAFA with excess PbI_2 in different phases including the spin-orbit coupling effect.

Temperature [K]	Direction	Electron mass [m_e]		Hole mass [m_h]	
		CsMAFA-st	CsMAFA	CsMAFA-st	CsMAFA
298	$Z \rightarrow A$	0.202	0.233	-0.272	-0.324
	$Z \rightarrow \Gamma$	0.168	0.177	-0.166	-0.173
200	$Z \rightarrow A$	0.177	0.227	-0.218	-0.292
	$Z \rightarrow \Gamma$	0.160	0.167	-0.149	-0.160
120	$Z \rightarrow A$	0.185	0.231	-0.219	-0.295
	$Z \rightarrow \Gamma$	0.160	0.167	-0.154	-0.157

$$\frac{dn_e}{dt} = G_C - k_2\left(n_h + p_0\right)n_e - k_T\left(N_T - n_t\right)n_e - k_s n_e + k_s' n_{ts} \tag{4A.4}$$

$$\frac{-dn_h}{dt} = -G_C + k_2\left(n_h + p_0\right)n_e + k_D n_t\left(n_h + p_0\right) \tag{4A.5}$$

$$\frac{dn_t}{dt} = k_T\left(N_T - n_t\right)n_e - k_D n_t\left(n_h + p_0\right) \tag{4A.6}$$

$$\frac{dn_{ts}}{dt} = k_s n_e - k_s' n_{ts} \tag{4A.7}$$

The global, iterative fitting procedure can be summarized as follows:

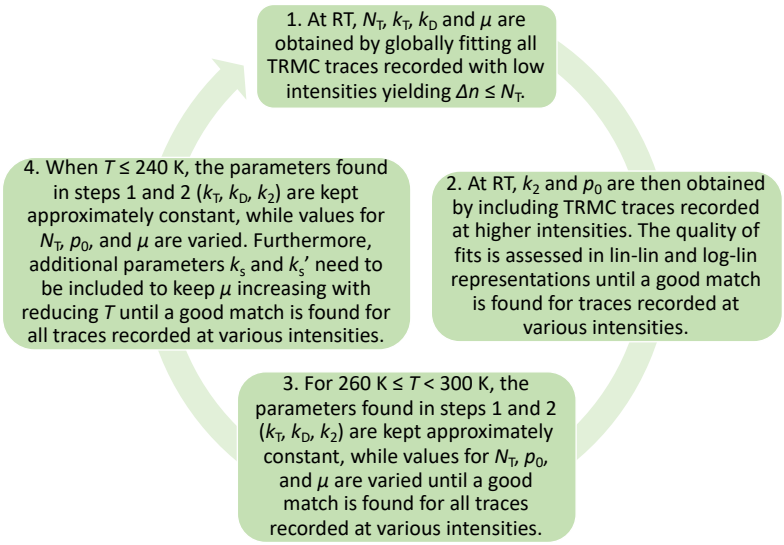

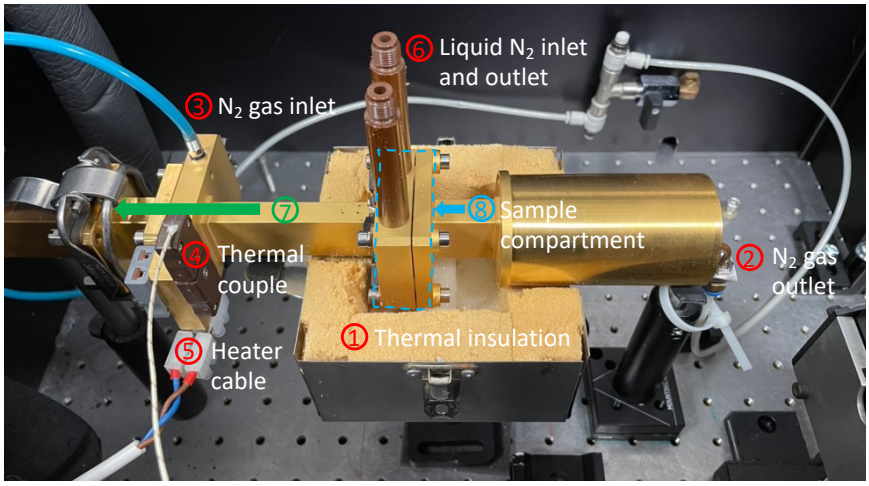

Figure 4A.13: Photo of the TRMC cell with cooling system. The main components are indicated by red, green, and blue numbers and white text.
1. A thermal insulation box is used to allow cooling to liquid N_2 (Only the lower part is shown).
2. N_2 gas outlet to avoid condensation on the optical entrance window.
3. N_2 gas inlet to keep the pressure inside the cell constant.
4. Connection to thermal couple, which is mounted close to the sample inside the central brass part.
5. Connection to the resistive heaters, which are mounted on top of the central brass part.
6. Liquid N_2 in and outlet running around the sample compartment.
7. Connection with microwave source and detection circuitry (marked in green).
8. Sample compartment (marked in blue).

Note S4 Absorption, PL and TRMC for the CsMAFA-st layer

For the CsMAFA-st layer, the optical and TRMC were carried out in the same way as CsMAFA. Regarding the optical properties in CsMAFA-st, a similar absorption is observed (Figure 4A.5a in Appendices). However, CsMAFA shows a subtle redshift of 6 meV compared with the CsMAFA-st layer (Figure 4A.5b in Appendices), which has been observed previously in $MAPbI_3$. It is suggested that the conduction band level becomes deeper with the addition of excess PbI_2, which is in line with the use of the surface passivation of potassium iodide.[7]

[7] B. Roose, et al. Critical assessment of the use of excess lead iodide in lead halide perovskite solar cells. *Journal of Physical Chemistry Letters* **11** (2020), 6505.

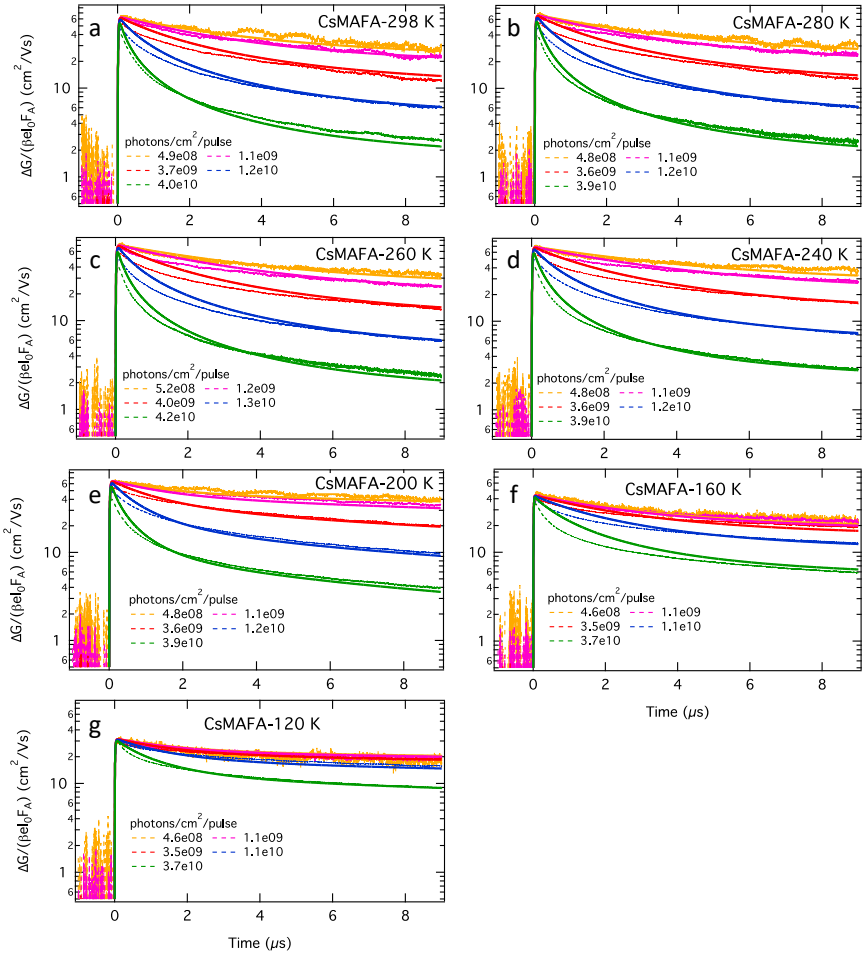

Figure 4A.14: Photoconductance traces for CsMAFA with excess PbI_2 samples at (a) 298 K, (b) 280 K, (c) 260 K, (d) 240 K, (e) 200 K, (f) 160 K, and (g) 120 K recorded on excitation at 600 nm with incident light intensities ranging from $10^8 - 10^{10}$ photons cm^{-2} per pulse. The fits (solid line) are added to the experimental data (dotted line).

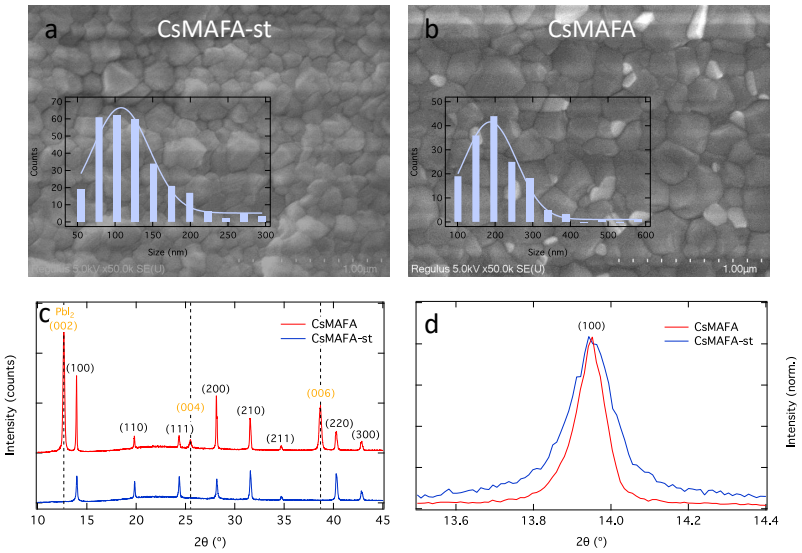

Figure 4A.15: (a, b) The top view of SEM images of the CsMAFA-st and CsMAFA with excess PbI_2, respectively. The inset shows the statistical average size of the crystal domain. (c) XRD patterns (Cu Kα X-radiation) for CsMAFA layers with stoichiometry and excess PbI_2. The dashed line indicates the presence of excess PbI_2. (d) The comparison of (100) peak width of perovskite between two layers.

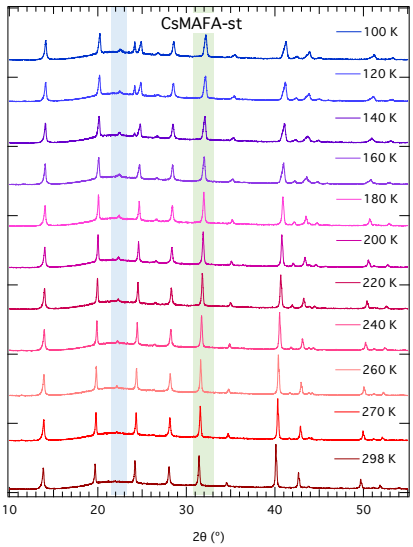

Figure 4A.16: Temperature dependence of an overview of the XRD patterns (Cu Kα X-radiation) of CsMAFA-st layer deposited on quartz.

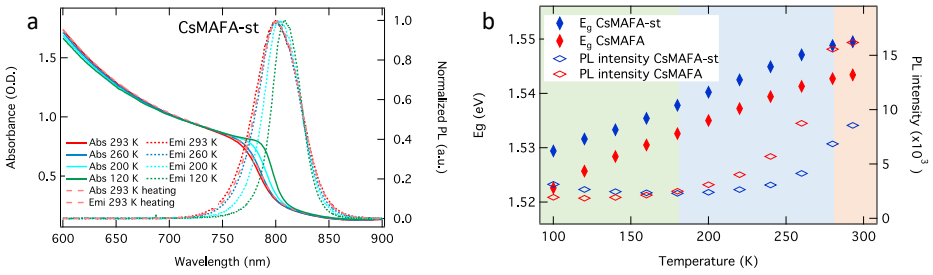

Figure 4A.17: (a) Temperature dependence of the absorption (solid line, left axis) and normalized photoluminescence spectra (dotted line, right axis) of the CsMAFA-st layer excited with a violet LED light (λ = 405 nm). Dashed lines indicate the data recorded upon heating. (b) Evolution of bandgap energy (E_g) (left axis) and PL intensity (right axis) as a function of temperature for the CsMAFA-st and CsMAFA layers.

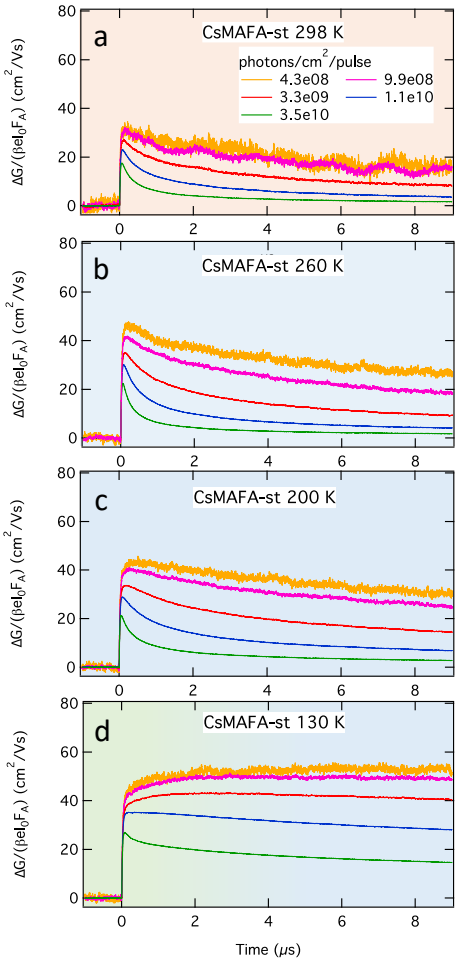

Figure 4A.18: Photoconductance traces for the CsMAFA-st layer at (a) 298 K, (b) 260 K, (c) 200 K, and (d) 130 K recorded on excitation at 600 nm with incident light intensities ranging from $10^8 - 10^{10}$ photons cm^{-2} per pulse.

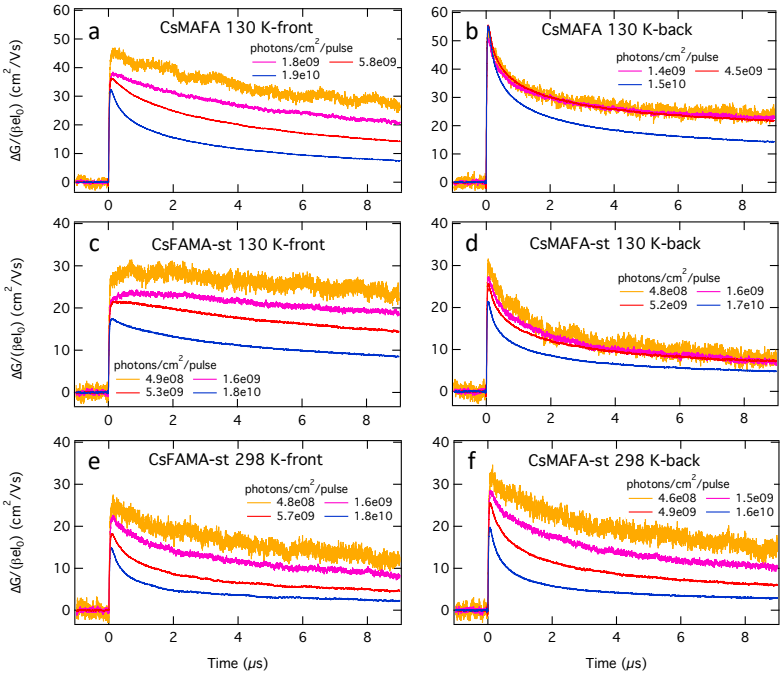

Figure 4A.19: Experimentals TRMC traces for (a, b) CsMAFA and (c-f) CsMAFA-st recorded at (a-d) 130 and (e, f) 298 K on excitation at 650 nm for the (a, c, e) front and (a, d, f) back excitation at incident light intensities ranging from 10^8 to 10^{10} photons cm^{-2} per pulse.

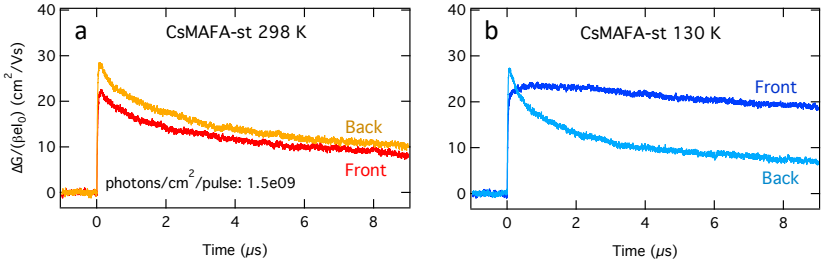

Figure 4A.20: TRMC traces for CsMAFA-st recorded at (a) 298 K and (b) 130 K on excitation at 650 nm for the front and back excitation at an incident intensity of around 2×10^9 photons cm^{-2} per pulse.

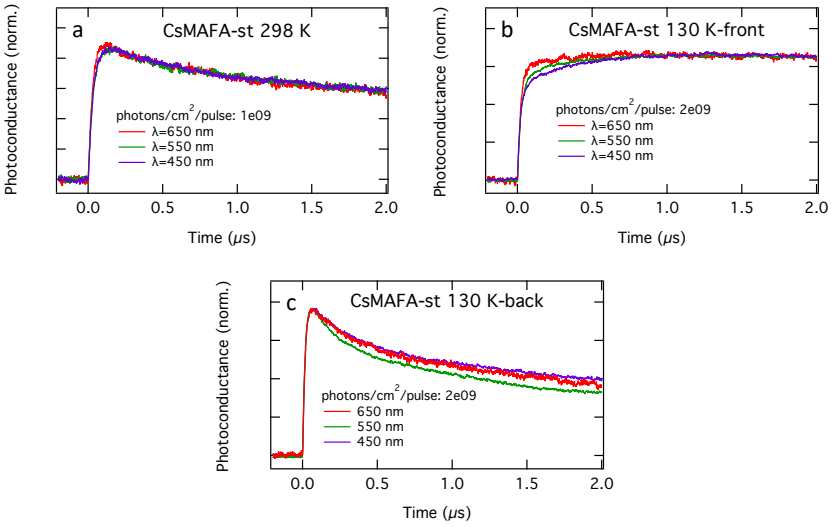

Figure 4A.21: TRMC traces recorded on excitation at 650, 550, and 450 nm with an incident light intensity of 2×10^9 photons cm^{-2} per pulse for the CsMAFA-st layer at (a) 298 K and (b) 130 K on front and (c) back excitation„ respectively.

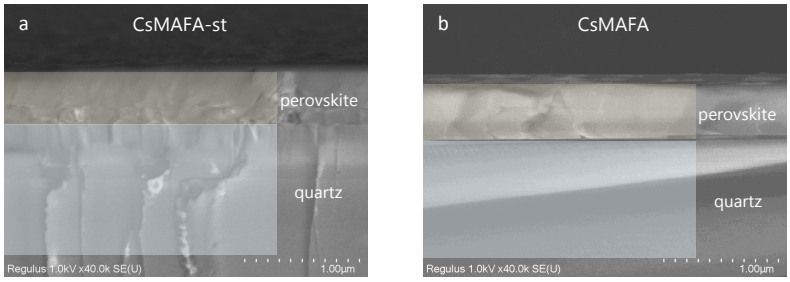

Figure 4A.22: Scanning electron microscopy (SEM) cross-section images of CsMAFA-st and CsMAFA with excess PbI_2 deposited on quartz. Light yellow and blue shades are guided by perovskite and quartz, respectively.

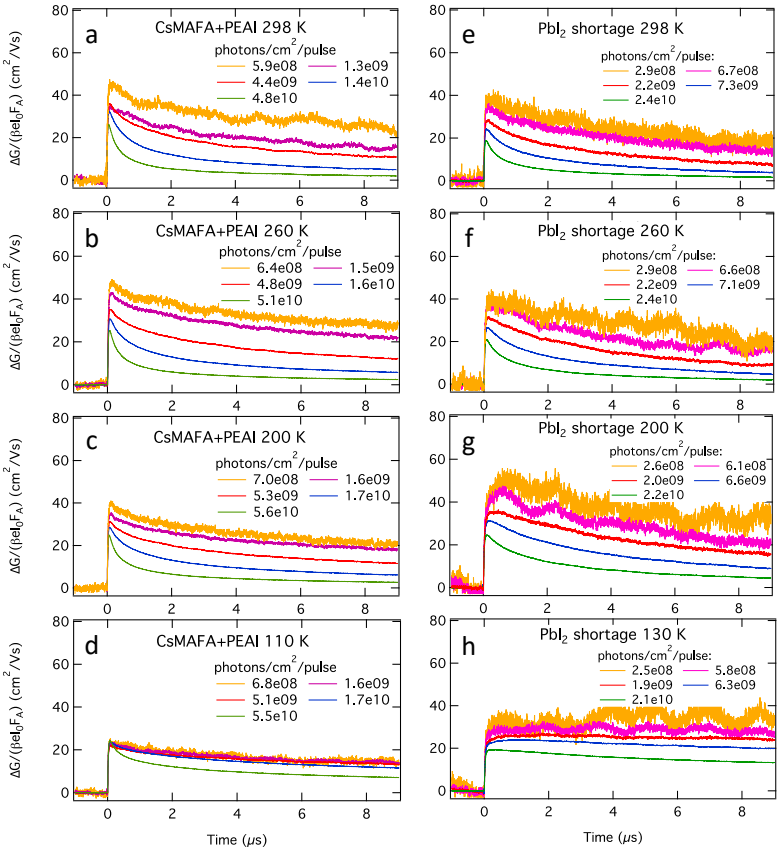

Figure 4A.23: Photoconductance traces for CsMAFA with PEAI post-treatment (a-d, left panels) and CsMAFA with 5% PbI_2 shortage (e-h, right panels) at 298 K, 260 K, 200 K, and 130 K recorded on excitation at 600 nm with incident light intensities ranging from $10^8 - 10^{10}$ photons cm^{-2} per pulse.

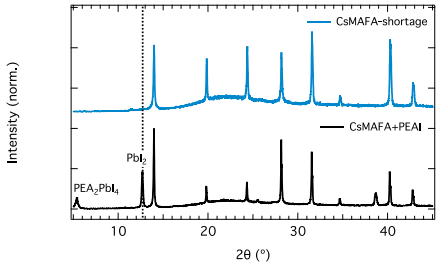

Figure 4A.24: XRD patterns (Cu Kα X-radiation) for CsMAFA-shortage and CsMAFA+PEAI layers.

5

Long-lived Charge Extraction in CsMAFA Perovskites in n-i-p and p-i-n Structures

To increase the V_{OC} in solar cells based on CsMAFA, reducing recombination processes at the interfaces with transport layers (TLs) is key. In this Chapter, we investigated the charge carrier dynamics in bilayers and trilayers of CsMAFA combined with TLs using TRMC without and with bias illumination (BI). In the bilayers, we find balanced mobilities for electrons and holes in CsMAFA and nearly quantitative carrier extraction. The small, rapidly decaying TRMC signal for n-i-p- and p-i-n triple layers indicate both carriers are extracted. Applying BI leads to the charging of the TLs and the corresponding electric field prevents additional charge extraction, which demonstrates long-lived charge separation over the CsMAFA/TLs. Most importantly, for all bilayer combinations showing long-lived charge separation, an increase of the quasi-Fermi level splitting with respect to that of the CsMAFA layer is found.

This chapter is based on

J. Zhao, L.M. van der Poll, S. Looman, J. Yan, J. Thieme, B. Ibrahim and T.J. Savenije. Long-lived Charge Extraction in CsMAFA-based Perovskites in n-i-p and p-i-n Structures (Submitted)

5.1. Introduction

Metal halide perovskites (MHPs) have attracted worldwide research attention in the last decade due to their excellent optoelectronic properties and to the rapidly increasing performance of MHP-based solar cells,[1–5] with recorded power conversion efficiencies (PCEs) of 26.1% in conventional n-i-p structures[6] and 24.6% in inverted p-i-n configurations.[7] These impressive PCEs can be partially attributed to extensive interface engineering to reduce the non-radiative recombination at the interfaces with the electron and hole transport layers (TLs).[8–15] Yet, despite this impressive progress in performance, in order to further reduce deficits between the obtained and maximum theoretical open-circuit voltage (V_{OC}),[16–18] it is crucial to understand the carrier dynamics including charge transport, extraction, and recombination at the interfaces. Photoluminescence quantum yield (PLQY) measurements revealing the quasi-Fermi level splitting (QFLS) in various MHP absorbers with hole or/and electron TLs show that non-radiative charge carrier recombination still occurs at most interfaces.[17,19,20] For this reason, an in-depth understanding of the carrier dynamics at the interfaces is of vital importance for further optimization.

Characterization of charge carrier dynamics at the interfaces has been investigated by employing various techniques ranging from laser spectroscopy to electrical measurements.[21–25] However, transient absorption or optically pump terahertz probe measurements are typically limited by the high excitation intensities required, leading to higher-order recombination processes and thus disguising the charge extraction.[26] Moreover, data interpretation of time-resolved photoluminescence measurements is not straightforward given their inhomogeneous excitation region of the pulsed laser, and the calculated QFLS derived from PLQY is not very accurate. In addition, transient electrical measurements, such as transient photovoltage decay or intensity-modulated photocurrent/photovoltage spectroscopy on complete PSCs can elucidate carrier recombination mechanisms under operating conditions.[9,27] Nevertheless, the complexity of multiple interfaces at which various photophysical processes on different timescales occur in combination with undesired ion diffusion affecting the internal electric field makes the interpretation of such measurements very challenging.[28,29]

In this Chapter, the contactless time-resolved microwave conductance (TRMC) technique was used to investigate carrier extraction and recombination at different interfaces in n-i-p and p-i-n stacks, by directly comparing the carrier dynamics in the perovskite absorber layer to those obtained in bilayer and tri-layer systems. As the absorber, $Cs_{0.05}MA_{0.10}FA_{0.85}Pb(I_{0.97}Br_{0.03})_3$ (CsMAFA) was chosen since corresponding PSCs showed excellent performance with improved thermal and phase stability.[10,30] C_{60} was selected as electron TL, while for the hole TL, either Spiro-OMeTAD (n-i-p) or PTAA (p-i-n) was chosen. First of all, by analyzing the TRMC traces recorded with various incident light intensities, we demonstrate that carrier extraction occurs in all bilayers and trilayers by the reduction of the TRMC signal height and the change in the decay kinetics. Furthermore, pulsed excitation in combination with bias illumination (BI) demonstrates long-lived carrier extraction over the CsMAFA/TL interfaces, as reflected by the almost comparable TRMC signals in bare CsMAFA and TL/CsMAFA/TL trilayers. Finally, we examine how charge collection and recombination at the interface affect the quasi-Fermi level splitting, which is derived from steady-state microwave conductivity (SSMC) mea-

surements.

5.2. Results and discussion

$Cs_{0.05}MA_{0.10}FA_{0.85}Pb(I_{0.97}Br_{0.03})_3$ (CsMAFA) films with 5% excess PbI_2 were prepared using the spin-coating method using ethyl acetate as antisolvent (see Experimental methods for more details). The XRD pattern of a bare CsMAFA film is shown in Figure 5.1a, confirming the presence of a small excess PbI_2 and the cubic phase of CsMAFA, in agreement with the simulated cubic powder XRD pattern.[31,32] Figure 5.1b presents the top view SEM image of CsMAFA displaying the compact and polycrystalline nature of the perovskites. In Figure 5.1c the absorption and photoluminescence (PL) spectra of CsMAFA are provided, showing optical absorption onset and PL maximum at around 800 nm (1.55 eV) in line with the literature.[13,33]

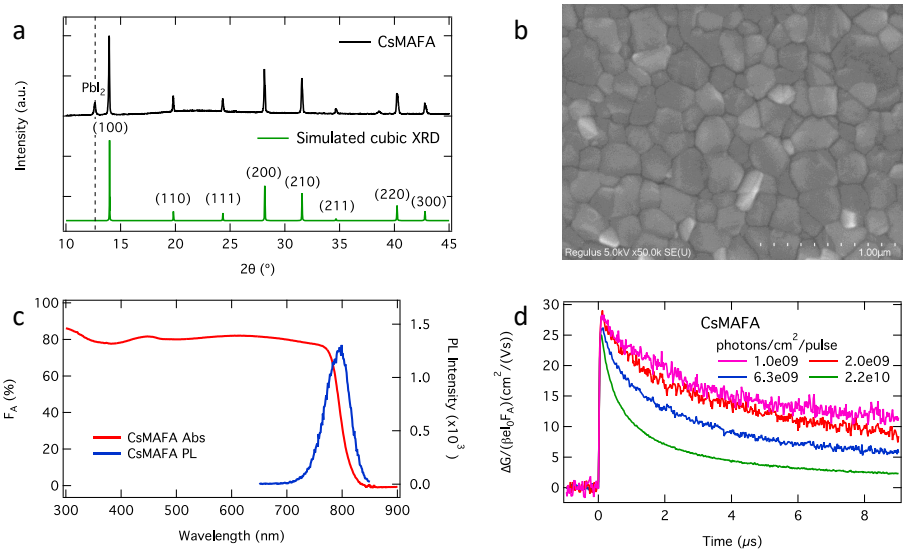

Figure 5.1: (a) The XRD pattern (Cu Kα X-radiation) and simulation of CsMAFA, (b) The top view of the SEM image, (c) Optical absorption and photoluminescence spectra, and (d) Experimental photoconductance traces for CsMAFA recorded on excitation at 650 nm with incident light intensities ranging from $10^9 - 10^{10}$ photons cm^{-2} per pulse.

The time-resolved microwave conductivity (TRMC) technique was used to investigate the mobilities and recombination dynamics of photoexcited charge carriers in CsMAFA. Figure 5.1d shows the photoconductance traces (ΔG) normalized by the number of absorbed photons as a function of time. The initial increase of the signal originates from the generation of free charge carriers, while the decay is attributed to the immobilization of excess charge carriers via trapping or the recombination of electrons and holes. At low intensities, the decay kinetics are predominantly determined by non-radiative, first-order recombination mediated via deep trap states. With increasing laser pulse intensities, the decay kinetics become faster due to enhanced second-order

electron-hole recombination. This type of behavior has been observed and described previously for other perovskites.[34–37] The maximum signal height represents the product of the free charge carrier generation yield, φ, and the sum of the electron and hole mobility, $\Sigma\mu$ (See Equation 2.3 in the Experimental methods in Chapter 2). Given the low exciton binding energy of 10-24 meV reported for FA-rich MHPs,[38–42] the majority of the excitons will dissociate into free charges, and the free charge carrier generation yield, φ, will be close to unity. Hence, the total carrier mobility of holes and electrons in CsMAFA, i.e. the TRMC signal height, is around 30 $cm^2\,(Vs)^{-1}$ and the lifetimes of carriers are relatively long, on the order of microseconds at incident fluences ranging from $10^9 - 10^{10}$ photons cm^{-2} per pulse. Therefore, we conclude that the obtained CsMAFA films exhibit good optoelectronic properties with a uniform and polycrystalline structure.

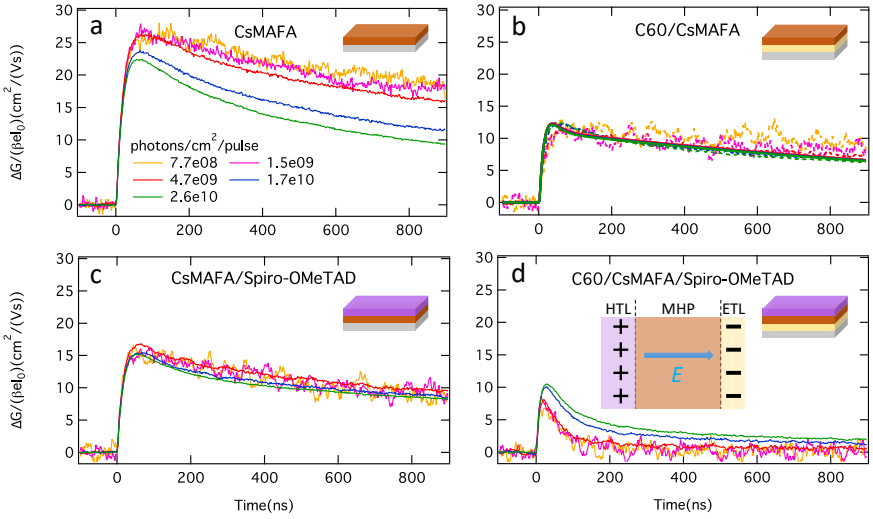

Figure 5.2: TRMC traces for CsMAFA (a), C_{60}/CsMAFA (b), CsMAFA/Spiro-OMeTAD (c), and C_{60}/CsMAFA/Spiro-OMeTAD (d) deposited on quartz (light grey) recorded on excitation at 650 nm with incident light intensities ranging from $10^9 - 10^{10}$ photons cm^{-2} per pulse. The fits for the C_{60}/CsMAFA bilayer are indicated by the solid lines. A simplified parallel-plate capacitor illustration of a trilayer system after charge extraction is shown in the inset.

For a complete perovskite device, not only the absorber layer but also the collection of charges by the transport layers (TLs) is very important to achieve high performance. In order to investigate the charge collection from CsMAFA into the TLs, the charge carrier dynamics in neat CsMAFA were directly compared with those of the bilayers (TL/MHP or MHP/TL) and sandwich-like trilayers (TL/MHP/TL). The configurations of CsMAFA and TLs are identical to the configurations used in perovskite solar cells to allow direct comparison. Hence, two different types of stacks, i.e., n-i-p (ETL/MHP/HTL) and p-i-n (HTL/MHP/ETL), were studied. First, we focused on the n-i-p architecture, where C_{60} was used as the electron transport layer (ETL) and Spiro-OMeTAD as the hole transport layer (HTL) (see Figure 5A.1 in Appendices for energy band diagrams). For all systems, we excited samples from the sample side using an excitation of 650 nm to ensure a ho-

mogeneous generation profile in CsMAFA (see Figure 5A.2). More importantly, the absorption of TLs at 650 nm is negligible (see Figure 5A.3 in Appendices), which means that the TRMC signal only originates from carriers initially generated in CsMAFA and is not affected by the parasitic absorption by the TLs.

First of all, on comparing the neat CsMAFA layer (Figure 5.2a) and bilayers (Figures 5.2b, c), a substantial reduction in TRMC signal is observed in both bilayers, in agreement with our previous reports in $MAPbI_3$.[43,44] Since the mobility in TLs is at least one order of magnitude lower than in CsMAFA,[24] the reduced signal height implies that electrons and holes are injected into their respective layers while the remaining TRMC signal originates from carriers remaining in the perovskite (holes or electrons). Furthermore, we noticed that the sum of TRMC signals in bilayers (Figures 5.2b, c) is very similar to that in CsMAFA, suggesting that carriers were nearly completely transferred to their corresponding TLs. Moreover, it also demonstrates that the electric field due to charge accumulation at the CsMAFA/TL interface does not yet hamper the charge collection. Additionally, the reduction in TRMC signal in both bilayers is very comparable, indicating that their individual mobilities are rather similar, consistent with what we previously reported in Chapter 4. Apart from the change in signal size, two additional observations can be noticed. First, for both bilayers, the lifetimes of the charge carriers are elongated in comparison to neat CsMAFA, which can be explained by the slow recombination of electrons and holes occurring over the interface since they are physically separated. Secondly, unlike in CsMAFA, all TRMC traces overlap at different intensities and have no second-order recombination features, meaning that in bilayers the carrier decay is dominated by first-order recombination via the interface.

Knowing that all these bilayers can efficiently extract carriers, it is of interest to examine how charge carriers in trilayer systems behave. As shown in Figure 5.2d, the TRMC traces recorded in the trilayer show a significant reduction in signal height, and the lifetimes of carriers are considerably shortened compared to both those of the single and bilayers. If complete extraction of carriers from CsMAFA to their respective TL happens rapidly in the trilayer, a very small, negligible TRMC signal should be expected due to the limited carrier mobility in the TLs. In reality, a small TRMC signal still remains. To examine whether the charge carrier diffusion time (τ) in CsMAFA is responsible for the remaining TRMC signal, we calculated τ across the CsMAFA film using Equation 1.2 in Chapter 1, here μ taken as 15 $cm^2\,(Vs)^{-1}$ in CsMAFA. Assuming that diffusion length, L_D, is equal to the thickness of the CsMAFA film of 500 nm, τ amounts to 6 ns. Although charge collection between CsMAFA and TLs is expected to be between picosecond and sub-nanosecond time scales, the actual extraction time of carriers is limited by carrier diffusion in CsMAFA. Since the response time of the cavity used in this work is 18 ns, the effect of the instrumental response function (IRF) on the measured traces for a ΔG of 6 ns is shown in Figure 5A.4 in Appendices, indicating that a small TRMC signal might still be retained. Most importantly, the short TRMC signal implies that almost complete carrier extraction occurs $I_0 < 5 \times 10^9$ photons cm^{-2} per pulse.

Furthermore, contrary to what we usually observe in single perovskite layers,[36,45] the intensity dependence in the trilayer exhibits longer charge carrier lifetimes and higher TRMC signals with increasing incident light intensities. One possible explanation for this increased signal is that the extracted charge carriers in their respective TLs give rise

to an internal electric field in the trilayer system, as depicted in the inset of Figure 5.2d. The direction of this E-field is from the HTL towards the ETL, which is opposite to the carrier extraction, hindering further collection of carriers. It is worth noting that when $I_0 > 5 \times 10^9$ photons cm^{-2} per pulse, corresponding to a carrier density of 1×10^{13} cm^{-3}, this resulting electric field is sufficiently large to reduce further charge extraction. In addition, we measured the photoconductance of both bilayers and trilayers using back-side (quartz side) excitation at 650 nm, as shown in Figure 5A.5 in Appendices. The TRMC signal height shows small fluctuations, which is due to the differences in reflection by the perovskite and quartz substrate. However, the charge carrier dynamics for the bilayers and trilayers are fairly comparable and hence, we conclude that the charge carrier collection occurs independently of the illumination side.

Besides PSCs in conventional n-i-p architectures, inverted inverted p-i-n PSCs have attracted more attention owing to their long operational stability derived from non-doped HTLs[7] and their successful integration with silicon solar cells into multijunction tandem solar cells.[46] Hence, also bilayers and trilayers with a p-i-n configuration were studied. Herein, we used PTAA as the HTL and C_{60} as the ETL. On comparing Figure 5A.6a with 5A.6b in Appendices, corresponding to neat CsMAFA and PTAA/CsMAFA bilayer, a similar carrier decay behavior to that observed in the n-i-p structure is found upon introduction of the HTL, i.e. a reduction in TRMC signal and an elongation of the lifetime of charge carriers. For the CsMAFA/C_{60} bilayer, it is evident that charge extraction to C_{60} occurs, as shown by the drop in maximum signal. However, only short-lived TRMC traces could be measured, possibly because C_{60} is not compatible with the CsMAFA top surface, leading to rapid interfacial recombination via a trap-assisted process.[20] Nevertheless, in the PTAA/CsMAFA/C_{60} trilayer system, the same features as in C_{60}/CsMAFA/Spiro are observed.

Table 5.1: Rate constants, trap densities, and mobilities extracted from the fits to TRMC traces of CsMAFA, C_{60}/CsMAFA and CsMAFA/C_{60} bilayers.

	CsMAFA	C_{60}/CsMAFA	CsMAFA/C_{60}
k_2 [$\times 10^{-9}$ cm^{3}s^{-1}]	3.5	3.5	3.5
k_T [$\times 10^{-9}$ cm^{3}s^{-1}]	5	5	5
k_D [$\times 10^{-9}$ cm^{3}s^{-1}]	0.5	0.5	0.5
N_T [$\times 10^{13}$ cm^{-3}]	6.5	6.5	6.5
p_0 [$\times 10^{13}$ cm^{-3}]	0.8	0.8	0.8
μ_e [cm^2(Vs)$^{-1}$]	14	14	14
μ_h [cm^2(Vs)$^{-1}$]	14	14	14
k_{ext} [$\times 10^7$ s^{-1}]	-	6	6
k_{rec} [$\times 10^7$ s^{-1}]	-	0.06	0.6

To further verify the occurrence of long-lived charge extraction from CsMAFA to their respective TLs in the trilayers, we compared TRMC measurements of a bare CsMAFA layer with a C_{60}/CsMAFA/Spiro trilayer under various bias illuminations (BI) using a white LED, as illustrated in Figure 5.3b. The measured TRMC traces are shown in Figure 5.4. First, for the bare CsMAFA layer under 0.86 mW BI (corresponding to 0.04 sun)

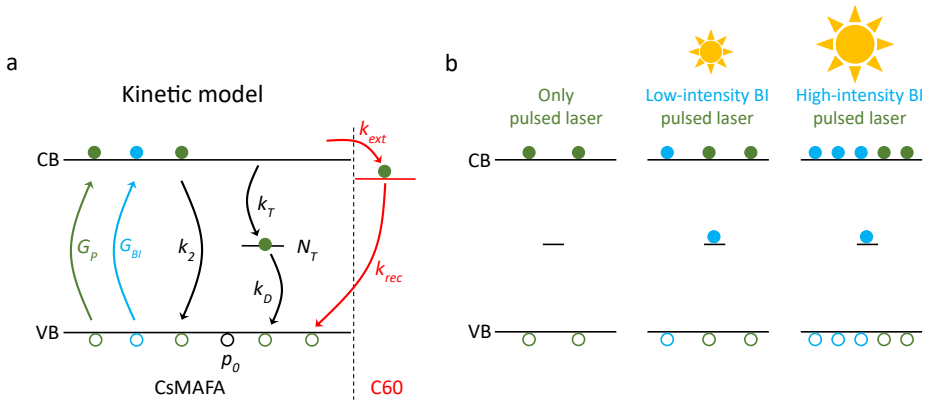

Figure 5.3: (a) Kinetic model of charge carrier processes initiated by optical excitation of CsMAFA. G_P and G_{BI} represent the photo generation of charge carriers by pulsed laser alone or in combination with bias illumination (BI); k_2 depicts the second-order recombination rate. Electron trap-mediated recombination is described by trapping rate, k_T, and depopulation rate, k_D. Electrons are collected by C_{60} and consecutively recombined with holes in CsMAFA are represented by extraction rate k_{ext} and recombination rate k_{rec}, respectively (red arrows). (b) Illustration of photo-generated carriers in CsMAFA under pulsed laser combined with bias illumination. A BI arrives on the sample prior to the pulsed laser. Carriers generated by pulsed laser and BI are represented by green and light blue circles, respectively.

(Figure 5.4a), charge carrier decays become slightly faster and display less dominant second-order recombination. This can be attributed to the higher excess carrier concentration under BI. However, the concentration of excess carriers generated by the BI is still comparable to that generated by the pulsed illumination. When BI is increased to 5 mW (~ 0.3 sun), the decay is much faster and exhibits a pseudo-first-order recombination behavior, which indicates that carrier recombination is mainly governed by the charge carriers generated by the BI.

In contrast to neat CsMAFA, the trilayer system exhibits higher TRMC signals and longer carrier lifetimes with BI. Using low-intensity BI (0.86 mW) the TRMC signals are increased by approximately fifty percent in comparison to that without BI. On further increasing the BI to 7 mW, the TRMC signal height is even higher and almost comparable to that in neat CsMAFA. These observations can only be explained by the fact that under BI, charge extraction to the TLs occurs leading to a charge carrier equilibrium between CsMAFA and the TLs long before pulse excitation. At low BI, the carriers in TLs are not saturated, and further charge extraction of carriers induced by the laser pulse can still take place to a certain degree. At high BI, the TLs appear to be almost saturated and no further charge extraction is feasible. Therefore, similar TRMC signals are observed in the single and triple layers under high BI.

Then, the same TRMC measurements with BI were carried out on neat CsMAFA and PTAA/CsMAFA/C_{60} trilayer (p-i-n configuration, see Figure 5A.6 in Appendices). For the CsMAFA single layer (Figures 5A.6a-c in Appendices), almost identical features are noticed as described above. Unlike the C_{60}/CsMAFA/Spiro trilayer, we did not observe any obvious difference in carrier decay behavior between low and high BI in the p-i-n tri-

layer (Figures 5A.6d-f in Appendices), implying that the TLs used in p-i-n architecture saturates at a relatively low energy threshold with respect to the regular n-i-p structure, as both the PTAA and C_{60} layers are relatively thin on the order of tens of nm. It is worth mentioning that the charge carrier dynamics after removing the BI are very similar to the initial TRMC traces recorded with only the pulsed laser (see Figure 5A.9 in Apendices). Hence these BI-induced changes are fully reversible and all perovskites and TLs are stable during BI.

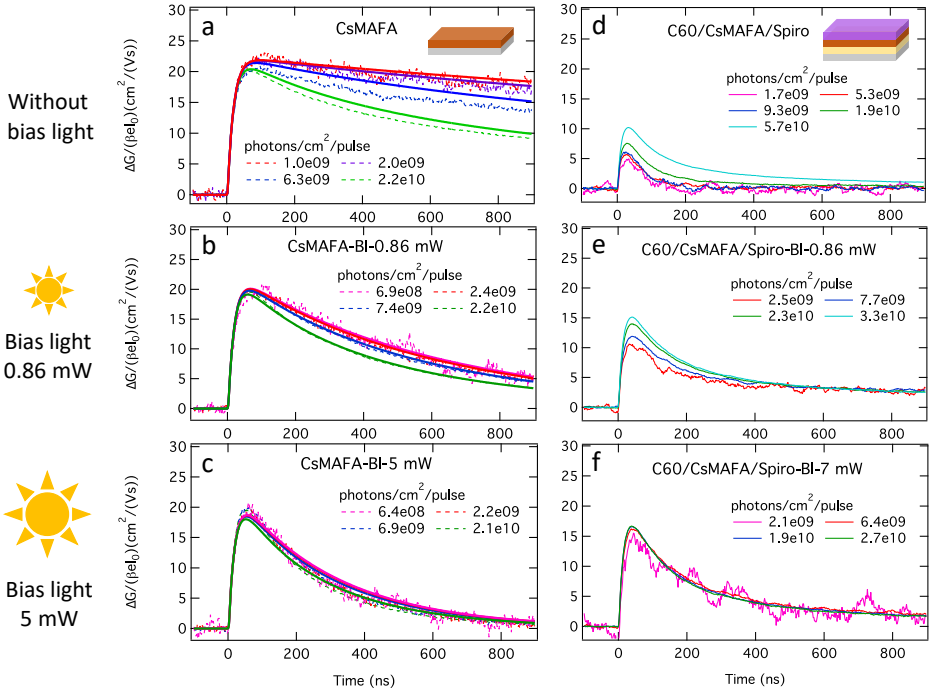

Figure 5.4: TRMC traces recorded in neat CsMAFA (left panels) and C_{60}/CsMAFA/Spiro trilayer (right panels) deposited on quartz (light grey) without BI (a, d), with low-intensity BI (0.86 mW ~ 0.04 sun) (b, e) and high-intensity BI (5 mW ~ 0.24 sun) (c, f). For neat CsMAFA the fits are added to the dashed experimental traces.

In order to validate the above interpretation, we first modeled TRMC traces in bare CsMAFA without BI using the kinetic model shown in Figure 5.3a, which was previously used to describe the photophysical processes in various perovskites.[35,45] This allows us to quantitatively extract the carrier mobilities, trap densities, and recombination rates in CsMAFA. The fits are added to Figure 5.4a with solid lines (see Figure 5A.7a in Appendices for longer timescales) and match the experimental traces well. In Table 5.1 the kinetic parameters are collected. The second-order recombination rate constant (k_2) is around 3.5×10^{-9} cm^3s^{-1}, in line with the reported value for other high-quality perovskite thin films.[47] Furthermore, the trap density (N_T) is 6.5×10^{13} cm^{-3}, which is relatively low for polycrystalline perovskite films. Since the effective masses of electrons and holes are very comparable as shown by density functional theory calculations,[39] we kept the mo-

bilities of electrons and holes identical during the fitting procedure to 14 $cm^2 (Vs)^{-1}$).

Next, to simulate the TRMC traces under BI, we took both the temporal laser pulse and continuous illumination into account (see Note S1 for the used set of differential Equations 5A.1 to 5A.3 in Appendices), using the same kinetic model and the same set of parameters in Table 5.1, as has been done for $MAPbI_3$.[48] The fits were added to the TRMC traces in Figures 5.4b, c (see Figures 5A.7b, c in Appendices for longer timescales), as illustrated by the solid lines, in excellent agreement with the dashed experimental traces. In Figure 5.5, the modeled concentrations of holes, electrons, and trapped electrons for a pulsed laser excitation of $I_0 = 7 \times 10^9$ photons cm^{-2} per pulse (1×10^{14} excitations cm^{-3} per pulse) are shown. Figure 5.5a displays the carrier concentration generated using only the pulsed laser, showing the temporal evolution of the carriers and traps after the pulse. Under a BI of 0.86 mW (Figure 5.5b), the carrier concentrations created by the BI and pulsed laser are rather comparable, which means that their carrier dynamics are affected by both sources. When the BI increases to 5 mW, excess carriers generated by the BI become dominant. Therefore, the carrier decay behavior is governed by the BI, leading to a pseudo-first-order recombination process. In addition, the perfect match of the fits highlights that CsMAFA is stable under the illumination conditions used in this work, without any undesired ion migration or degradation.

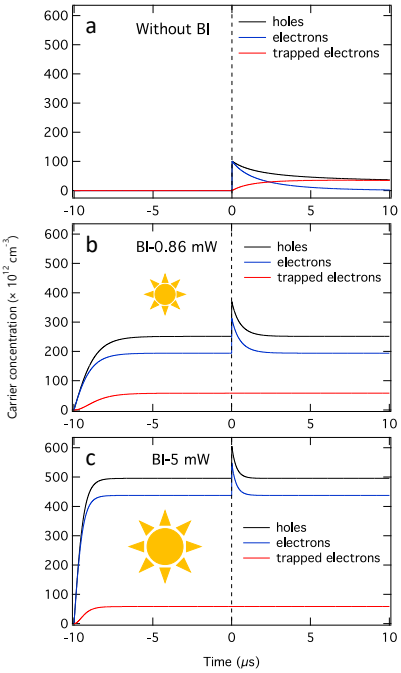

Figure 5.5: Modeling of the charge carrier concentration using the pulsed laser with an incident fluence of 7×10^9 photons cm^{-2} per pulse (a) or a combination of pulsed and biased illumination sources under different BI intensities (b, c) in the neat CsMAFA layer.

To better understand the differences in carrier extraction dynamics between

C_{60}/CsMAFA and CsMAFA/C_{60}, we simulated the TRMC traces in these two bilayers using the same kinetic model but extended it by the introduction of an ETL, to account for the additional charge extraction and recombination pathways, as shown in Figure 5.3a in red. The fits are added as solid lines to the dashed experimental data in Figure 5.2b and Figure 5A.6c in Appendices, respectively. Note that we used the same set of parameters obtained from the fit of neat CsMAFA, leaving only k_{ext} and k_{rec} to vary. The results are added to Table 5.1. The carrier extraction rate, k_{ext}, for both bilayers is found to amount to 6×10^7 s^{-1}, in agreement with previously reported values.[43,48] Interestingly, the recombination time constant, k_{rec} is 10 times larger in CsMAFA/C_{60} than that in C_{60}/CsMAFA, implying much faster interfacial recombination when C_{60} is deposited on top of CsMAFA than vice versa. Therefore, the sequence of deposition seems to be important for the formation of interfacial states between CsMAFA and C_{60}.

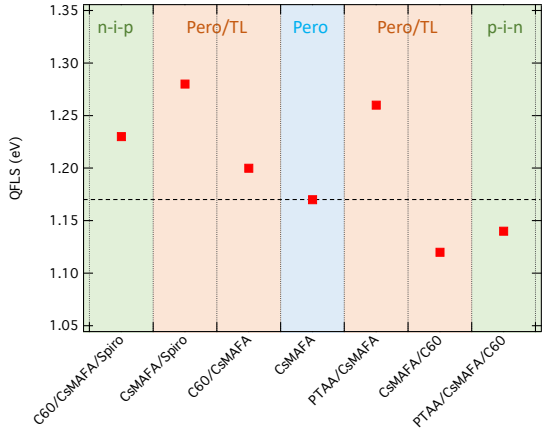

Figure 5.6: The calculated QFLS of the neat CsMAFA layer (blue shade) and combined with hole or electron transport layers (orange shade) as well as the corresponding n-i-p and p-i-n stacks (green shade) derived from the steady-state microwave conductivity measurement.

Finally, we want to see how charge collection and recombination at the interface affect the quasi-Fermi level splitting, which is a measure of the possible attainable V_{OC}. We derived the QFLS from steady-state microwave conductivity measurements under simulated sunlight (see the Experimental methods and Note S3 in the Supporting Information for details). Figure 5.6 shows the measured QFLS for a bare CsMAFA layer and various bi- and triple-layers under AM 1.5 illumination. The QFLS of the neat CsMAFA layer is approximately 1.17 eV, which is close to the previously reported QFLS values derived from the PLQY (~ 1.2 eV) and the VOC obtained on FA-rich PSCs (1.13-1.18 eV).[7,17,18,30] For the CsMAFA/C_{60} showing short-lived charge separation, implying electron collection is followed by rapid interfacial recombination, the corresponding QFLS is reduced with respect to the pristine CsMAFA layer. Most importantly, for the other bilayer combinations including in C_{60}/CsMAFA long-lived charge separation is observed which translates into an increase of the QFLS with respect to the CsMAFA layer. Furthermore, the n-i-p and p-i-n stacks were evaluated. Compared to the n-i-p configuration, the QFLS of the p-i-n

structure is significantly lower, suggesting that again the CsMAFA/C_{60} interface is likely to be the major issue limiting the final V_{OC} of the device. Therefore, the inclusion of an interfacial layer might indeed be important to obtain long-lived charge separation in CsMAFA/C_{60} bilayers.[10] The origin of the losses is not well known and might be due to the deposition conditions used for the C_{60} layer or the impact of the collision of the C_{60} molecules with the perovskite surface. A recent study claimed that this interfacial recombination most likely occurs within the first monolayer of C_{60} at the interface.[20] Future research on fundamental aspects may help to understand more about the origins of these losses.

5.3. Conclusions

In this Chapter, we performed time-resolved microwave photoconductance measurements in single, double, and triple layers comprising a triple-cation lead mixed-halide perovskite absorber layer (CsMAFA), C_{60} as electron TL and Spiro-OMeTAD (n-i-p) or PTAA (p-i-n) as hole TL. From the analysis of the bilayers, charge extraction from CsMAFA to Spiro and PTAA is efficient, demonstrating long-lived charge separation. The recombination in CsMAFA/C_{60} is much faster than in C_{60}/CsMAFA, implying the presence of interfacial trap states when C_{60} is deposited on top of CsMAFA. The sequence of deposition seems to be important for the formation of these interfacial states which should be reduced to increase the Fermi level splitting and subsequently the V_{OC} of a corresponding solar cell. Furthermore, the similar reduction of the TRMC signal in CsMAFA/ETL and CsMAFA/HTL bilayers compared to neat CsMAFA indicates that the mobilities of electrons and holes are balanced in the perovskite. In trilayer systems, a strongly decreased TRMC signal is observed for both n-i-p and p-i-n stacks indicating efficient charge carrier extraction. At higher incident intensities, the charge asymmetry caused by charge extraction leads to an internal electric field, which is opposite to the direction of the charge extraction, increasing the TRMC signal. Applying BI leads to the formation of an equilibrium of electrons and holes in both TLs. Interestingly, recording a TRMC signal results in a much higher signal in the presence of BI than without BI. In fact, with BI, the triple layer resembles the TRMC signal of a bare CsMAFA under the same BI. This provides valuable insight into how charge collection and recombination at the perovskite/TL interfaces affect the performance of PSCs based on FA-rich perovskites.

5.4. Experimental methods

Preparation of transport layers

For the Spiro-OMeTAD layer, a 75 mg mL^{-1} chlorobenzene solution was prepared, which was spin-coated at 1500 rpm for 45 s. The C_{60} layer (30 nm) was thermally evaporated. For the PTAA layer, a 2 mg mL^{-1} PTAA dissolved in chlorobenzene was spin-coated at 6000 rpm for 30 s. After 10 min annealing on a hotplate at 100 °C, the films were cooled down to room temperature. The thickness is about 10 nm referring to the literature.[13]

Steady-state microwave conductance

The steady-state microwave conductance (SSMC) technique was used to examine the background conductivity of perovskite thin films. Here, the reduction in microwave power ($\Delta P(t)/P$) is studied by sweeping the frequency range between 8.2-12.2 GHz. Only frequencies that allow the formation of a standing wave inside the resonance cavity result in the maximum interaction between the sample and the microwaves, thus producing a dominant dip at those frequencies in the SSMC scan. All SSMC measurements were performed in the dark. By using equation 5.1, the depth of the dip in the frequency scan (expressed as $\Delta P(t)/P$) can be related to the conductivity of the sample, in this case, due to the concentration of charge carriers that are present in the dark. In this equation, L accounts for the sample thickness. $\Delta\sigma$ is the difference in conductivity between a quartz reference and the perovskite film, which is also deposited on quartz. Therefore, the conductivity of the perovskite film can be extracted.

$$\frac{\Delta P(t)}{P} = -K\beta L\Delta\sigma \tag{5.1}$$

5

References

[1] S. D. Stranks, G. E. Eperon, G. Grancini, et al. Electron-hole diffusion lengths exceeding 1 micrometer in an organometal trihalide perovskite absorber. *Science* **342** (2013), 341–344.

[2] M. Grätzel. The light and shade of perovskite solar cells. *Nature Materials* **13** (2014), 838–842.

[3] H. Tan, A. Jain, O. Voznyy, et al. Efficient and stable solution-processed planar perovskite solar cells via contact passivation. *Science* **355** (2017), 722–726.

[4] E. M. Tennyson, T. A. Doherty, and S. D. Stranks. Heterogeneity at multiple length scales in halide perovskite semiconductors. *Nature Reviews Materials* **4** (2019), 573–587.

[5] N. G. Park and K. Zhu. Scalable fabrication and coating methods for perovskite solar cells and solar modules. *Nature Reviews Materials* **5** (2020), 333–350.

[6] NREL. *Best Research-Cell Efficiencies: Rev. October 2023*. 2023.

[7] G. Li, Z. Su, L. Canil, et al. Highly efficient p-i-n perovskite solar cells that endure temperature variations. *Science* **379** (2023), 399–403.

[8] H. Chen, A. Maxwell, C. Li, et al. Regulating surface potential maximizes voltage in all-perovskite tandems. *Nature* **613** (2023), 676–681.

[9] R. Gottesman, P. Lopez-Varo, L. Gouda, et al. Dynamic Phenomena at Perovskite/Electron-Selective Contact Interface as Interpreted from Photovoltage Decays. *Chem* **1** (2016), 776–789.

[10] S. Mariotti, E. Köhnen, F. Scheler, et al. Interface engineering for high-performance, triple-halide perovskite-silicon tandem solar cells. *Science* **381** (2023), 63–69.

[11] H. Zhu, Y. Liu, F. T. Eickemeyer, et al. Tailored Amphiphilic Molecular Mitigators for Stable Perovskite Solar Cells with 23.5% Efficiency. *Advanced Materials* **32** (2020), 1–8.

[12] C. M. Wolff, P. Caprioglio, M. Stolterfoht, and D. Neher. Nonradiative Recombination in Perovskite Solar Cells: The Role of Interfaces. *Advanced Materials* **31** (2019).

[13] Z. Li, B. Li, X. Wu, et al. Organometallic-functionalized interfaces for highly efficient inverted perovskite solar cells. *Science* **376** (2022), 416–420.

[14] G. Fu, D.-k. Lee, and N.-g. Park. Disulfidation Interfacial Engineering toward Stable, Lead-Immobilizable Perovskite Solar Cells. *ACS Energy Letters* **8** (2023), 4563–4571.

[15] Y. Li, H. Xie, E. L. Lim, A. Hagfeldt, and D. Bi. Recent Progress of Critical Interface Engineering for Highly Efficient and Stable Perovskite Solar Cells. *Advanced Energy Materials* **12** (2022), 1–31.

[16] D. Guo, V. M. Caselli, E. M. Hutter, and T. J. Savenije. Comparing the calculated fermi level splitting with the open-circuit voltage in various perovskite cells. *ACS Energy Letters* **4** (2019), 855–860.

[17] M. Stolterfoht, P. Caprioglio, C. M. Wolff, et al. The impact of energy alignment and interfacial recombination on the internal and external open-circuit voltage of perovskite solar cells. *Energy and Environmental Science* **12** (2019), 2778–2788.

[18] P. Caprioglio, M. Stolterfoht, C. M. Wolff, et al. On the Relation between the Open-Circuit Voltage and Quasi-Fermi Level Splitting in Efficient Perovskite Solar Cells. *Advanced Energy Materials* **9** (2019).

[19] J. Haddad, B. Krogmeier, B. Klingebiel, et al. Analyzing Interface Recombination in Lead-Halide Perovskite Solar Cells with Organic and Inorganic Hole-Transport Layers. *Advanced Materials Interfaces* **7** (2020).

[20] J. Warby, F. Zu, S. Zeiske, et al. Understanding Performance Limiting Interfacial Recombination in pin Perovskite Solar Cells. *Advanced Energy Materials* **12** (2022), 1–10.

[21] E. Serpetzoglou, I. Konidakis, G. Kakavelakis, et al. Improved Carrier Transport in Perovskite Solar Cells Probed by Femtosecond Transient Absorption Spectroscopy. *ACS Applied Materials and Interfaces* **9** (2017), 43910–43919.

[22] J. I. Khan, F. H. Isikgor, E. Ugur, et al. Charge Carrier Recombination at Perovskite/Hole Transport Layer Interfaces Monitored by Time-Resolved Spectroscopy. *ACS Energy Letters* **6** (2021), 4155–4164.

[23] E. Ugur, J. I. Khan, E. Aydin, et al. Carrier Extraction from Perovskite to Polymeric Charge Transport Layers Probed by Ultrafast Transient Absorption Spectroscopy. *Journal of Physical Chemistry Letters* **10** (2019), 6921–6928.

[24] V. M. Le Corre, M. Stolterfoht, L. Perdigón Toro, et al. Charge Transport Layers Limiting the Efficiency of Perovskite Solar Cells: How to Optimize Conductivity, Doping, and Thickness. *ACS Applied Energy Materials* **2** (2019), 6280–6287.

[25] S. Ravishankar, S. Gharibzadeh, C. Roldán-Carmona, et al. Influence of Charge Transport Layers on Open-Circuit Voltage and Hysteresis in Perovskite Solar Cells. *Joule* **2** (2018), 788–798.

[26] E. M. Hutter, T. Kirchartz, B. Ehrler, D. Cahen, and E. Von Hauff. Pitfalls and prospects of optical spectroscopy to characterize perovskite-transport layer interfaces. *Applied Physics Letters* **116** (2020).

[27] J. Bisquert and M. Janssen. From Frequency Domain to Time Transient Methods for Halide Perovskite Solar Cells: The Connections of IMPS, IMVS, TPC, and TPV. *Journal of Physical Chemistry Letters* **12** (2021), 7964–7971.

[28] J. Bisquert. Interpretation of the Recombination Lifetime in Halide Perovskite Devices by Correlated Techniques. *Journal of Physical Chemistry Letters* **13** (2022), 7320–7335.

[29] P. Lopez-Varo, J. A. Jiménez-Tejada, M. García-Rosell, et al. Effects of Ion Distributions on Charge Collection in Perovskite Solar Cells. *ACS Energy Letters* **2** (2017), 1450–1453.

[30] S. You, H. Zeng, Y. Liu, et al. Radical polymeric p-doping and grain modulation for stable, efficient perovskite solar modules. *Science* **379** (2023), 288–294.

[31] C. C. Stoumpos, C. D. Malliakas, and M. G. Kanatzidis. Semiconducting tin and lead iodide perovskites with organic cations: Phase transitions, high mobilities, and near-infrared photoluminescent properties. *Inorganic Chemistry* **52** (2013), 9019–9038.

[32] D. H. Fabini, C. C. Stoumpos, G. Laurita, et al. Reentrant Structural and Optical Properties and Large Positive Thermal Expansion in Perovskite Formamidinium Lead Iodide. *Angewandte Chemie* **128** (2016), 15618–15622.

[33] L. Chen, Y. Y. Tan, Z. X. Chen, et al. Toward Long-Term Stability: Single-Crystal Alloys of Cesium-Containing Mixed Cation and Mixed Halide Perovskite. *Journal of the American Chemical Society* **141** (2019), 1665–1671.

[34] E. M. Hutter, R. J. Sutton, S. Chandrashekar, et al. Vapour-Deposited Cesium Lead Iodide Perovskites: Microsecond Charge Carrier Lifetimes and Enhanced Photovoltaic Performance. *ACS Energy Letters* **2** (2017), 1901–1908.

[35] D. Guo, Z. Andaji Garmaroudi, M. Abdi-Jalebi, S. D. Stranks, and T. J. Savenije. Reversible Removal of Intermixed Shallow States by Light Soaking in Multication Mixed Halide Perovskite Films. *ACS Energy Letters* **4** (2019), 2360–2367.

[36] T. J. Savenije, D. Guo, V. M. Caselli, and E. M. Hutter. Quantifying Charge-Carrier Mobilities and Recombination Rates in Metal Halide Perovskites from Time-Resolved Microwave Photoconductivity Measurements. *Advanced Energy Materials* **10** (2020), 1–12.

[37] J. Zhao, V. M. Caselli, M. Bus, B. Boshuizen, and T. J. Savenije. How Deep Hole Traps Affect the Charge Dynamics and Collection in Bare and Bilayers of Methylammonium Lead Bromide. *ACS Applied Materials and Interfaces* **13** (2021), 16309–16316.

[38] F. Ruf, M. F. Aygüler, N. Giesbrecht, et al. Temperature-dependent studies of exciton binding energy and phase-transition suppression in (Cs,FA,MA)Pb(I,Br)3 perovskites. *APL Materials* **7** (2019).

[39] K. Galkowski, A. Mitioglu, A. Miyata, et al. Determination of the exciton binding energy and effective masses for methylammonium and formamidinium lead trihalide perovskite semiconductors. *Energy and Environmental Science* **9** (2016), 962–970.

[40] C. L. Davies, J. Borchert, C. Q. Xia, et al. Impact of the Organic Cation on the Optoelectronic Properties of Formamidinium Lead Triiodide. *Journal of Physical Chemistry Letters* **9** (2018), 4502–4511.

[41] P. Umari, E. Mosconi, and F. De Angelis. Infrared Dielectric Screening Determines the Low Exciton Binding Energy of Metal-Halide Perovskites. *Journal of Physical Chemistry Letters* **9** (2018), 620–627.

[42] M. Baranowski and P. Plochocka. Excitons in Metal-Halide Perovskites. *Advanced Energy Materials* **10** (2020).

[43] E. M. Hutter, J. J. Hofman, M. L. Petrus, et al. Charge Transfer from Methylammonium Lead Iodide Perovskite to Organic Transport Materials: Efficiencies, Transfer Rates, and Interfacial Recombination. *Advanced Energy Materials* **7** (2017), 1–8.

[44] V. M. Caselli, Z. Wei, M. M. Ackermans, et al. Charge Carrier Dynamics upon Subbandgap Excitation in Methylammonium Lead Iodide Thin Films: Effects of Urbach Tail, Deep Defects, and Two-Photon Absorption. *ACS Energy Letters* **5** (2020), 3821–3827.

[45] E. M. Hutter, G. E. Eperon, S. D. Stranks, and T. J. Savenije. Charge Carriers in Planar and Meso-Structured Organic-Inorganic Perovskites: Mobilities, Lifetimes, and Concentrations of Trap States. *Journal of Physical Chemistry Letters* **6** (2015), 3082–3090.

[46] A. Al-Ashouri, E. Köhnen, B. Li, et al. Monolithic perovskite/silicon tandem solar cell with >29% efficiency by enhanced hole extraction. *Science* **370** (2020), 1300–1309.

[47] C. L. Davies, M. R. Filip, J. B. Patel, et al. Bimolecular recombination in methylammonium lead triiodide perovskite is an inverse absorption process. *Nature Communications* **9** (2018), 1–9.

[48] V. M. Caselli and T. J. Savenije. Quantifying Charge Carrier Recombination Losses in MAPbI3/C60 and MAPbI3/Spiro-OMeTAD with and without Bias Illumination. *Journal of Physical Chemistry Letters* **13** (2022), 7523–7531.

Appendices

5.A. Appendices

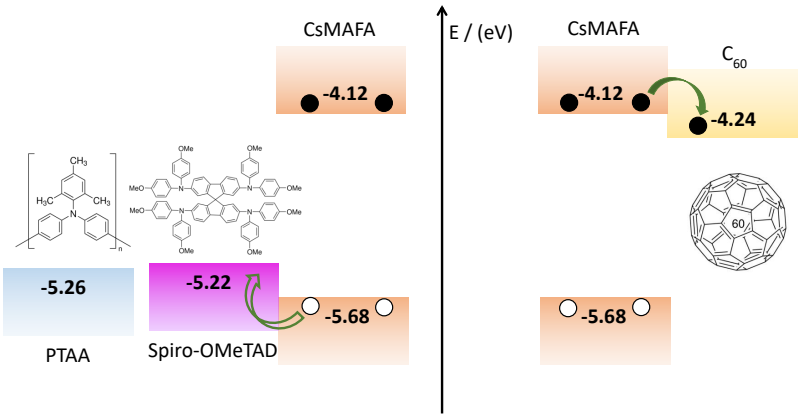

Figure 5A.1: Energy band diagrams and molecular structures of CsMAFA and different transport materials.

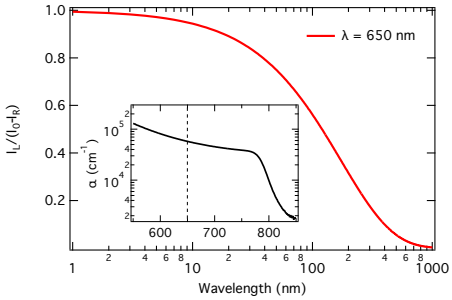

Figure 5A.2: Initial charge carrier generation profile for excitation at 650 nm using the absorption coefficient 5.77×10^4 cm^{-1} for 650 nm as shown in the inset.

Note S1 TRMC fitting differential equations

$$\frac{dn_e}{dt} = G_C - k_2\left(n_h + p_0\right)n_e - k_T\left(N_T - n_t\right)n_e - k_{ext}n_e \tag{5A.1}$$

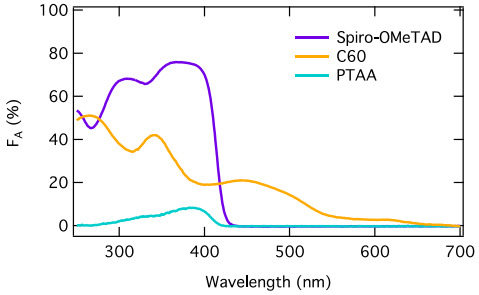

Figure 5A.3: Optical absorption spectra of Spiro-OMeTAD, C_{60}, and PTAA layers deposited on quartz.

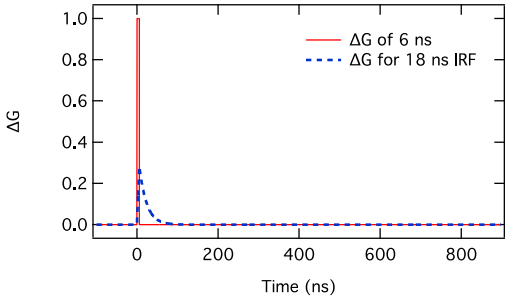

Figure 5A.4: The effect of the instrumental response function (IRF) on the cavity with a response time of 18 ns for a ΔG of 6 ns.

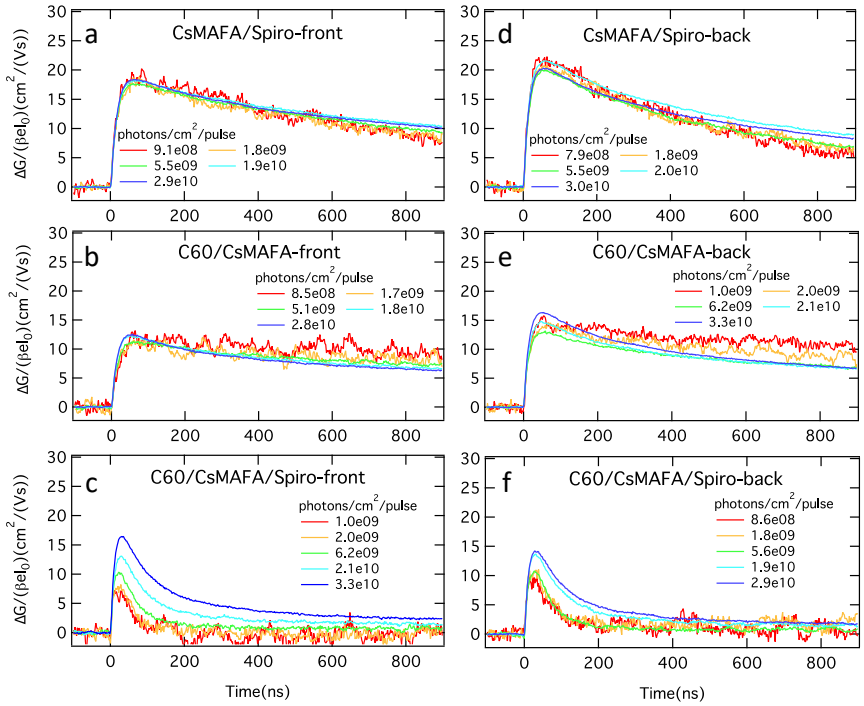

Figure 5A.5: TRMC traces for CsMAFA/Spiro (a, d), C_{60}/CsMAFA (b, e), and C_{60}/CsMAFA/Spiro (c, f) recorded on the front (left panels) and back (right panels) excitation at 650 nm with incident light intensities ranging from $10^8 - 10^{10}$ photons cm^{-2} per pulse.

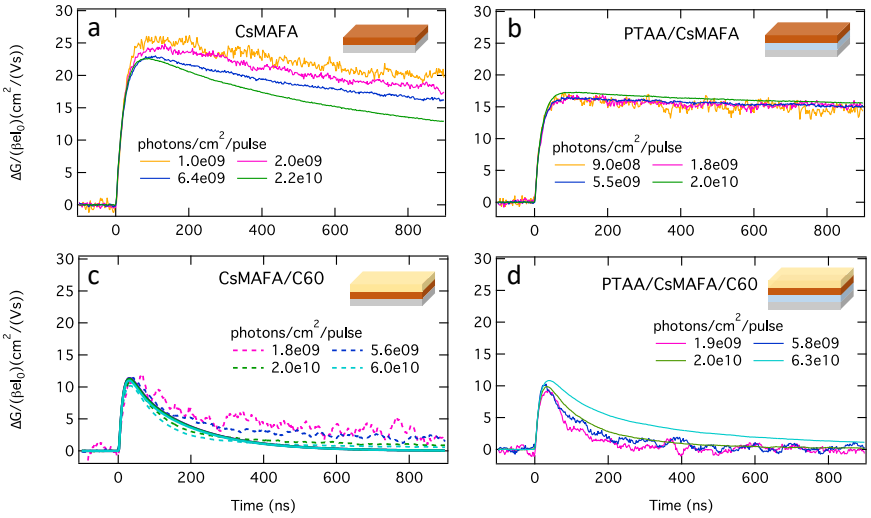

Figure 5A.6: TRMC traces for CsMAFA (a), PTAA/CsMAFA (b), CsMAFA/C_{60} (c), and PTAA/CsMAFA/C_{60}, (d) deposited on quartz (light grey) recorded on excitation at 650 nm with incident light intensities ranging from $10^9 - 10^{10}$ photons cm^{-2} per pulse. The fits for the CsMAFA/C_{60} bilayer are indicated by the solid lines.

$$\frac{-dn_h}{dt} = -G_C + k_2\left(n_h + p_0\right)n_e + k_D n_t\left(n_h + p_0\right) - k_{rec}n_h \tag{5A.2}$$

$$\frac{dn_t}{dt} = k_T\left(N_T - n_t\right)n_e - k_D n_t\left(n_h + p_0\right) \tag{5A.3}$$

$$\frac{dn_{ETL}}{dt} = k_{ext}n_e - k_{rec}n_h \tag{5A.4}$$

Note S2 Quasi-Fermi level splitting determination

The quasi-Fermi level splitting (QFLS) at AM 1.5 was determined by steady-state microwave conductivity measurements using a monochromatic LED (λ = 522 nm) to photogenerated excess charges. The LED light intensity corresponding to AM 1.5 was determined by integrating the solar spectrum down to an energy of 1.55 eV, corresponding to the bandgap of CsMAFA yielding 2×10^{17} photons s^{-1} cm^{-2}. The LED intensity (measured in mW cm^{-2}) was set to this fluence using an optical sensor, resulting in an intensity of 75 mW cm^{-2}). The LED light was modulated to a frequency of 0.5 Hz using a function generator. The change in voltage (ΔV) between dark and light over the microwave detector was probed by a lock-in amplifier.

The QFLS can be calculated using:

$$QFLS = \frac{k_B T}{q} ln\left(\frac{\left(n_0 + \Delta n\right)\left(p_0 + \Delta p\right)}{{n_i}^2}\right) \tag{5A.5}$$

Where the $(k_B T)/q$ is the thermal voltage, n_i represents the intrinsic carrier concentration and has been evaluated around 1×10^6 cm^{-3} for triple cation CsMAFA. n_0 and p_0

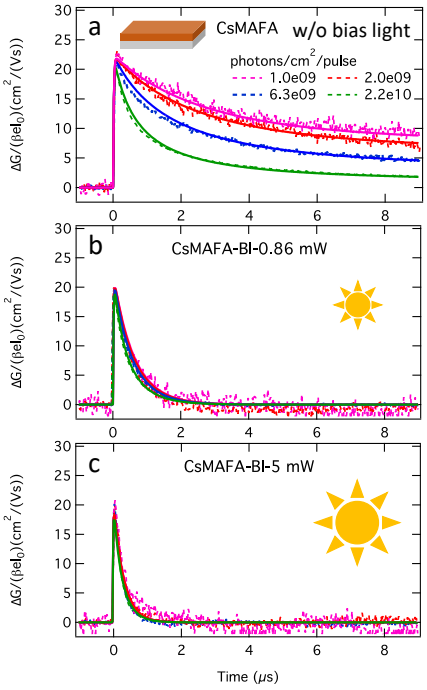

Figure 5A.7: TRMC traces in neat CsMAFA deposited on quartz (light grey) without (a) and with bias illumination under 0.86 mW (~ 0.04 sun) (b) and 5 mW (~ 0.3 sun) (c) on longer time scales. The fits are added to the dashed experimental traces.

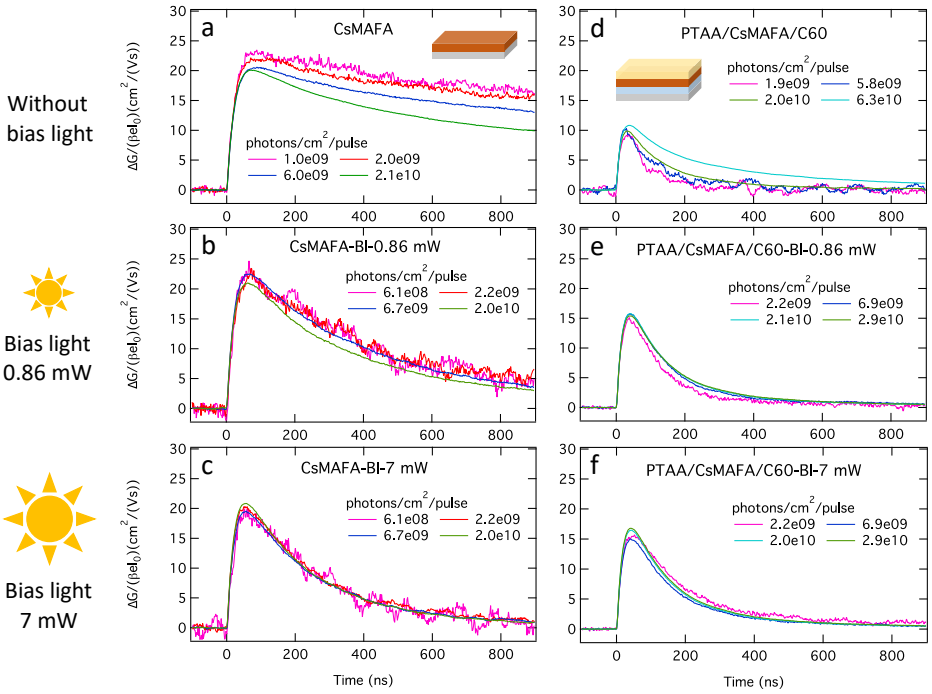

Figure 5A.8: TRMC traces in neat CsMAFA (left panels) and PTAA/CsMAFA/C_{60} trilayer (right panels) without (a, d) and with bias illumination under 0.86 mW (b, e) and 7 mW (c, f). The fits are added to the dashed experimental traces for neat CsMAFA.

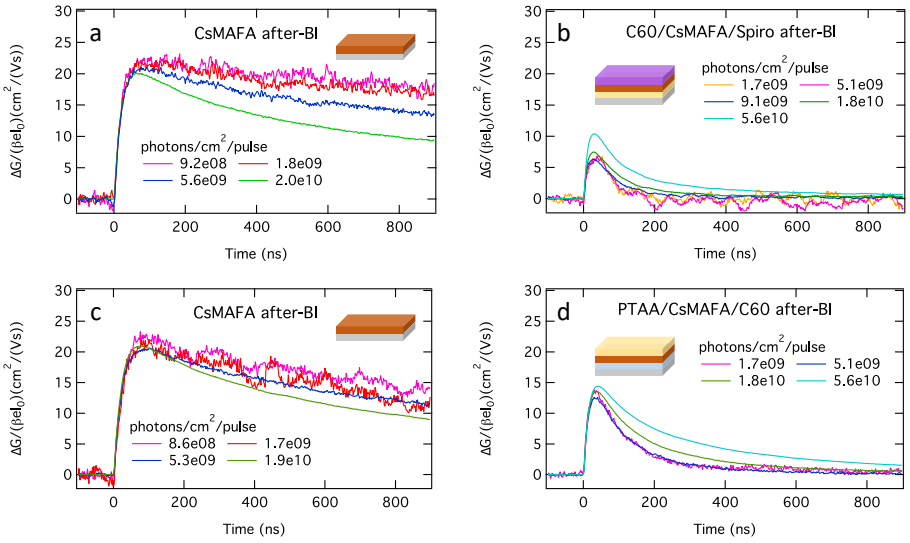

Figure 5A.9: TRMC traces for bare CsMAFA (a, c), C_{60}/CsMAFA/Spiro (b), and PTAA/CsMAFA/C_{60} (d) trilayers recorded after bias illumination on pulsed excitation at 650 nm with incident light intensities ranging from $10^8 - 10^{10}$ photons cm^{-2} per pulse.

are thermal equilibrium concentrations of electrons and holes, respectively. While Δn, Δp are photoexcited excess charge carrier concentrations. According to our simulated TRMC results on CsMAFA, p_0 is in the order of 10^{12} cm^{-3}, which is almost three orders of magnitude smaller than that of Δn and Δp under AM 1.5, which is in the order of 10^{15} cm^{-3}. Besides, since each photon results in the generation of one mobile electron and one mobile hole, we take Δn to be equal to Δp. Therefore, equation 5A.5 can be simplified as follows:

$$QFLS = \frac{k_B T}{q} ln\left(\frac{\Delta n^2}{{n_i}^2}\right) \tag{5A.6}$$

The change in conductivity ($\Delta\sigma$) is calculated from ΔV that was measured by the lock-in, together with the cell voltage (V_{cell}), n factor (n) and predetermined sensitivity factor K using equation 5A.7. The $\Delta\sigma$ is related to Δn by equation 5A.8, where e is the elementary charge and $\Sigma\mu$ is the sum of the mobilities of electrons and holes which can be extracted from the recorded TRMC signals.

$$n\frac{\Delta V}{V_{cell}} = \frac{\Delta P}{P} = -K\Delta\sigma\beta L \tag{5A.7}$$

$$\Delta\sigma = e\Delta n\Sigma\mu \tag{5A.8}$$

Summary

As one of the fastest-growing renewable energy technologies, photovoltaics play an increasingly important role in the global energy transition. Over the past decade, metal halide perovskite solar cells (PSCs) have emerged as the most promising candidates for next-generation solar cells, with a certified power conversion efficiency of 26.1% for single-junction cells. Despite these significant advances in this performance, understanding the fundamental optoelectronic properties of various compositions is crucial to improve the efficiency and stability of the development of single-junction and multi-junction solar cells, including perovskite/silicon and all-perovskite tandem solar cells. In this thesis, we have investigated the generation, recombination, and extraction of photo-generated carriers in various metal halide perovskites (MHPs) in combination with selective transport layers (TLs) mainly using the time-resolved microwave conductivity (TRMC) technique. Moreover, structural properties were revealed using various techniques including XRD, XPS, and SEM. In addition, different deposition methods of perovskite thin films are studied with the aim of providing insights into the relationship between structure and optoelectronic properties.

In Chapter 2, we have studied the carrier decay dynamics in the wide-bandgap perovskite $MAPbBr_3$ prepared by one-step spin-coating, which has great potential to be used as the top cell in tandem solar cells. We observe that the concentration of trap states in $MAPbBr_3$ exceeds $10^{16}cm^{-3}$, which is an order of magnitude higher than that in $MAPbI_3$. This finding explains the larger voltage deficit between E_g/e and V_{OC} for bromide-containing perovskites compared to their pure iodide counterparts. More importantly, the introduction of the additive, hypophosphorous acid (HPA), reduces the trap states that are most likely to reside at grain boundaries. Furthermore, by applying an electron or a hole TL on top of the perovskite layer, we find that hole trap states dominate in $MAPbBr_3$.

In Chapter 3, we have investigated the optoelectronic properties of co-evaporated $MAPbI_3$, since thermal evaporation is particularly beneficial for integrating perovskite devices with silicon into tandem solar cells and for the scalability of large-area PSCs. We find that co-evaporated $MAPbI_3$ films exhibit a gradient in composition due to changes in the evaporation rate of each precursor during the co-evaporation process. We observe that an MAI deficiency is predominantly located at the top part of the $MAPbI_3$ films, resulting in local n-doping. Therefore, an internal electric field is formed in $MAPbI_3$ due to the presence of different n-doped regions across the $MAPbI_3$ films. Moreover, we test the power conversion efficiency of corresponding devices using the same co-evaporated $MAPbI_3$ layers in n-i-p and p-i-n configurations. It turns out that the performance of PSCs in p-i-n architecture is better than that in n-i-p structure, demonstrating that the internal electric field is only beneficial for p-i-n PSCs because it is expected that the energy alignment improves the charge carrier collection.

Chapters 4 and 5 focus on the state-of-the-art triple-cation lead mixed halide per-

ovskites prepared by the antisolvent method, which have been extensively studied in PSCs, showing very promising performance and stability. In Chapter 4, we perform an in-depth fundamental investigation of how the phase behavior affects the optoelectronic properties in $Cs_{0.05}MA_{0.10}FA_{0.85}Pb(I_{0.97}Br_{0.03})_3$ (CsMAFA) films with 5% excess PbI_2. First of all, XRD refinement reveals that CsMAFA undergoes an $\alpha - \beta$ phase transition at ~ 280 K and another transition to the γ-phase at ~ 180 K. Through extensive analyses of our TRMC data, we find that shallow traps are harmless in the α-phase, but negatively affect the charge carrier dynamics in the γ-phase. Most importantly, we reveal that CsMAFA exhibits the lowest trap density in the β-phase, which is associated with the lowest microstrain we derived from the XRD patterns at around 240 K. Below 200 K we find a considerable increase in trap states, most likely related to the temperature-induced compressive microstrain. Finally, based on the ingrowth TRMC signal in stoichiometric CsMAFA at 130 K, we conclude that excess PbI_2 retards the phase retention from β- to γ-phase, as the PbI_2 at the interface alleviates the mismatch between the expansion coefficients of quartz and CsMAFA.

To improve the open-circuit voltage in PSCs based on these CsMAFAs, reducing recombination processes at the interfaces with TLs is key. In Chapter 5, we examine the charge carrier dynamics in neat CsMAFA in combination with hole and electron TLs in n-i-p and p-i-n stacks without and with bias illumination (BI). In the bilayers, we find almost balanced mobilities for electrons and holes in CsMAFA and nearly quantitative carrier extraction. For the triple layers, based on the small, rapidly decaying TRMC signal, both carriers are extracted at low laser intensities independent of the configuration. By applying BI, we observe that charge extraction is retarded and the resulting TRMC signal is much higher in comparison to the situation without BI. We explain these observations to the charging of both TLs under BI, resulting in an internal electric field that inhibits further charge collection. Most importantly, for all bilayer combinations showing long-lived charge separation, an increase of the quasi-Fermi level splitting with respect to that of the CsMAFA layer is found.

In the end, this thesis mainly uses the TRMC technique to systematically study the charge carrier dynamics of perovskite thin films with a variety of compositions prepared by spin-coating or thermal evaporation methods. Chapter 2 reveals how the introduction of HPA additives in $MAPbBr_3$ improves the morphology, thereby reducing the trap density and enhancing optoelectronic properties. Chapter 3 demonstrates that asymmetry in co-evaporated $MAPbI_3$ perovskite films ultimately influences the performance of PSCs, depending on the device configuration. The low temperature-dependent measurements in CsMAFA in Chapter 4 highlight the importance of diminishing microstrain in perovskite films to further boost their efficiency. Chapter 5 shows that contactless TRMC measurements in n-i-p and p-i-n stacks combined with quasi-Fermi level splitting predictions in CsMAFA are powerful tools for pinpointing the interfacial issues of the most concerned in the corresponding PSCs.

Samenvatting

Als een van de snelst groeiende technologieën voor hernieuwbare energie speelt fotovoltaïsche zonne-energie een steeds belangrijkere rol in de mondiale energietransitie. De afgelopen tien jaar zijn metaalhalide-perovskiet-zonnecellen (PSCs) de meest veelbelovende kandidaten gebleken voor de volgende generatie zonnecellen, met een gecertificeerde energieconversie-efficiëntie van 26.1% voor cellen gebaseerd op een enkele licht absorberende laag. Ondanks deze aanzienlijke vooruitgang is het begrijpen van de fundamentele opto-elektronische eigenschappen van verschillende perovskiet samenstellingen cruciaal voor het verbeteren van de efficiëntie en stabiliteit voor de ontwikkeling van zonnecellen met één en meerdere juncties, waaronder perovskiet/silicium- en volledige perovskiet-tandemzonnecellen. In dit proefschrift hebben we de generatie, recombinatie en extractie van licht-geïnduceerde ladingsdragers in verschillende metaal halogenide perovskieten (MHPs) onderzocht in combinatie met selectieve transportlagen, voornamelijk met behulp van de tijdsopgeloste microgolfgeleidingstechniek (TRMC). Bovendien werden structurele eigenschappen onthuld met behulp van verschillende technieken, waaronder XRD, XPS en SEM. Daarnaast zijn verschillende depositiemethoden voor het maken van dunne MHP films bestudeerd met als doel inzicht te krijgen in de relatie tussen de structuur en de opto-elektronische eigenschappen.

In Hoofdstuk 2 hebben we de dynamiek van de ladingsdragers bestudeerd in een MHP met brede bandafstand, namelijk $MAPbBr_3$, die is vervaardigd door middel van een eenstap-spincoating proces en die een grote potentie heeft om te worden gebruikt in de topcel in tandemzonnecellen. We laten zien dat de concentratie van traptoestanden in $MAPbBr_3$ groter is dan $10^{16}cm^{-3}$, wat een orde van grootte hoger is dan die in $MAPbI_3$. Deze observatie verklaart de groter potentiaalkloof tussen E_g/e en V_{OC} voor bromide houdende perovskieten vergeleken met hun zuivere jodide-tegenhangers. Belangrijker nog is dat de introductie van het additief, hypofosforzuur (HPA), de concentratie defect toestanden vermindert die zich waarschijnlijk bevinden aan de korrelgrenzen. Bovendien zagen we dat, door het aanbrengen van een elektronen- of een gaten-transportlaag boven op de MHP, dat defecten voor gaten domineren in $MAPbBr_3$.

In Hoofdstuk 3 hebben we de opto-elektronische eigenschappen van opgedampt $MAPbI_3$ onderzocht. Thermische verdamping is bijzonder interessant voor de integratie van perovskieten en silicium in tandemzonnecellen omdat deze techniek schaalbaar is naar grotere oppervlakken. We vinden dat opgedampte $MAPbI_3$ films een gradiënt in samenstelling vertonen als gevolg van veranderingen in de verdampingssnelheid van elke precursor tijdens het co-depositie proces. We zien dat er een MAI-deficiëntie in het bovenste deel van de $MAPbI_3$ films is, wat resulteert in lokale n-doping. Vanwege de aanwezigheid van verschillende n-gedoteerde gebieden in de $MAPbI_3$ films wordt er een intern elektrisch veld gevormd in deze $MAPbI_3$ laag. Bovendien testen we de energieconversie-efficiëntie van overeenkomstige zonnecellen met behulp van dezelfde opgedampte $MAPbI_3$-lagen in n-i-p- en p-i-n-configuraties. Het blijkt dat de efficiënties

van PSCs met een p-i-n-architectuur beter zijn dan die in n-i-p-structuur, wat aantoont dat het interne elektrische veld alleen gunstig is voor p-i-n PSCs omdat alleen in deze configuratie de ladingsdragers collectie verbetert.

Hoofdstukken 4 en 5 richten zich op de state-of-the-art drievoudige-kation-loodhalide-perovskieten, geprepareerd met de antisolvent-methode, die uitgebreid zijn bestudeerd in PSCs en veelbelovende prestaties en stabiliteiten laten zien. In Hoofdstuk 4 is een uitgebreid fundamenteel onderzoek uitgevoerd naar hoe het fasegedrag de optoelektronische eigenschappen in $Cs_{0.05}MA_{0.10}FA_{0.85}Pb(I_{0.97}Br_{0.03})_3$ (CsMAFA) films met 5% overmaat PbI_2 beïnvloedt. Allereerst toont XRD-analyse dat CsMAFA een $\alpha - \beta$-faseovergang ondergaat bij ~ 280 K en een andere overgang naar de γ-fase bij ~ 180 K. Door uitgebreide analyses van TRMC-gegevens ontdekken we dat ondiepe defecten onschadelijk zijn in de α-fase, maar een negatieve invloed hebben op de ladingsdrager dynamica in de γ-fase. Het allerbelangrijkste is dat we laten zien dat CsMAFA de laagste trapdichtheid heeft in de β-fase, wat gerelateerd is met de minste microspanning die bereikt wordt rond 240 K. Onder de 200 K vinden we een aanzienlijke toename in diepe defect toestanden, hoogstwaarschijnlijk gerelateerd aan de temperatuur geïnduceerde compressieve microspanning. Ten slotte concluderen we op basis van het ingroeide TRMC-signaal in stoichiometrisch CsMAFA bij 130 K dat overtollig PbI_2 de faseovergang van de β- naar de γ-fase vertraagt, omdat het PbI_2 op het grensvlak het verschil tussen de uitzettingscoëfficiënten van kwarts en CsMAFA beperkt.

Om de open klemspanning in PSCs op basis van deze CsMAFAs te verbeteren, is het verminderen van recombinatieprocessen aan de grensvlakken met de transportlagen van cruciaal belang. In Hoofdstuk 5 hebben we de ladingsdragerdynamiek in zuivere CsMAFA onderzocht in combinatie met gaten- en elektronen-transportlagen in een n-i-p- en een p-i-n-configuratie zonder en met bias-belichting (BB). Uit TRMC metingen aan de dubbellagen vinden we bijna vergelijkbare mobiliteiten voor elektronen en gaten en bijna kwantitatieve ladingsdrager extractie. In de n-i-p en p-i-n triple lagen, worden beide ladingsdragers efficiënt gecollecteerd bij lage laserintensiteiten, op basis van het kleine, snel afnemende TRMC-signaal. Door BB toe te passen, zien we echter dat de ladingsextractie vermindert en dat het resulterende TRMC-signaal veel hoger is in vergelijking met de situatie zonder BB. We verklaren deze waarnemingen op basis van het feit dat onder BB ladingen in beide transportlagen leiden tot een intern elektrisch veld, wat de collectie van nog meer ladingen tegenwerkt. Het belangrijkste is dat voor alle configuraties die een langdurige ladingsscheiding vertonen, een toename van de quasi-Fermi-niveausplitsing ten opzichte van die van de CsMAFA-laag wordt gevonden. Dit wordt verklaard doordat de perovskiet oppervlakte wordt gepassiveerd door het aanbrengen van de transport laag.

Uiteindelijk maakt dit proefschrift voornamelijk gebruik van de TRMC-techniek om systematisch de ladingsdrager dynamica in dunne perovskiet films te bestuderen met verschillende samenstellingen, gemaakt door middel van spin-coating of thermische depositie. Hoofdstuk 2 laat zien hoe de introductie van HPA-additieven aan $MAPbBr_3$ de morfologie verbetert, waardoor de defect dichtheid wordt verminderd en de optoelektronische eigenschappen worden verbeterd. Hoofdstuk 3 laat zien dat, afhankelijk van de configuratie van de lagen, de asymmetrie in opgedampte $MAPbI_3$ perovskiet films uiteindelijk de efficiënties van PSCs beïnvloedt. De temperatuurafhankelijke metingen

aan CsMAFA beschreven in Hoofdstuk 4 benadrukken het belang van het verminderen van de microspanning in perovskiet films om hun efficiëntie verder te vergroten. Hoofdstuk 5 laat zien dat contactloze TRMC-metingen aan n-i-p- en p-i-n-triple lagen, gecombineerd met het bepalen van de splitsing in quasi-Fermi niveaus in CsMAFA, kan helpen bij het opsporen van problemen aan het grensvlak van perovskiet en de transportlagen.

Acknowledgements

When we were little kids, our teachers always asked, "What do you want to be when you grow up?" I said I wanted to become a scientist, but I bet I had no idea what a scientist meant at that time. In the mysterious workings of the universe, there seems a divine will. Twenty years later, I graduated with a PhD in chemistry. Instead, I realized completing a PhD is the end of a student career, but probably just the beginning of a scientist. Looking back over the past twenty years, I want to thank many people who have inspired and influenced me. But here I would like to especially thank the people who were involved during my PhD.

Tom, I remember when I was looking for a CSC-funded PhD position five years ago, you were the first professor I contacted because I had read your papers and was interested in your work. After the interview, you decided to go ahead with supporting my application for CSC. Eventually, I got the scholarship and came to Delft. Four years later, it turns out that I am so lucky to have you as my PhD supervisor. You have the ability to supervise each student according to their individuality and also tailor your supervision at each stage of a PhD. I am grateful that you spent so much time on monitoring and guiding me step by step at the early days of my PhD, allowing me to enter my research path faster and more smoothly. For example, when I was new to TRMC, you would always knock on the door of the TRMC lab to check if everything was ok and have a chat. Later, when I "grew up", you also gave me enough freedom to lead my research and helped me when I needed. I enjoyed the numerous meetings and discussions we had and also learned a lot from you, not only about the research itself, but also about the way you supervise students. Although my PhD has been completed, I hope we will still find opportunities to collaborate in the future.

Arjan, I admire the way you speak, you can talk openly, confidently, and straightforwardly, expressing your thoughts or opinions in a clear and articulate manner. I appreciate all your comments and suggestions on my work during our OM group meetings. On the other hand, I also felt a bit regrettable we could have had more individual meetings if I had taken the opportunity to talk to you often. **Ferdinand**, I did like and thoroughly enjoyed your course "Scientific Writing and Argumentation". Thank you for all your insights and critical thinking on my work. **Laurens**, I would like to thank you for the questions you brought up during my talk that made me think more.

My former students **Menke, Verena, Reinder, Jakob, Sander**, it has been a pleasure working with you and learning from each other. Thank you all for your contribution to my thesis and work during my PhD.

What I like most about our OM group is our technicians, **Ruben, Wiel, Jos, Bahiya**. I would like to thank you all for your training and your tremendous help when problem arose in the lab. Without you, I would not been able to complete my PhD smoothly. Moreover, the technicians from our department, **Xiaohui, Bart, Marcel, Duco**. Thank you all for your help and patience when I asked questions. Our secretary, **Adinda**, thank

you for your efforts in resolving my conference reimbursement issue and my Visa extension.

I would also like to thank those with whom we have collaborated outside of the OM group. **Lars, Xiaohui**, thank you very much for your help in performing XRD in various setups and interpreting XRD data. **Annalisa, Jia, Shuxia, Zijin**, thank you for your contribution to our joint work and to the simulation part in Chapter 4.

I am also grateful to have joined the OM group, surrounded by all wonderful colleagues and creating a such harmonious environment where we help each other rather than compete, even though the group is always dynamic. **Dengyang**, thank you for teaching me how to use TRMC and fit TRMC traces, even though we only have one month of overlap. **Solrun, Maryam, Maria, Jaco, Magnus**, thank you for welcoming and helping me when I joined the group and especially for "saving" me during our unforgettable mud-walking group outing. I enjoyed having many Chinese dinners with you and hearing many funny stories from you. **Maria**, you are always helpful to me and thank you for all the information you emailed me when you heard I wanted to apply for a postdoc. I would also like to thank my other colleagues, **Deepika, Jence, Indy, Reinout, Maarten, Michael, Yan** for your help during my PhD and LO2 projects. Special thanks to all girls in my office. **Valentina**, the message "coffee?" via our group chat is a sign of your arrival. I enjoyed spending time with you in our office and TRMC lab as well as activities outside of these, boating, BBQ and lasagna night. **Jasmeen**, I think you are the coolest Jasmeen in our coolest office. You are thoughtful, humorous, and energetic which I admire. Thank you for bring us a vibrant environment in our office. More importantly, thank you for being my paranymph. **Lara**, you were the last cool girl to join our office, our overlap was even less due to different working hours, but your contribution to my project has never diminished. Thank you very much!

There is a poem in China: being alone in a foreign land, every festive occasion amplifies my longing for family. Thank you all my dear colleagues and Chinese friends for letting me feel more in our home land. **Zimu**, we started our PhD at the same time and in the same office. I am grateful that I have a close and excellent friend who has grown up together with me and is always there to help me. I enjoyed the many lunches and dinners we had together and our gathering became bigger and more fun after **Jin** and **Hua** joined. **Jin** and **Hua**, thank you for providing me with favors in the lab and I wish you the best of luck with the rest of your PhD journey.

My **dad, mom** and **brother**, I did not expect that from the beginning of my PhD to the end, we had not seen each other in real life for more than four years. I miss you very much and look forward to seeing you soon when I return to China. **Dad**, you have been the finest teacher and exemplary role model in my life, fostering and guiding me to become the person I am today. **Mom**, you and **dad** are complementary partners, you shaped my character through your grace and kindness. I am deeply grateful for your nurture and your unconditional support and love. My **brother**, I sincerely thank you for always being there with our mom and dad.

My boyfriend **Yanan**, besides obtaining a doctoral degree, meeting you was the best thing that happened to me during my PhD. Thank you for the sense of security you bring me and for your support in everything. I enjoyed every day we spent, every trip we took, every soulful conversation we had and every thought we dreamed. I look forward to

experiencing more with you in the future.

Jiashang
Delft, February 2024

Curriculum Vitæ

Jiashang ZHAO

Jiashang Zhao was born on September 15, 1992 in Hebei, China. In 2011, she started a bachelor in Chemistry at Hebei University in Baoding. Afterwards, in 2016, she went to Renmin University of China, in Beijing to pursue a Master degree in Physical Chemistry at the center for structural dynamics of functional molecular complexes and materials, where her project focused on the fabrication of metal halide perovskite solar cells and investigating the charge carrier recombination dynamics in these devices through transient photoelectric measurements. In 2019, she obtained her Master's degree with a thesis entitled "Charge Carrier Recombination Dynamics in a Bi-cationic Perovskite Solar Cell" under the supervision of Prof. Xicheng Ai and Prof. Jianping Zhang.

Later on, she moved to the Netherlands by joining the group of Dr. ir. Tom Savenije as a PhD student at Delft University of Technology, where she specialized in time-resolved spectroscopy techniques with a focus on thin films. Her research involved an in-depth exploration of the generation, recombination, and extraction of photo-generated carriers in perovskites and selective transport layers mainly using time-resolved microwave conductivity and photoluminescence measurements, combined with other structural characterization techniques, to gain insights into the interplay between structural and optoelectronic properties in metal halide perovskites. In addition, she assisted in several LO2 practice courses and supervised one bachelor and four master students.

List of Publications

This thesis is based on the following publications:

- **Zhao, J.**, van der Poll, L.M., Looman, S.L., Yan, J., Thieme, J., Ibrahim, B., Savenije, T.J., Long-lived Charge Extraction in CsMAFA-based Perovskites in n-i-p and p-i-n Structures. (Submitted)
- **Zhao, J.**, Liu, X., Wu, Z., Ibrahim, B., Thieme, J., Brocks, G., Tao, S., Bannenberg, L.J. and Savenije, T.J., Temperature-Dependent Interplay between Structural and Charge Carrier Dynamics in CsMAFA-Based Perovskites. *Adv. Funct. Mater.*, 2023, 2311727.
- **Zhao, J.**, Li, J., Liu, X., Bannenberg, L.J., Bruno, A. and Savenije, T.J., Charge Carrier Dynamics in Co-evaporated $MAPbI_3$ with a Gradient in Composition. *ACS Appl. Energy Mater.*, 2022, 5(6), 7049-7055.
- **Zhao, J.**, Caselli, V.M., Bus, M., Boshuizen, B. and Savenije, T.J., How Deep Hole Traps Affect the Charge Dynamics and Collection in Bare and Bilayers of Methylammonium Lead Bromide. *ACS Appl. Mater. Interfaces*, 2021, 13(14), 16309-16316.
- Li, J., Dewi, H.A., Wang, H., **Zhao, J.**, Tiwari, N., Yantara, N., Malinauskas, T., Getautis, V., Savenije, T.J., Mathews, N. and Mhaisalkar, S., Co-Evaporated $MAPbI_3$ with Graded Fermi Levels Enables Highly Performing, Scalable, and Flexible p-i-n Perovskite Solar Cells. *Adv. Funct. Mater.*, 2021, 31(42), 2103252.

Other publications by the author:

- Péan, E.V., **Zhao, J.**, Doolin, A.J., Savenije, T.J., and Davies, M.L., Advanced Characterization of Perovskite Thin Films using Time-Resolved Microwave Photoconductivity and Time-Resolved Photoluminescence. (In preparation)
- Zhao, C., Zhou, Z., Almalki, M., Hope, M.A., **Zhao, J.**, Gallet, T., Krishna, A., Mishra, A., Eickemeyer, F.T., Lian, X., Luo, M., Xu, J., Yang, Y., Mo, X., Zakeeruddin, S.M., Redinger, A., Savenije, T.J., Emsley, L., Chu, J., Yao, J., Zhang, H., Grätzel, M., Stabilization of Highly Efficient Perovskite Solar Cells with a Tailored Supramolecular Interface. (Submitted)
- Van der Werf, V.M., **Zhao, J.**, Koning, J.S., Nespoli, J., Thieme, J., Bus, M., Savenije, T.J., Charge Distribution in $CsFAPbI_3$ Spatially Resolved by Scanning Microwave Impedance Microscopy. *Cell Rep. Phys. Sci.*, 2023, 4(7), 101491.
- Yan, J., **Zhao, J.**, Wang, H., Kerklaan, M., Bannenberg, L.J., Ibrahim, B., Savenije, T.J., Mazzarella, L. and Isabella, O., Crystallization Process for High-Quality $Cs_{0.15}FA_{0.85}PbI_{2.85}Br_{0.15}$ Film Deposited via Simplified Sequential Vacuum Evaporation. *ACS Appl. Energy Mater.*, 2023, 6(20), 10265-10273.
- Caselli, V.M., Thieme, J., Jöbsis, H.J., Phadke, S.A., **Zhao, J.**, Hutter, E.M. and Savenije, T.J., Traps in the Spotlight: How Traps Affect the Charge Carrier Dynamics in $Cs_2AgBiBr_6$ Perovskite. *Cell Rep. Phys. Sci.*, 2022, 3(10), 101055.

- Hempel, H., Savenjie, T.J., Stolterfoht, M., Neu, J., Failla, M., Paingad, V.C., Kužel, P., Heilweil, E.J., Spies, J.A., Schleuning, M., **Zhao, J.**, Friedrich, D., Schwarzburg, K., Siebbeles, L.D.A., Dörflinger, P., Dyakonov, V., Katoh, R., Hong, M.J., Labram, J.G., Monti, M., Butler-Caddle, E., Lloyd-Hughes, J., Taheri, M.M., Baxter, J.B., Magnanelli, T.J., Luo, S., Cardon, J.M., Ardo, S., and Unold T., Predicting Solar Cell Performance from Terahertz and Microwave Spectroscopy. *Adv. Energy Mater.*, 2022, 12(13), 2102776.

- Wang, H.Y., **Zhao, J.S.**, Li, Y., Zou, Y.Q., Yu, M., Hao, M.Y., Li, Y., Li, H., Qin, Y., Mu, C. and Li, D., Diffusion Dynamics of Mobile Ions Hidden in Transient Optoelectronic Measurement in Planar Perovskite Solar Cells. *ACS Appl. Energy Mater.*, 2020, 3(9), 8330-8337.

- Guo, Y., Jin, Z., Yuan, S., **Zhao, J.S.**, Hao, M.Y., Qin, Y., Fu, L.M., Zhang, J.P. and Ai, X.C., Effects of Interfacial Energy Level Alignment on Carrier Dynamics and Photovoltaic Performance of Inverted Perovskite Solar Cells. *J. Power Sources*, 2020, 452, 227845.

- **Zhao, J.S.**, Wang, H.Y., Yu, M., Hao, M.Y., Yuan, S., Qin, Y., Fu, L.M., Zhang, J.P. and Ai, X.C., Charge Carrier Recombination Dynamics in a Bi-cationic Perovskite Solar Cell. *Phys. Chem. Chem. Phys.*, 2019, 21(10), 5409-5415.

- Yu, M., Yuan, S., Wang, H.Y., **Zhao, J.S.**, Qin, Y., Fu, L.M., Zhang, J.P. and Ai, X.C., Characterization of the Influences of Morphology on the Intrinsic Properties of Perovskite Films by Temperature-Dependent and Time-Resolved Spectroscopies. *Phys. Chem. Chem. Phys.*, 2018, 20(9), 6575-6581.

List of Presentations

- Apr 2021 (oral) at the Solliance PSC review meeting (online), the Netherlands
- Dec 2021 (poster) at the national conference Chains (online), the Netherlands
- Jan 2022 (poster) at the national conference Physics@Veldhoven (online), the Netherlands
- May 2022 (poster) at the 14th international conference on hybrid and organic photovoltaics in Valencia, Spain
- Jun 2022 (poster) LMPV annual symposium: light management, materials design, and fabrication for photovoltaics in Amsterdam, the Netherlands
- Sep 2022 (oral) at the national conference Chains in Eindhoven, the Netherlands
- Apr 2023 (oral) at the national conference Physics@Veldhoven in Eindhoven, the Netherlands
- Jun 2023 (poster) at the 15th international conference on hybrid and organic photovoltaics in London, UK